Modeling of Adsorption and Atomic Force Microscopy Imaging of Molecules on Insulating Surfaces

David Zhe Gao

2014

A thesis submitted in partial fulfilment of the requirements for the degree of Doctor of Philosophy (Ph.D.) of the University College London

I, David Zhe Gao, confirm that the work presented in this thesis is my own. Where information has been derived from other sources, I confirm that this has been indicated in the thesis.

Abstract

The study of atoms and molecules on bulk insulating surfaces is of critical importance to many fields of surface science including lubrication, and molecular electronics. I studied these systems by using a variety of theoretical methods to predict adsorption geometry, diffusion pathways, and film structure, and to interpret noncontact atomic force microscopy (NCAFM) data.

I began by using molecular dynamics (MD) simulations to predict that Pd atoms deposited onto MgO(100) exhibit some transient mobility. They were initially able to move across the surface, but were eventually captured at an adsorption site when enough energy had been dissipated. Similarly, deposited molecules may also be able move around and find nucleation sites such as step edges or kinks before becoming stabilized on surface terraces at low temperature.

I then moved on to study the properties of single molecules on oxide surfaces. I combined my theoretical calculations with experimental data to compare adsorption sites and geometries of Co-Salen molecules on NaCl(100) and NiO(100). I used density functional theory calculations (DFT) to show that minor differences in commensurability between the molecule and the surface can qualitatively change adsorption. Both surfaces are bulk insulators with simple cubic crystal structures, however, a much higher adsorption energy and distortion of the molecule on NiO(100) produced a significant vertical dipole moment.

Single molecules adsorbed onto insulators can be directly imaged with chemical resolution using metal coated NCAFM tips. However, accurate interpretation of the results is needed. I studied metallic tips using DFT calculations and developed a point dipole model to represent the Cr coated tips used experimentally. I then fit the position and magnitude of the point dipole in this model directly to experimental scan-lines and was able to produce virtual AFM (VAFM) images and scan-lines that were in quantitative agreement

with experiment. This method simultaneously reduced the complexity of interpretation of experimental data and the computational cost of producing VAFM images.

Finally, I studied larger systems using a hybrid quantum mechanics / molecular mechanics (QM/MM) and parametrized classical force fields using genetic algorithm (GA) methods. This allowed me to study CDB, a large organic molecule, on KCl(100). Static DFT calculations and classical MD simulations using these force fields showed that adsorbed CDB molecules are mobile at room temperature and stabilized at step edges due to increased adsorption energy.

These results provide insight into the processes and mechanisms that govern deposition, adsorption, and diffusion of atoms and molecules on insulating surfaces and can help guide the design of functional molecules and films.

Contents

List of Figures

List of Tables

Acknowledgements

I would like to begin by thanking my supervisors Alexander Shluger and Matthew Watkins for their guidance throughout my studies at UCL. Alex in particular has always found time to discuss physics or review publication drafts; it is easy to see his group and the science are an important part of his life. I would also like to thank Filippo Federici Canova for help with programming and the numerous discussions we had in Sendai.

Over the years, I have enjoyed several fruitful international collaborations and would like to acknowledge Alexander Schwarz and Josef Grenz at the University of Hamburg as well as Christian Loppacher and Laurent Nony at Aix-Marseille University for relentless discussions, high quality experimental data, and many good beers. With their help, I have learned much more than I could have using theory alone.

Additionally, I would like to thank my colleagues and supervisors at Chevron Oronite LLC for supporting and funding my studies and all the members of the HPC Materials Chemistry Consortium, which provided me with the computational resources that I needed to do most of the work presented here.

Finally, I would like to dedicate this thesis to my wife, Jessica, who supported me and moved halfway around the world so that I could follow my dreams. Overall, I have had an amazing experience working in London and would do it again in a heartbeat.

Preface

0.1 Personal Background and Motivation

Understanding the adsorption, mobility, and growth of atoms and molecules on bulk insulating surfaces is of critical importance to many fields of surface science. My particular interest lies in designing compounds that can be used as lubricating oil additives. My interest originates from the time I spent in the lubricating oil additive industry working in the Components group at Chevron Oronite. At that time my primary goal was to design novel additives geared towards increasing fuel economy and reducing wear in automotive and industrial engines. Some examples of commonly used additives include a Mo containing metal organic complex for reducing friction in automotive engines [1] and a Zn containing metal organic complex that is similarly employed to reduce wear [2]. These materials are used under a wide array of conditions and qualitative differences in adsorption and film formation determine how they may be used in the engine.

A standard passenger engine contains a variety of friction contacts and each region experiences different conditions that can be characterized by the viscosity, velocity, and load, as shown in Figure 1.

These friction regimes are illustrated in Figure 2 and represent qualitatively different environments. In the boundary regime, the solid surfaces are so close together that opposing asperities come into contact with each other. As film thickness increases, the separation between opposing surfaces also increases. Eventually, with enough separation, asperities on opposing surfaces only rarely interact with each other. This type of interaction is known

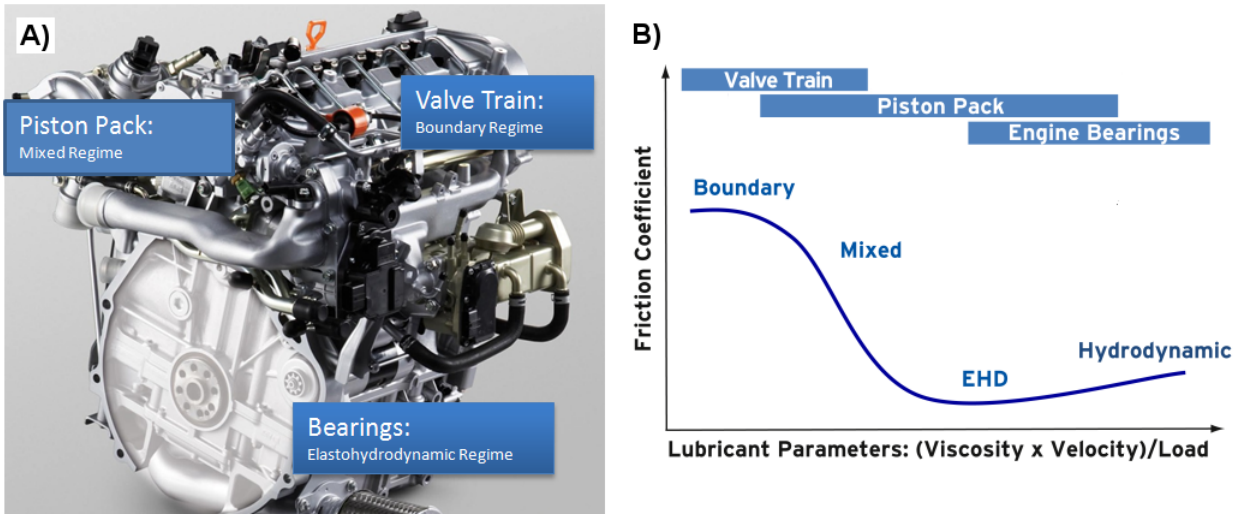

Figure 1: A) An automotive engine with several representative regions and their corresponding friction regimes. B) A Stribeck curve illustrating how these regimes can be characterized by their viscosity, velocity, and load.

as the elastohydrodynamic regime. The region in between these two extremes is known as the mixed regime. Since the engine represents such a diverse collection of environments, a blend of compounds must be designed specifically for each application. Furthermore, technologies that perform well in one region of the engine do not always provide the same benefits elsewhere.

In order to design effective compounds that are able to adsorb to surfaces and form protective films, the interactions between these molecules and oxide surfaces must be well understood. Additionally, any new additive must also be compatible in solution with existing technologies. The adsorption, growth, and energy dissipation mechanisms within these systems all play an important role in how well an additive performs. One major challenge, however, is that the engine itself is a closed environment that operates at high temperature and pressure. This makes it incredibly difficult for experiments to probe the system during operation and the mechanisms responsible for many important processes remain unknown. Furthermore, the nature of studying a system that depends so heavily on the solvent base oil and interactions between additives makes it difficult to design simple model systems to experiment on. Each formulation typically contains a large number of additive compounds in addition to the base oil solvent and the interaction between additives

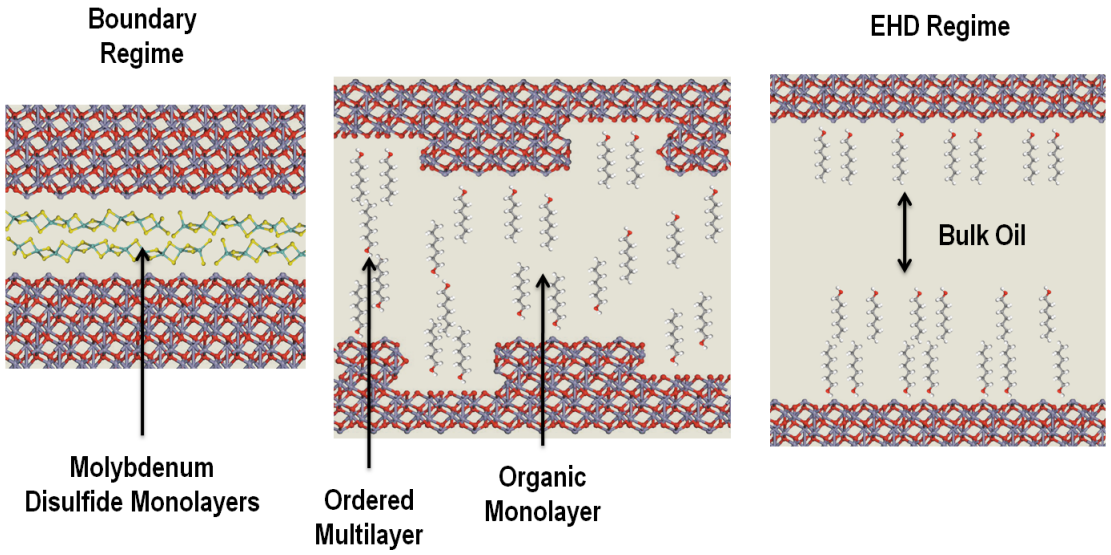

Figure 2: A schematic diagram of the interactions present in the boundary, mixed, and elastohydrodynamic regimes. O atoms are shown in red, Fe atoms in blue, C in black, H in white, S in yellow, and Mo in green. The nature of the friction reducing films needed changes depending on conditions in the engine. These films can range from monolayers of Molybdenum Disulfide in the boundary regime to ordered multilayers of organic molecules in the EHD regime depending on the distance between lubricating surfaces.

and competition between them on the surface play a large role in film formation.

These challenges result in gaps in the understanding of adsorption and film formation in these systems and many current research and development efforts can still be described as trial and error. I believe that theoretical efforts can help by filling in where experimental data is lacking. An increased understanding of the mechanisms and interactions involved will allow me to design superior functional compounds targeting specific applications, such as increasing fuel efficiency and decreasing engine wear and tear. With these goals in mind, Chevron Oronite agreed to fund my studies at UCL.

When I began this research, I quickly realized that realistic industrial systems are too complex and that I needed to start with more fundamental properties such as the adsorption, diffusion, and film structure of prototypical organic molecules and metal-organic complexes on insulating surfaces. Studying these types of molecules allowed me to collaborate with experimental groups to greatly improve my understanding of molecule-surface interactions.

Chapter 1

Introduction

1.1 Presentation of the Problem

My goal in this work was to develop a better understanding of the adsorption, diffusion, and film structure of molecules on insulating surfaces. To accomplish this, I considered a variety of theoretical approaches and combined them with experimental noncontact atomic force microscopy (NCAFM) data. Combining theoretical and experimental results can provide a wealth of knowledge on these systems, but it is important to understand the limitations and roles of each approach.

While scanning probe methods such as NCAFM are a powerful tool for imaging molecules on surfaces, these experiments are limited by the time-scale of data acquisition and by the surfaces that can be realistically employed. Experimental images can only show the before and after of many processes and the mechanisms that govern molecular adsorption, diffusion, and growth are difficult to elucidate. Many important processes, such as phase transitions (μs), chemical reactions (μs), thermal diffusion (ns), or even molecular vibrations (ps) can qualitatively change during the course of one experimental measurement. Furthermore, interpretation of the data can often be ambiguous since NCAFM images show bright and dark spots on the surface rather than atoms or molecules. Finally, simply knowing the positions of molecules on the surface does not provide information on the

character of bonding or electronic interactions within the system.

In contrast, while theoretical studies are able to predict structures and directly propose mechanisms for critical processes, they must be verified experimentally. When good agreement between theory and experiment is achieved, theoretically predicted structures and mechanisms are often used to support the interpretation of experimental data and provide additional information about the system. In my work, I used theoretical models to unambiguously interpret NCAFM data and study the deposition, adsorption, diffusion, film structure, and initial stages of film formation of atoms and molecules on bulk insulating surfaces. A combined approach is able to simultaneously interpret experimental images, verify theoretical methods and predictions, and shed light on the mechanisms behind observable phenomena.

In order to understand some of the challenges involved in combining theoretical predictions with experimental NCAFM data to study organic molecules on insulating surfaces, it is useful to consider the many interactions present within the experimental setup. A schematic diagram of the components present in the system is given in Figure 1.1A.

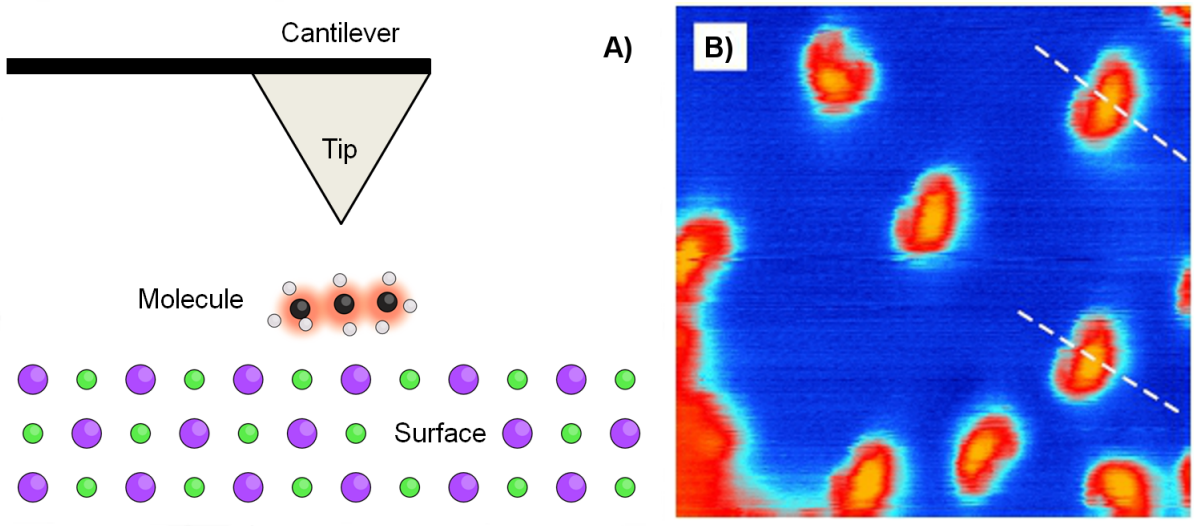

Figure 1.1: A) A schematic diagram depicting the NCAFM cantilever, tip, a molecule, and a surface. B) An experimental image taken by J. Grenz and A. Schwarz of small molecules adsorbed onto NiO(001). Molecules are shown in red while the unresolved surface is shown in blue. Dashed lines indicate the symmetry axis of the molecules.

The NCAFM probes the sample using an oscillating tip and cantilever, as depicted

in Figure 1.1A, and the resulting data can be represented as an image, such as the one shown in Figure 1.1B. However, as previously mentioned, the experimental data simply shows bright and dark spots on the surface. In order to interpret the experimental data, a multi-scale model of the entire system is needed. The development of this multi-scale model and the theoretical methods needed to provide theoretical predictions to compliment experimental data represents the main challenge to be met within the scope of this work. The problem can be partitioned into several key components as follows:

1. Theoretical predictions of properties, such as the character of bonding, changes in electronic structure due to molecular adsorption, mobility, and film structure.

2. An accurate multi-scale model of the complete system to directly compare experimental data and theoretical predictions. This simultaneously validates theoretical methods and helps interpret experimental data. The components of this model must be designed to account for the important interactions within the system:

   A) Accurate models of the molecule-surface system and the NCAFM tip.

   B) Model of the tip-sample interactions responsible for experimental contrast.

   C) Model of the instrument to account for the oscillating cantilever.

3. Long time-scale simulations that can probe the mechanisms behind experimentally observable phenomena and fill in the gaps that arise due to the time-scale of experimental measurements.

The strategy that I employed to meet these challenges and the scope of this work is described in the next section. This in turn provides the general outline of my thesis.

1.2 Scope and Outline of Thesis

The scope of this work can be described as a multi-scale study of the properties of organic molecules and films on bulk insulating surfaces. This study incorporates a multi-scale

model that provides unambiguous interpretation of experimental data. This allowed me to validate my results describing the properties of single molecules on insulating surfaces, characterize adsorption, and discuss the mechanisms behind experimentally observed phenomena. I then focused on expanding the time-scale and size-scale of my simulations to probe dynamic effects and predict the structures of monolayers on the surface.

In this thesis I start by presenting general theoretical methods that are relevant to more than one results chapter in Chapter 2. I cover density functional theory (DFT), classical force fields, and the hybrid quantum mechanics/molecular mechanics (QM/MM) techniques which can be used to describe molecule-surface interactions. Special attention is paid to common difficulties and nonstandard methods that I used to greatly reduce the computational cost of treating my systems. I then briefly discuss the molecular dynamics (MD) methods that I used to expand the time-scale of my studies.

The results chapters are then presented in the following order. Each chapter starts with a general introduction which includes a review of the latest methods, prior work, a description of the challenge that I set out to address, and outlines novelty of my work. The logical first step to these studies was to examine what happens when an atom or molecule first lands on the surface and the effects this may have on the distribution of single atoms (or molecules) and their ability to reach surface features, such as step edges. With this in mind, I studied the mechanisms of transient mobility using a simple model system. Pd atoms were deposited on the MgO(001) surface using classical pair potentials and molecular dynamics at experimentally feasible conditions. The simple atomic system allowed me to perform a large number of simulations of sufficiently long duration to characterize the mechanisms that are responsible for transient mobility. The data was compared and analyzed in the context of prior experiments and theory in the fields of scattering, tribology, growth kinetics, and diffusion. This work is discussed in Chapter 3 of this thesis.

I then moved on to examine the properties of adsorbed single molecules on oxide surfaces in Chapter 4. This work provided an opportunity to study quantum mechanical methods and other techniques needed to investigate organic molecules and metal-organic

complexes on oxide surfaces. I was able to compare my results to experimental images as part of a collaboration with A. Schwarz, J. Grenz, and R. Wiesendanger at the University of Hamburg. Co-Salen (a Co containing metal-organic complex) was deposited onto NiO(001) and studied using NCAFM in combination with DFT in order to examine the differences in adsorption and growth on various bulk insulator surfaces. By combining theory and experiment in this system, I was able to determine the adsorption site of Co-Salen on NiO(001) and provide an explanation for the differences observed in comparison to a previous study of Co-Salen on NaCl(001) [3]. My results highlight the qualitative differences that arise due to slight changes in commensurability on the two surfaces despite the fact that both are bulk insulators with the same simple cubic crystal structure.

While these results were in good agreement with my initial interpretation of the experimental data, the imaging mechanism and the properties of the NCAFM tip used in these studies still needed to be explored. To accomplish this I studied the properties of the metal coated NCAFM tip to develop a point dipole model for the tip. Then I directly simulated NCAFM experiments by combining this point dipole model with a virtual AFM (VAFM) code. This multi-scale method was tested by studying adsorbed CO molecules on NiO(001) and shown to provide quantitative agreement with experimental data. The point dipole model and these results are discussed in Chapter 5.

I then moved on to study the structure of self-assembled monolayers of 1,4-bis(cyanophenyl)-2,5-bis(decyloxy)benzene (CDB) molecules on KCl(001) in Chapter 6. This work was part of a collaboration with NCAFM experimentalists C. Loppacher and L. Nony at Aix-Marseille University. Using DFT methods, I characterized the competing molecule-molecule and molecule-surface interactions within the system. This data then allowed me to propose atomistic models for experimentally observed monolayer patterns. I compared the energies of these structures to identify the most stable configuration. This configuration was then used to generate VAFM images using the point dipole model which could be directly compared to experimental images. However, despite good agreement between experimental and theoretical images, initial *ab initio* molecular dynamics simulations pre-

dicted that the molecules are quite dynamic on the surface. A static picture is somewhat misleading, especially since the experimental data was taken at room temperature. Unfortunately, I was unable to investigate these properties or the diffusion, trapping, and growth of these molecules using DFT due to the prohibitively expensive computational cost.

In order to study dynamic effects, the scale of the system had to be substantially increased in several ways. The number of molecules had to be increased in order to avoid imposing heavy constraints on the system. The time-scale had to be greatly increased to study slower processes, such as growth and nucleation. These kinds of simulations are typically performed using classical molecular dynamics, however, there were no readily available molecule-surface force fields for my system. My solution was to fit a set of molecule-surface interactions to *ab initio* data by using genetic algorithm (GA) methods. I was then able to study diffusion, adhesion to step edges, and dewetting to gain insight into some of the dynamic properties of the system. The scheme I employed to generate molecule-surface forcefields is presented in Chapter 7 along with these results.

Finally, the results of these studies are summarized and discussed in Chapter 8 and suggestions are made for future work.

1.3 List of Publications

The following publications are derived from work presented in this thesis. The author gave a major contribution in performing the calculations and writing the original manuscripts in all of the listed papers.

1) D. Z. Gao, M. B. Watkins, and A. L. Shluger, "Transient Mobility Mechanisms of Deposited Metal Atoms on Insulating Surfaces: Pd on MgO(100)", *J. Phys. Chem. C* **116**, 14471-14479 (2012)

2) A. Schwarz, D. Z. Gao, K. Lammle, J. Grenz, M. B. Watkins, A. L. Shluger, and R.

Wiesendanger, "Determining Adsorption Geometry, Bonding, and Translational Pathways of a Metal-Organic Complex on an Oxide Surface: Co-Salen on NiO(001)", *J. Phys. Chem. C* **117**, 1105-1112 (2013)

3) D. Z. Gao, J. Grenz, M. B. Watkins, F. Federici Canova, A. Schwarz, R. Wiesendanger and A. L. Shluger, "Using Metallic Noncontact Atomic Force Microscope Tips for Imaging Insulators and Polar Molecules: Tip Characterization and Imaging Mechanisms", *ACS Nano* **8**, 5339-5351 (2014)

4) D. Z. Gao, A. Schwarz, and A. L. Shluger. (2014) "Imaging Molecules on Bulk Insulators Using Metallic Tips" In S. Morita (Ed.) Noncontact Atomic Force Microscopy Volume 3 (Ch 17). New York, NY: Springer.

5) A. Amrous, F. Bocquet, L. Nony, F. Para, C. Loppacher, S. Lamare, F. Palmino, F. Cherioux, D. Z. Gao, F. Federici Canova, M. B. Watkins, and A. L. Shluger, "Molecular Design and Control over the Morphology of Self-Assembled Films on Ionic Substrates", *Adv. Mater. Interfaces* **1**, 1400414-1-14 (2014)

6) D. Z. Gao, F. Federici Canova, M. B. Watkins, and A. L. Shluger, "Efficient Parameterization of Complex Molecule-Surface Force Fields", *J. Comput. Chem.* **36**, 1187-1195 (2015)

The author contributed in the following publication by writing sections of code and editing the original manuscript.

7) J. N. Tracey, F. Federici Canova, D. Z. Gao, P. Spijker, B. Reischl, A. S. Foster, "Flexible and Modular Virtual Scanning Probe Microscope", *Comput. Phys. Commun.* **Accepted**

(2015)

The following publication is not included in the thesis, but is discussed in the preface. The author contributed by synthesizing the molecules, performing chemical analysis of the molecules, and writing the original manuscript.

8) G. Bhalla, M. H. Tsang, D. Gao, Q. Chen. W. Ruhe, N. Ushioda, "Frictional Properties of Molybdenum-Based Lubricating Oil Additives Using Green Chemistry", *SAE Int. J. Fuels Lubr.* **5**, 496-503 (2012)

Chapter 2

Theoretical Methods

Aims: This chapter reviews the standard theoretical methods that I used throughout the thesis to represent adsorbed molecules and monolayers. It begins by briefly describing density functional theory (DFT) in section 2.2. The mixed Gaussians and plane waves method (GPW) is discussed in section 2.2.1, hybrid functionals in section 2.2.2, basis set superposition error (BSSE) in section 2.2.3, the auxiliary density matrix method (ADMM) and methods for basis set parameterization in 2.2.4, and the semi-empirical long-range dispersion corrections in section 2.2.5. These methods are later used to study the electronic structure of small molecules adsorbed onto insulating surfaces. I then describe classical force fields in section 2.3 and the hybrid quantum mechanics/molecular mechanics (QM/MM) method in section 2.4, which were used to greatly reduce the computational cost of studying larger systems. Finally I discuss molecular dynamics (MD), which allowed me to investigate dynamic properties, in section 2.5.

Methods: Electronically complex systems that contain molecules adsorbed onto a surface often require both hybrid functionals and extensive basis sets in order to properly represent the electronic structure of the system. It is critical that the electronic interactions between the molecule and the substrate are well accounted for to avoid effects such as artificial charge transfer. In order to facilitate the use of extensive basis sets with hybrid functions, I parameterized auxiliary basis sets to use with the ADMM. This technique can

be used to greatly improve the speed of hybrid functional calculations performed using the CP2K code. When available, the system can be represented using classical force fields to greatly reduce computational cost. When studying surfaces, the periodic QM/MM scheme can be used to combine DFT and classical force fields when only part of the system can be represented classically.

2.1 Introduction

Throughout this thesis I employ a large range of standard and nonstandard theoretical techniques to study the molecule-surface interactions that influence adsorption, diffusion, and film structure. Following the logic that I previously outlined, it is important to accurately represent the NCAFM tip as well as the molecule-surface system. These methods include density functional theory (DFT) [4] techniques using standard [5, 6] and hybrid functionals [7, 8], classical force fields, and hybrid QM/MM [9, 10] methods. Using these representations of the atomic or electronic structure of the system, I performed energy minimizations using the conjugate gradient and steepest descent methods [4] and calculated energy barriers using constrained minimization, nudged elastic band [11], and the dimer methods [12]. When possible, I evolved my systems over time using MD simulations. Due to the multi-scale nature of modeling NCAFM experiments and the multi-scale nature of dynamic molecule-surface systems, an in depth discussion of every method that I used throughout the thesis would be too lengthy. Fortunately, the standard methods that I employed are well studied and thorough descriptions can be found throughout the literature. Instead, I will primarily focus on nonstandard methods that I have used, models that I have personally developed, and instances where I needed to parametrize the model to suit my needs. This chapter, in particular, focuses on methods that were used in more than one results chapter of the thesis.

2.2 Density Functional Theory

One of the major advantages that theory can provide when studying new systems is intimate knowledge of the electronic structure of the systems in question. NCAFM experiments in particular can illustrate the geometry and adsorption site of molecules, but are unable to provide information about the character of binding. Electronic structure calculations can be used to predict the character of binding, adsorption site, geometry, and even barriers to motion across the surface. Importantly, it is difficult to understand the

interaction between the NCAFM tip and the sample without accurate electronic structure data on each. Experimentally observable properties can then be compared with theoretical predictions in order to verify the accuracy of the method used and improve credibility of other predictions.

The starting point in theoretical physics for calculating electronic structures is the Schrödinger equation. Published in 1926 by the Austrian physicist Erwin Schrödinger, it is a partial differential equation that describes how the quantum state of a given system changes with time. However, the exact solution to the Schrödinger equation cannot be obtained for systems containing many particles, even when the Born-Oppenheimer approximation is applied. This approximation uses the fact that nuclei have much larger mass than electrons to greatly simplify the problem by considering the electrons as moving in a field of fixed nuclei. The problem largely stems from the fact that solving the Schrödinger equation means solving for the exact wavefunction of the system, which is dependent on 3^N variables for N number of particles. Fortunately the Hohenberg-Kohn theorems demonstrated that the ground state properties of many-electron systems can be determined from the electron density instead of the wavefunction. These methods are called density functional theory (DFT).

Since DFT is a well known method and has been very popular for solid state physics calculations starting from the 1970s and quantum chemistry calculations starting from the 1990s, detailed descriptions of the general methods can be found elsewhere [4]. Instead, I will focus on the major challenges I encountered and the techniques that I employed to perform accurate electronic structure calculations on large systems with reasonable computational cost. The methods presented in this chapter are relevant to several results chapters while more specific examples are instead discussed within the chapter in which they are applied.

2.2.1 CP2K and the Gaussian and Plane Waves Method (GPW)

Studying the electronic structure of molecules on surfaces implies a need to include a large number of atoms in my calculations. While individual organic molecules may be small, any representation of the surface must be of sufficient area so that the individual molecules do not interact with periodic images of themselves. Additionally, the surface slab must contain enough layers to replicate proper surface rumpling, bond lengths, and electronic states. Due to the large number of electrons required for such molecule-surface systems, I employed the CP2K code in order to use the efficient Gaussians and Plane Waves (GPW) method [13]. In order to calculate Kohn-Sham orbitals and calculate ground state properties of the system using DFT, the electron density must be represented using some basis set. One popular choice is to use a combination of functions centered around the atomic coordinates of nuclei, or what is called a local basis set. A common representation is to use Gaussian functions. An advantage of using Gaussian basis sets is that they can be constructed systematically [14] to improve accuracy while still providing a compact description of the wave function. While these calculations are difficult to fully converge, they have been shown to produce reasonably accurate results [13]. This enables the use of efficient methods for solving self-consistent field (SCF) equations. Since the functions are localized, they rapidly decay to zero far away from atomic coordinates and the Kohn-Sham, overlap, and density matrix are sparse as system size increases. However, Gaussian basis sets often do not provide an accurate description of electron density near the nucleus. Furthermore, the accuracy of the calculation depends greatly on the completeness of the basis set. Finally, the localized nature of such basis sets also results in basis set superposition error (BSSE) in areas where basis functions overlap.

Another commonly used type of basis set is constructed from plane waves. These basis sets are not dependent on the atomic coordinates of nuclei in the system and are well suited for describing periodic materials. While the periodic and unlocalized nature of plane wave basis sets helps avoid superposition error, one major drawback is that the empty regions of the simulation are described with the same accuracy as areas that contain atoms and

increases computational cost. One advantage to using plane waves is the ability to use Fast Fourier Transforms (FFT) to solve the Poisson equation and obtain the Hartree energy. However, they typically require more basis functions than localized basis sets.

The Gaussian and plane waves (GPW) method [13] uses both of these types of basis sets simultaneously to describe the system. A Gaussian basis set is used to describe the single particle wave functions (Kohn-Sham orbitals) while a plane wave basis set is used to describe the density of the system. This enables the use of linearly scaling fast Fourier transform (FFT) methods when computing the electrostatic interactions within the system, greatly reducing computational cost. The main feature of the GPW method is that electron density is represented in two ways in order to compute both total energy and the Kohn-Sham matrix with improved speed. When using a Gaussian basis set, the representation of the electron density $n(r)$ can be written as

$$n(r) = \sum_{\mu\nu} P^{\mu\nu} \psi_\mu(\mathbf{r}) \psi_\nu(\mathbf{r}), \tag{2.1}$$

where $P^{\mu\nu}$ is a density matrix element and $\psi_\mu = \sum_i d_{i\mu} g_i$. $g_i(\mathbf{r})$ represents the primitive Gaussian functions and $d_{i\mu}$ represents the contraction coefficients. The plane wave representation can be written as

$$\tilde{n}(r) = \frac{1}{\Omega} \sum_{\mathbf{G}} \tilde{n}(\mathbf{G}) exp(i\mathbf{G} \cdot \mathbf{r}), \tag{2.2}$$

where Ω represents the volume of the unit cell and $\mathbf{G}$ represents the reciprocal lattice vectors. The expansion coefficients $\tilde{n}(\mathbf{G})$ are such that $\tilde{n}(\mathbf{r}) = n(\mathbf{r})$ on a regular grid in the unit cells. It is then possible to convert between the basis sets using an efficient mapping procedure [13] which will not be described here. When using the dual GPW representation, the Kohn-Sham DFT energy expression as used within the GPW framework can be written as

$$
\begin{aligned}
E[n] &= E^T[n] + E^V[n] + E^H[n] + E^{XC}[n] + E^{II} \\
&= \sum_{\mu\nu} P^{\mu\nu} \langle \psi_\mu(\mathbf{r})| - \frac{1}{2}\nabla^2 |\psi_{nu}(\mathbf{r})\rangle \\
&+ \sum_{\mu\nu} P^{\mu\nu} \langle \psi_\mu(\mathbf{r})| V^{PP}_{loc}(r) |\psi_{nu}(\mathbf{r})\rangle \\
&+ \sum_{\mu\nu} P^{\mu\nu} \langle \psi_\mu(\mathbf{r})| V^{PP}_{nl}(r, r`) |\psi_{nu}(\mathbf{r})\rangle \\
&+ 2\pi\Omega \sum_G \frac{\tilde{n}^*(\mathbf{G})\tilde{n}(\mathbf{G})}{\mathbf{G}^2} + \int e^{XC}(\mathbf{r}) d\mathbf{r} \\
&+ \frac{1}{2} \sum_{I \neq J} \frac{Z_I Z_J}{|\mathbf{R}_I - \mathbf{R}_J|},
\end{aligned}
\tag{2.3}
$$

where $E^T[n]$ represents the electronic kinetic energy, $E^V[n]$ represents the electronic interaction with ionic cores, $E^H[n]$ represents the electronic Hartree energy, $E^{XC}[n]$ represents the exchange-correlation energy, and E^{II} represents the interaction between ionic cores with charges of Z_I and Z_J and positions R_I and R_J. $E^V[n]$ is described by pseudopotentials with a local term $V^{PP}_{loc}(r)$ and a non-local term $V^{PP}_{nl}(r, r`)$.

The efficient GPW method reduces computational cost by computing the Kohn-Sham matrix in a linearly scaling fashion and the total energy in a cubically scaling fashion with respect to the number of basis functions. This allowed me to treat more complex molecule-surface systems using DFT to study their physical properties.

2.2.2 Hybrid Functionals (B3LYP)

In Kohn-Sham DFT, the properties of a system can be calculated using functionals, or functions of another function. The functional used in this case is the spatially dependent electron density which can be calculated from the wave function:

$$
\rho(\vec{r}) = \sum_{i=1}^{N} |\psi_i(\mathbf{r})|^2, \tag{2.4}
$$

where ψ_r represents single particle wave functions. The total energy of the system can then be written as a functional of the electron density as follows:

$$F[\rho(\mathbf{r})] = E_{KE}[\rho(\mathbf{r})] + E_H[\rho(\mathbf{r})] + E_{XC}[\rho(\mathbf{r})] + v(r)\rho(\mathbf{r})dr, \tag{2.5}$$

where $E_{KE}[\rho(\mathbf{r})]$ represents the kinetic energy of the system system, $E_H[\rho(\mathbf{r})]$ the Hartree energy, $E_{XC}[\rho(\mathbf{r})]$ the exchange-correlation, and $v(\mathbf{r})\rho(\mathbf{r})dr$ the contributions from an external potential.

One main challenge with DFT is that the exact functionals for exchange and correlation are not known except for the free electron gas. This leads to a number of popular approximations which can be used to calculate certain properties accurately. Some examples include the local-density approximation (LDA), where the functional only depends on the density at the coordinate where it is being evaluated, and the generalized gradient approximation (GGA), where the the gradient of the density at the coordinate of interest is considered as well. Hybrid functionals represent other approximations to the exchange-correlation energy functional. They are commonly used to improve the accuracy of many calculated molecular properties, such as bond length, vibrational frequencies, and band gaps, which may be poorly described with LDA or GGA. When employing a hybrid functional, the exchange-correlation term of the energy is augmented using some fraction of the exact Hartree-Fock exchange (HFX) as:

$$E_{XC}[\rho(r)] = \alpha E_X^{HFX}[\psi_i] + (1-\alpha)E_X^{DFT}[\rho] + E_C^{DFT}[\rho], \tag{2.6}$$

where α indicates the fraction of HFX included while E_X and E_C represent the density functionals for exchange and correlation. I use hybrid functionals in the work presented in Chapters 5 and 6 in order to accurately represent the electronic structure of the system. However, they do increase the computational cost significantly so I employ standard functionals when possible.

2.2.3 Basis Set Superposition Error (BSSE)

One of the previously mentioned major drawbacks to using Gaussian basis sets to represent the wave function is basis set superposition error (BSSE) [15, 16]. These basis sets are localized, or centered around the atomic coordinates of nuclei, and it is assumed that most of the electron density of the system resides in regions very close to these coordinates. These regions are described with much higher levels of accuracy, or more basis functions, than the empty regions of the simulation. However, in the regions where the basis sets of two different atoms overlap, the electron density is represented by the basis sets centered around both atoms resulting in a difference in energy. The energy of a dimer consisting of atom A and B can be represented as follows:

$$E_{DIMER} = E_{AB}[BasisA, B] - E_A[BasisA] - E_B[BasisB]. \tag{2.7}$$

The counterpoise correction method can be employed to estimate the superposition error by calculating the energy difference between calculations performed using the original basis set and calculations using both the original basis set and that of the adjacent atom:

$$E^{CC}_{DIMER} = E_{AB}[BasisA, B] - E_A[BasisA, B] - E_B[BasisA, B]. \tag{2.8}$$

Superposition error is of particular importance when studying surfaces since many basis sets are designed for bulk materials instead. At the surface, electrons behave differently than in the bulk, and often additional functions are needed to represent diffuse electrons or polarization effects. The magnitude of this error can be large enough to qualitatively change theoretical predictions and must be accounted for carefully by either choosing an extensive basis set or manually adding functions until superposition error is reduced to an acceptable level.

2.2.4 Auxiliary Density Matrix Method (ADMM)

The previously described method helps reduce computational cost by using the GPW approach. However, hybrid functional and extensive basis sets both greatly increase compute time. Furthermore, the cost of computing the HFX term scales to the fourth power with respect to the number of primitive basis set functions used. Fortunately, as system size increases many of these integrals can be screened to reduce computational cost. If heavily contracted basis sets are used, the number of primitive integrals increases. In addition, the number of functions required grows quadratically with quantum number making polarization functions incredibly expensive. Finally, diffuse functions further compound the issue since they reduce the region of space where electron density is negligible. This makes screening more difficult, further increasing the expense of calculating HFX. In order to use hybrid functionals while minimizing BSSE, the efficiency of calculating HFX must be improved.

To accomplish this, I employed the Auxiliary Density Matrix Method (ADMM) [17]. When using an atomic centered basis set $\phi_\mu(r)$ we can write

$$\psi_i(r) = \sum_\mu C^{\mu i}\phi_\mu(r). \tag{2.9}$$

The Hartree-Fock exchange component can then be written as a product of the density matrix and the two electron integrals as shown below.

$$E_X^{HFX}[P] = -\frac{1}{2}\sum_{\lambda\sigma\mu\nu} P^{\mu\sigma}P^{\nu\lambda}(\mu\nu|\lambda\sigma). \tag{2.10}$$

The density matrix elements $P^{\mu\nu}$ can be obtained using the molecular (MO) coefficients C as follows:

$$P^{\mu\nu} = \sum_i C^{\mu i}C^{\nu i}, \tag{2.11}$$

and the two electron integrals can be represented as:

$$(\mu\nu|\lambda\sigma) = (\int\int \phi_\mu(r_1)\phi_\nu(r_1)g(|r_2 - r_1|)\phi_\lambda(r_2)\phi_\sigma(r_2)dr_1dr_2). \quad (2.12)$$

In this equation, $g(r)$ represents the $(1/r)$ Coulombic interaction potential in standard Hartree-Fock theory. The density matrix P can then be replaced by an auxiliary density matrix $\hat{P}$ that is either smaller or rapidly decaying and the HFX energy term can be written as follows:

$$E_x^{HFX}[P] = E_x^{HFX}[\hat{P}]+(E_x^{HFX}[P]-E_x^{HFX}[\hat{P}]) \approx E_x^{HFX}[P]+(E_x^{DFT}[P]-E_x^{DFT}[\hat{P}]). \quad (2.13)$$

In this scheme, the critical approximation is that the difference between exchange energy calculated using the primary and auxiliary density matrices is well represented by GGA calculations. As the auxiliary basis set becomes identical to the primary basis set, this difference converges to zero. However, the rate of convergence depends not only on the primary basis set, but the functional as well. The above equation states that a correction factor based on the difference in the exchange term between using primary or auxiliary density matrices must be applied when computing the HFX energy using an auxiliary density matrix. Since only a small fraction of exchange is used in most hybrid functionals, any error in the final calculation will be greatly reduced. The current implementation of the correction term is based on the GGA correction for PBE exchange [5, 6]. Using other parameterizations and functionals for the correction term has not been explored.

The ADMM greatly reduces the computational cost of combining hybrid functionals with extensive basis sets. This allowed me to minimize BSSE while ensuring that the electronic structure of my systems were properly represented with reasonable computational cost.

Auxiliary Basis Sets

In order to use the ADMM, an auxiliary density matrix must be generated. This can be done using a variety of methods. These range from directly manipulating the sparsity of the matrix during the calculation to generating it from less extensive auxiliary basis sets. In this work, I have elected to generate auxiliary density matrices from auxiliary basis sets fit to model systems. Since the primary density matrix P generated using a high quality primary basis set ($\phi_{mu}(r)$) is large, an auxiliary basis set ($\hat{\phi}_{mu}(r)$) is used to describe the wave function during HFX calculations instead:

$$\psi_i(r) = \sum_{\mu} \hat{C}^{\mu i} \hat{\phi}_{\mu}(r). \tag{2.14}$$

The auxiliary density matrix elements $\hat{P}^{\mu\nu}$ are obtained from molecular coefficients as follows:

$$\hat{P}^{\mu\nu} = \sum_{i} \hat{C}^{\mu i} \hat{C}^{\nu i}. \tag{2.15}$$

The optimal value for these MO coefficients are then obtained by minimizing the square of the difference between occupied wave functions in the primary and auxiliary basis set representations:

$$\min_{\hat{C}} = \sum_{i} \int (\psi_j(\mathbf{r}) - \hat{\psi}_j(\mathbf{r}))^2 d\mathbf{r}. \tag{2.16}$$

Auxiliary basis sets for the first two rows of elements are provided with the original documentation [17]. However, for the work presented in Chapters 5 and 6, I needed to generate additional auxiliary basis sets in order to account for Ni and Co atoms.

Basis Set Parameterization

The first step to generating auxiliary basis sets for the missing atom types was to choose the functional form. For simplicity, a set of 10 Gaussian type orbitals was selected as

the auxiliary basis set along with several small Ni containing systems to use as a fitting set. The auxiliary basis set chosen contains four S functions, three P functions and three D functions. They are designed to be used with the GTH pseudopotentials [18] and the MOLOPT primary basis set [19]. Ni atoms in this work were represented using 18 valence electrons ($3s^2 4s^2 3p^6 4d^8$) and the Co atoms were represented using 17 valence electrons ($3s^2 4s^2 3p^6 4d^7$). The fitting environments included a small NiO cluster (8 atoms), $C_4H_6NiO_4$, Ni_4O_4, $NiCO_3$, and $Ni(OH)_2$ as shown in Figure 2.1.

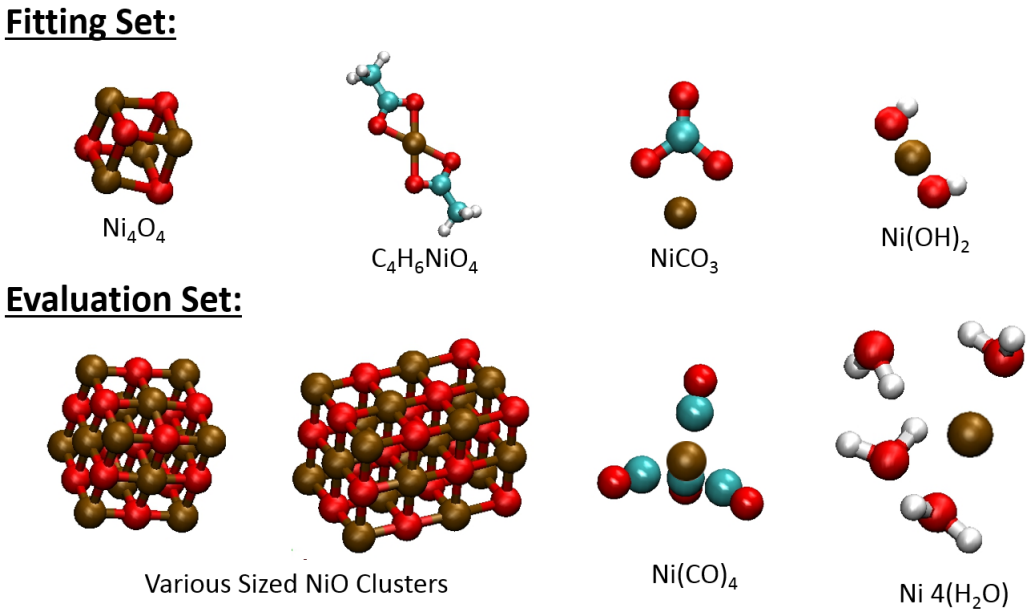

Figure 2.1: A set of small systems used to generate the auxiliary basis set for Ni and another set of systems chosen to evaluate transferability and accuracy of the auxiliary basis set are shown. Ni atoms are shown in brown, O atoms in red, C atoms in blue, and H atoms in white.

The geometries of these systems were optimized using the primary (MOLOPT) basis set in CP2K to obtain minimized geometries. The coefficients of the auxiliary basis set were then optimized to minimize the energy at these predetermined geometries with the auxiliary basis set. The optimized coefficients for each fitting system are given below in Table 2.1, along with the coefficients optimized using a single Ni atom. The similarities between these optimized auxiliary basis sets indicate good transferability between systems of a similar chemical environment. However, the results obtained from a single Ni atom show that the 10 Gaussian form selected may not be sufficient to represent an isolated

atom.

	$C_4H_6NiO_4$	Ni_4O_4	$NiCO_3$	$Ni(OH)_2$	Ni Atom
S1	7.5156	7.9027	7.9220	7.8271	7.5648
S2	2.5295	2.3215	2.2590	2.2951	2.4200
S3	0.9630	0.9306	0.8920	0.9085	0.9231
S4	0.0975	0.1138	0.0951	0.0940	0.0875
P1	2.8309	2.8125	2.8089	2.8102	2.8560
P2	0.9295	0.9059	0.9010	0.9056	0.9933
P3	0.1485	0.1090	0.1099	0.0920	**0.3671**
D1	6.8959	7.0401	6.9866	6.9467	6.7958
D2	2.1364	2.1998	2.1631	2.1502	2.0368
D3	0.5493	0.5686	0.5550	0.5503	0.4981

Table 2.1: A table of the auxiliary basis set coefficients generated using the four fitting systems and a single Ni atom. The auxiliary basis sets generated from each of the fitting systems are nearly identical. When fitting onto the neutral Ni atom, however, there is a large difference in one of the P functions which is highlighted in bold. These values represent the exponents of the Gaussians and are given in $Bohr^{-2}$.

I then averaged the parameters obtained over the four fitting environments to produce transferrable auxiliary basis set for Ni. This auxiliary basis set was then evaluated using a set of four evaluation systems including two larger NiO clusters (27 and 36 atoms), Ni with four adjacent water molecules, and $Ni(CO)_4$, as shown in Figure 2.1. The energy difference between calculations performed with and without enabling the ADMM was found to be less than 10 meV. A more detailed examination reveals that even the one electron energy levels within these simple systems is well represented using the ADMM, with differences in the range of 0.1 to 0.05 eV (see Supporting Table A.1).

This process was then repeated for Co. Additionally, I included an auxiliary basis set that was directly fit to the Co-Salen molecule for comparison, as shown in Table 2.2. As with the Ni atom, the isolated Co atom shows some minor differences when compared to the Co-Salen and fitting systems.

I then used these auxiliary basis sets in conjunction with the ADMM to perform DFT calculations of CO molecules and Co-Salen molecules on NiO(100) in chapters 5 and 6. Examples files for parametrizing auxiliary basis sets can be found on the supplementary disk attached to this thesis.

	Co-Salen	Fitting Set	Co Atom
S1	7.1616	7.0466	6.7514
S2	1.9742	1.9755	2.2846
S3	0.7936	0.7736	0.9084
S4	0.0798	0.0931	0.0867
P1	2.7259	2.7987	2.8565
P2	0.9279	1.0142	1.1224
P3	0.1165	0.1813	**0.4312**
D1	6.6690	6.4889	6.4301
D2	2.1234	2.0031	1.9389
D3	0.5686	0.5168	0.4863

Table 2.2: A table containing optimized auxiliary basis set parameters for Co. They were generated from fitting directly to the Co-Salen molecule in addition to the set of fitting molecules for comparison. When fitting to the isolated Co atom, however, there is again a large difference in one of the P functions which is highlighted in bold. This is similar to the difference observed for the Ni atom. These values represent the exponents of the Gaussians and are given in $Bohr^{-2}$.

2.2.5 Semi-Empirical Dispersion Corrections

Another well known challenge for density functional theory is accounting for the van der Waals interactions that result from fluctuating charge distributions. These dispersion interactions or van der Waals forces are due to long-range electron correlation effects that are not present in local and semi-local density functionals and must be accounted for by adding an extra energy term. There are many available techniques ranging from simple semi-empirical corrections to non-local long-range density functionals. However, the computational cost of many of my systems restricts the selection of viable techniques. In this thesis, these interactions have been accounted for in my calculations using the semi-empirical DFT-D2 method [20]. In this method, the total energy is corrected by adding an extra dispersion potential to Kohn-Sham DFT energy:

$$E_{DFT-D2} = E_{KS-DFT} + E_{Dispersion}. \tag{2.17}$$

The dispersion energy is given to be:

$$E_{disp} = -S_6 \sum_{i=1}^{N_{atoms}-1} \sum_{j=i+1}^{N_{atoms}} \frac{C_6^{ij}}{R_{ij}^6} f_{damp}(R_{ij}), \tag{2.18}$$

where C_6^{ij} represents the dispersion coefficient for atom i and j and S_6 represents a scaling term that is uniquely optimized for each DFT functional. A damping function helps to minimize error when atoms are within normal bonding distances and their interactions are adequately represented by uncorrected DFT. Within my systems, these interactions can be partitioned into two components. For molecular atoms, I have employed the default parameters for the DFT-D2 [20] scheme. The treatment of the surface atoms, however, is less straightforward and is discussed for each material in the relevant chapter.

Since many of the molecule-surface interactions that I studied can be characterized as physisorption, dispersion corrections are critical. In many of the systems that I studied, these contributions account for a significant fraction of the total adsorption energy. However, since these interactions tend to be uniform across the entire surface, they play less of a role when determining adsorption sites and diffusion pathways. Nevertheless, they must be properly included when studying molecule-surface interactions.

2.3 Classical Force Fields

Ab initio calculation can provide useful information on systems where interactions between the molecule and the surface have not been previously studied. However, they are severely limited in scale due to high computational cost. In order to increase both system size and the time-scale of my studies, a much simpler representation of the system is needed. Fortunately, the potential of my systems can often be simplified by using sets of mathematical functions. These functions can be parametrized in order to reproduce experimentally observable physical properties or calculated *ab initio* data. This implies, however, that the system in question has either already been studied in the past or that I must parametrize these functions first.

Classical models are readily available in the literature for a wide range of solid sur-

faces, molecules, and bulk materials. These force fields or potentials are usually optimized to reproduce experimentally observable properties including the lattice structure, compressibility, vibrational spectra, bond length, and geometry. While these force fields are incredibly diverse, the total energy of a system represented using an additive force field can be generally expressed as:

$$E_{Total} = E_{Bonded} + E_{Nonbonded}, \tag{2.19}$$

where the bonded interactions (E_{Bonded}) represent covalent or short-range contributions to the energy and can be generally expressed as:

$$E_{Bonded} = E_{Bond} + E_{Angle} + E_{Dihedral} \cdots \tag{2.20}$$

These bonded interactions are extremely varied and can be described using any number of terms depending on the force field in question. The long-range nonbonded interactions ($E_{Nonbonded}$) typically deal with the electrostatic and van der Waals contributions as shown:

$$E_{Nonbonded} = E_{Electrostatic} + E_{vdW}. \tag{2.21}$$

The electrostatic component is typically accounted for by assigning finite charges to each atom, while the vdW term is typically represented using Lennard-Jones (LJ) potentials. It is important to note that often these classical force field contributions are simply analytical equations meant to reproduce an experimental or theoretical value and that the form itself may not have any physical meaning. While force fields do exist for a wide range of materials, they often cannot be combined due to differences in functional form. A more thorough discussion of the classical force fields that I employed will be given in each relevant chapter of this thesis and the method that I used to generate new classical molecule-surface force fields is discussed in Chapter 7.

2.4 Hybrid Quantum Mechanics/Molecular Mechanics (QM/MM)

Classical force fields are able to accurately describe the physical properties of many solid materials and surfaces, however, such force fields are not often available for molecule-surface systems. While *ab initio* techniques do not suffer from these limitations, it is prohibitively expensive to perform *ab initio* molecular dynamics on systems containing hundreds of atoms. One popular solution has been to employ a multi-scale quantum mechanics/molecular mechanics (QM/MM) scheme. Originally popularized by Warshel and Levit [21], these methods partition the system into regions that can be treated quantum mechanically (QM) and regions that can be treated using molecular mechanics (MM) in order to greatly reduce computational cost, as shown in Figure 2.2.

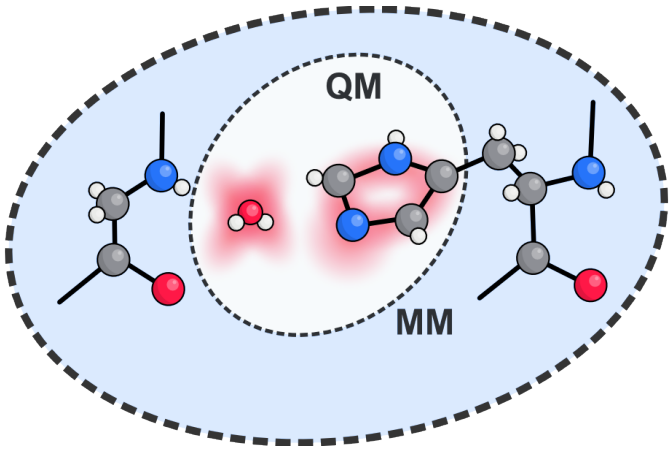

Figure 2.2: A schematic representation of the embedded cluster QM/MM scheme. Quantum mechanically represented atoms reside in the center of the simulation within the indicated QM region. The boundaries between QM and MM regions are designated using dashed lines.

In this representation, the QM region is a finite size and bounded on all sides by the MM region. This implementation has been used successfully in the past to study properties including chemical reactivity [22, 23, 24, 25, 26, 27, 28, 29] and has even been applied to self-assembled monolayers on metal surfaces [30]. To study periodic arrangements of large organic molecules on insulating surfaces, I chose to use the CP2K implementation [9, 10]

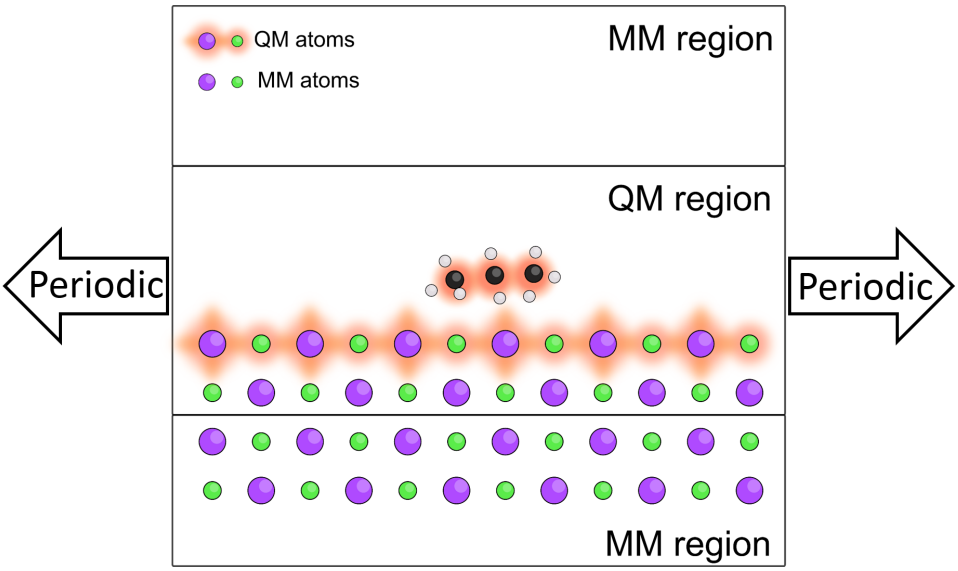

Figure 2.3: A schematic representation of the embedded slab QM/MM scheme. Quantum mechanically represented atoms are highlighted in red and the boundaries of the QM and MM regions are highlighted. MM atoms closer to the QM region have their charge density projected onto finer grids than those at the edge of the simulation box. This model is periodic in the plane parallel to the surface as indicated.

to represent the system using an embedded slab model. In this scheme, two MM regions are placed above and below a QM region (along Z) and all three regions are periodically treated along XY, as shown in Figure 2.3. This results in an infinite QM slab which is ideal for treating my systems. When monolayers of organic molecules interact with the surface, the interaction region occurs across a large area of the surface which would be expensive to model without using periodic boundary conditions.

The total energy of a system represented in this way can be partitioned into three independent components and treated additively. It can be expressed as follows:

$$E_{Total}(r_\alpha, r_a) = E_{QM}(r_\alpha) + E_{MM}(r_a) + E_{QM/MM}(r_\alpha, r_a), \tag{2.22}$$

where E_{QM} represents the purely quantum mechanical contribution to energy, E_{MM} represents the purely classical contribution to energy, and $E_{QM/MM}$ represents the interaction energy between the two regions. The purely quantum mechanical contribution is accounted for using standard DFT methods and the purely classical contribution is de-

scribed using the interactions outlined in the previous section. Finally, the interaction between the QM and MM subsystems can be expressed as shown:

$$E_{QM/MM}(r_\alpha, r_a) = \sum_{a \in MM} q_a \int \frac{\rho(r, r_\alpha)}{|r - r_a|} dr + \sum_{\substack{a \in MM \\ \alpha \in QM}} v_{vdW}(r_\alpha, r_a), \tag{2.23}$$

where r_a represents the position of a MM atom with a charge of q_a, $\rho(r, r_\alpha)$ represents the total electronic and nuclear charge density of the quantum mechanical system, and $v_{vdW}(r_\alpha, r_a)$ represents the van der Waals interactions between a classical atom (a) and a quantum atom (α).

When the interaction between QM and MM regions is considered, the problem can be further partitioned into short and long-range components. One of the main challenges involved in calculating the short-range contribution is attributed to electron spill-out or leakage at the boundary between the QM region and the MM region. This problem arises when classical atoms are represented using simple point charges. When the electrons of a QM atom come close to the position of such a classical atom, they can be trapped onto the positive point charge. This effect can be enhanced if diffuse basis sets are used. Since I am primarily interested in studying surfaces, diffuse basis sets are often required in order to properly account for the electronic structure and electron leakage must be addressed. In order to solve this problem, the MM atoms are represented using a charge density of finite width when the interaction between QM and MM atoms are considered. The short-range component of the QM-MM interaction is accounted for as shown:

$$v_a(r, r_a) = \frac{Erf(\frac{|r - r_a|}{r_{c,a}})}{|r - r_a|}, \tag{2.24}$$

where $r_{c,a}$ is a parameter representing the radius of atom a. This function represents the potential energy function generated using a Gaussian charge distribution as shown:

$$\rho(r, r_a) = (\frac{1}{\sqrt{\pi} * r_{c,a}})^3 e^{-(\frac{|r - r_a|}{r_{c,a}})^2}. \tag{2.25}$$

The Gaussian smearing of charges has been used in previous studies to repair broken covalent bonds at QM/MM boundaries [31, 32]. In the scheme that I employed, however, they are only intended to prevent the charge leakage problem and have not been considered in the context of treating QM/MM boundaries that contain covalent bonds.

The long-range interactions between QM and MM regions can be described by adding the contribution of the MM classical field to the one-electron Hamiltonian as shown:

$$H^{\mu v}_{QM/MM} = -\int \psi_\mu(r, r_a) \sum \frac{q_a}{|r_a - r|} \psi_v(r, r_\alpha) dr, \tag{2.26}$$

where ψ_μ and ψ_v are Gaussian basis functions and q_a is the atomic charge of a classical atom a at the coordinates r_a. The brute force evaluation of the total $E_{QM/MM}$ component previously described is time consuming and requires operations on the order of $N_\mu N_{MM}$, where N_μ represents the number of grid points (typically 10^6) and N_{MM} represents the number of MM atoms.

Fortunately, this challenge can be met *via* efficient decomposition of the electrostatic potential into Gaussian functions with different cutoffs. Using this method, the electrostatic potential of the system can be written in terms of Gaussian functions with varying cutoffs as:

$$v_a(r, r_a) = \frac{Erf(\frac{|r-r_a|}{r_{c,a}})}{|r - r_a|} = \sum_{N_g} A_g exp(-(\frac{|r - r_a|}{G_g})^2) + R_{low}(|r - r_a|). \tag{2.27}$$

The Coulomb potential is represented using a sum of N_g Gaussian functions with amplitudes of A_g and widths of G_g and a residual function R_{low}. If the amplitudes and widths are chosen correctly, the residual function will be smooth and its Fourier transform will be approximately zero for $g >> G_{cut}$. G_{cut} is dependent on the spacing of the grid that the R_{low} function will be mapped. The fitting of these parameters and the implementation of these algorithms are well described by Laino et al. [9], and will not be discussed here.

The QM/MM method allowed me to treat monolayer structures formed by large organic molecules by greatly reducing the number of surface atoms that had to be represented

quantum mechanically in my system. Furthermore, this reduction in computational expense allowed me to generate enough *ab initio* data to parametrize a classical force field in Chapter 7.

2.4.1 QM/MM Representation of KCl(001)

The first step in using such a QM/MM representation is to verify that the electronic structure of the surface does not differ significantly when compared to a full DFT calculation. I evaluated the method on the KCl(001), which was the substrate studied in Chapters 6 and 7.

First, I examined the electronic structure of the KCl(001) surface to determine whether or not a QM/MM approach is able to produce results that are equivalent to performing the full DFT calculation. In these evaluations the molecular mechanics region (MM) was represented using a set of classical parameters by Catlow *et al.* [33] while the quantum mechanics region (QM) was treated using the GPW method [13], the PBE/GGA [5, 6] functional, and the MOLOPT basis sets [19].

The full DFT calculation of KCl bulk material using B3LYP [7, 8] estimates the HOMO/LUMO gap to be 7.6 eV. This value is in agreement with prior calculations (7.77 eV [34]) and experimental data (7.6 eV [35]). However, due to the size of the systems that I was interested in, such expensive hybrid functionals were not desirable. My calculations showed that calculations performed using the PBE/GGA [5, 6] functional could produce band gaps of 5.6 eV for the bulk material and 5.4 eV for the KCl(001) surface. The 5.4 eV surface band gap was calculated using a 4 layer periodic slab of KCl where the bottom layer of atoms was fixed while the rest of the system was allowed to relax. Finally, these methods gave produced a lattice constant of 6.3 Å and a surface rumpling of 0.03 Å, in agreement with experimental values [36]. These results indicated that a local functional could reasonably approximate the bulk insulating properties of the bulk material and the surface.

Next, I needed to examine the relationship between the number of QM layers used

within the scheme and the electronic structure of the surface. To accomplish this, I plotted the electronic density of states of a 4 layer KCl(001) surface slab while varying the number of atomic layers represented quantum mechanically, as shown in Figure 2.4. A 3 layer quantum mechanics representation of the system produced a band gap of 4.8 eV, which was slightly reduced as fewer quantum layers of atoms were used. At the extreme limit where the surface is represented using just one QM layer and three MM layers, the band gap of KCl(100) was predicted to be 4.4 eV.

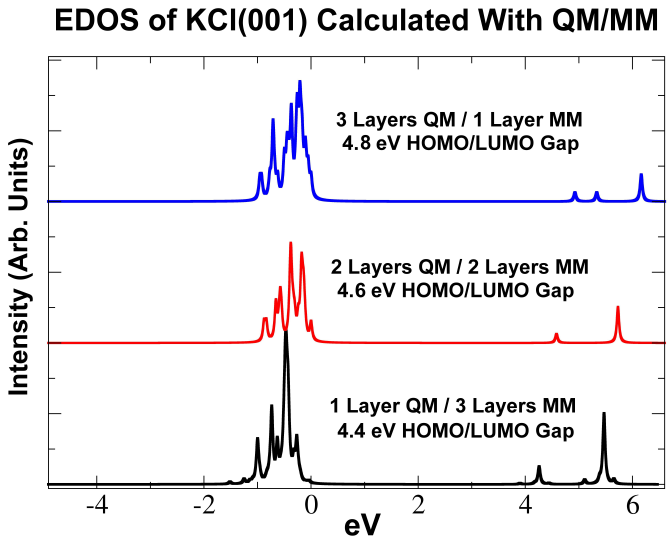

Figure 2.4: The electronic density of states of the KCl(001) surface calculated using several QM/MM schemes. These calculations represented the surface using varying numbers of QM and MM layers of atoms. The bottom layer of MM atoms were fixed while the rest of the system was allowed to relax. This treatment is able to produce a band gap of 4.4 eV with a only single layer of QM atoms.

One common problem in previously employed embedded cluster methods is that electron density tends to redistribute from quantum mechanically treated atoms to the nearest classical atoms [37]. In prior studies one common solution was to apply pseudopotentials to the cations nearest the QM region [37]. However, in CP2K the classical atoms are not represented as point charges, but are treated as Gaussian charge distributions, greatly reducing this effect in my system. The size of the Gaussian function used was determined by the ionic radius of the atom in question. In this work I used a value of 152 pm for K

and 167 pm for Cl. These distributions were assigned charges of +1 and -1 respectively. An isosurface of the electron density of the system (0.001 electrons) is shown in Figure 2.5. The electron density is confined to areas around quantum mechanical atoms and there is effectively no charge density present on any of the classically treated atoms.

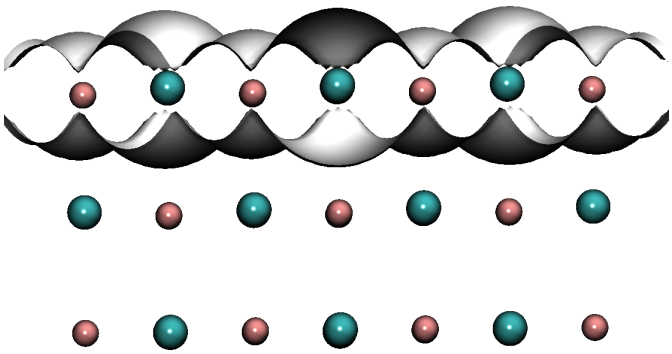

Figure 2.5: An isosurface (0.001 electrons) of the electron density of the QM/MM system. The top layer of atoms has been represented quantum mechanically while the rest are classically treated. K is shown in green and Cl is shown in red while the isosurface is shown in silver. There is effectively no charge density on any of the surface atoms beyond the first layer.

These results showed that the QM/MM scheme could reasonably reproduce the insulating properties of the KCl(001) surface while greatly reducing the number of atoms treated quantum mechanically. A summary of the properties of the KCl(001) surface obtained from experiment [35, 36], standard DFT (GGA/PBE) methods, and QM/MM methods is shown in Table 2.3.

	Lattice Constant	Surface Rumpling	Band Gap
Experiment	6.3 Å	0.03 Å	7.6 eV
DFT (GGA/PBE)	6.3 Å	0.03 Å	5.4 eV
1QM/3MM Layers	6.3 Å	0.04 Å	4.4 eV

Table 2.3: The properties of the KCl(001) surface from experimental data, a full DFT (GGA/PBE) representation, and the QM/MM scheme using 1 QM layer and 3 MM atomic layers.

These results show that the QM/MM method can reproduce the lattice constant on the surface, the surface rumpling, and the insulating properties of KCl(001). However, before

using such an approximation in the context of molecule-surface studies, it is important to ensure that the molecule-surface interactions are not heavily influenced by such a reduction in the HOMO/LUMO gap of the surface. Finally, it is important to note that further increasing the thickness of the MM slab in this system provides very little benefit while substantially increasing the memory requirement of these calculations due to the Gaussian smearing of MM point charges. Examples input files for a QM/MM calculation of KCl can be found on the supplementary disk attached to this thesis.

2.5 Molecular Dynamics (MD)

Accurate representations of the electronic structure or atomic structure of the system using the methods described so far in this chapter can be instrumental in predicting many physical properties and interpreting experimental data. However, in order to account for dynamic effects that may take place during or in between subsequent experimental measurements, I needed to consider the time evolution of my systems. The molecular dynamics (MD) method can be used to explicitly propagate the finite temperature trajectories of a system of particles by integrating Newton's laws of motion.

The technique was first conceived in 1959 [38, 39] and is widely applied today in the fields of chemical physics, materials science, and molecular modeling. It is often used to calculate the thermodynamic properties of microscopic systems and to predict the behavior of such systems over short periods of time. This method simulates the time evolution of a single microscopic system, which must be repeated in order to extract statistically meaningful data.

Using these methods, simulations can be performed on a small finite system in a way that mimics the behavior of a macroscopic system to study dynamic properties. MD is a complex and well studied method and a more complete review of the basic concepts and a review of the latest developments can be found in a review article [40]. However, a description of some of the relevant techniques that I used will be given here.

2.5.1 Velocity Verlet Algorithm

When performing MD simulations, the previously mentioned equations of motion must be solved numerically by integrating over the positions and velocities of all the particles in the system over time. Since the goal of my studies is to evolve my systems over significant periods of time, it is critical that the integration scheme employed conserves energy and momentum over a large number of time steps. The error that arises can be attributed to a combination of the timestep Δt and the algorithm.

I have used a timestep of 1 fs in all of the calculations discussed within this thesis. This value was chosen in order to ensure that all the microscopic processes within my molecule-surface system could be accurately represented. Indeed, prior studies suggest that 1.8 fs is sufficient for simulating the vibrational properties of a H_2 molecule while 3.8 fs is sufficient for a CO_2 molecule [41]. Furthermore, timesteps of 1 fs have been shown to produce reasonable results regarding thermal conductivity for alkali halide surfaces [42].

This timestep was used in conjunction with the Velocity Verlet algorithm implemented within the LAMMPS code. The original Verlet algorithm is a well known method that was first used in 1791 by Delambre and later popularized by Verlet in the 1960s [43]. It can be written as follows as Taylor expansions for the positions of the particles $r(t)$ forward:

$$r(t+\Delta t) = r(t) + v(t)\Delta t + \frac{a(t)\Delta t^2}{2} + \frac{b(t)\Delta t^3}{6} + O(\Delta t^4), \tag{2.28}$$

and backwards in time:

$$r(t-\Delta t) = r(t) + v(t)\Delta t + \frac{a(t)\Delta t^2}{2} - \frac{b(t)\Delta t^3}{6} + O(\Delta t^4), \tag{2.29}$$

where $r(t)$ are the positions of the particles at time (t), v represents the velocities, a represents the accelerations, and b represents the third derivatives of r with respect to t. Adding these two expressions together gives:

$$r(t+\Delta t) = 2r(t) - r(t-\Delta t) + a(t)\Delta t^2 + O(\Delta t^4). \tag{2.30}$$

Using the Verlet algorithm gives an error on the order of Δt^4 as shown above. The main problem with this standard algorithm is that the velocities of the particles within the system have not been accounted for. In most MD simulations, it is necessary to calculate the kinetic energy in order to evaluate the total energy of the system and determine whether or not energy conservation was achieved throughout the simulation. The simplest way of computing the velocities can be expressed as:

$$v(t) = \frac{r(t + \Delta t) - r(t - \Delta t)}{2\Delta t}. \tag{2.31}$$

Unfortunately, this results in an error on the order of Δt^2. A more commonly used version of the algorithm called the Velocity Verlet algorithm addresses this problem by obtaining the positions and velocities as follows:

$$r(t + \Delta t) = r(t) + v(t)\Delta t + \frac{a(t)\Delta t^2}{2}, \tag{2.32}$$

$$v(t + \frac{\Delta t}{2}) = v(t) + \frac{a(t)\Delta t}{2}. \tag{2.33}$$

This treatment reduces the error to an order of Δt^3. In the work presented in this thesis, the Velocity Verlet algorithm was used when performing MD calculations unless otherwise stated.

2.5.2 NVE and NVT Ensembles

In every study presented in this thesis, the treatment of energy within my MD systems was of critical importance and had to be carefully considered. To this end I used several ensembles which will be briefly described. The first method is called the NVE ensemble, or microcanonical ensemble, which represents a system with a constant number of atoms (N), volume (V), and energy(E). When using NVE, the total energy of the system is conserved while potential and kinetic energy are exchanged throughout the trajectory. The force (F) acting on each particle within a system containing N particles with x coordinates can be

expressed as:

$$F(x) = -\nabla U(x), \tag{2.34}$$

where $U(x)$ represents the potential energy function of the system as a function of the particle coordinates. This function is often referred to as the potential or force field representing the system and can be obtained using *ab initio* or classical methods as previously described in this chapter. The equation shown comes from Newton's second law and shows that the force on each particle (F) can be calculated as the negative gradient of this potential. At every timestep, the positions and velocities of every particle in the system can be integrated using methods such as the previously described Verlet algorithm [43]. This data can then be used to evolve the system over time and study dynamic effects.

One of the problems that arises when employing the NVE ensemble involves the treatment of temperature when performing MD calculations. One example can be seen in Chapter 4 where I studied the deposition of Pd atoms on MgO(001). Since the surface is represented using a finite number of atoms, the deposited Pd atoms inevitably transfer their deposition energy (or incident energy) to the surface. This may cause an unphysical increase in temperature within the system since in reality this energy would be rapidly dissipated and shared across the entire surface with little change in temperature. The canonical ensemble can help alleviate such problems.

The NVT ensemble, or canonical ensemble, represents a system with a constant number of atoms (N), volume (V), and temperature (T). When using NVT, the energy of the system is regulated using a thermostat to add or remove energy from the boundaries of the system in a realistic way. Some of the popular thermostat techniques include the Nosé-Hoover, and Berendsen thermostats. More information on these techniques can be found in a review article by Hünenberger [44].

In this thesis, I used the NVE ensemble when possible for the sake of simplicity. When using the NVT ensemble, I employed the Nosé-Hoover thermostat unless otherwise stated.

Chapter 3

Transient Mobility during Deposition: Pd on MgO(001)

Aims: This chapter describes the results of studying Pd atom deposition onto MgO(001). The importance and mechanisms of transient mobility of atoms and molecules adsorbing at surfaces have been a subject of controversy for many years. Atoms or molecules that exhibit transient mobility upon deposition may quickly migrate to surface features and defects. This affects the kinetics of growth and structures of nanoclusters and surface layers. However, since experiments are only able to study the surface before and after deposition, effects such as transient mobility must be studied theoretically. Section 3.1 gives an introduction and reviews prior experimental and theoretical work. Section 3.2 gives a description of the theoretical methods used in this study. The results are presented in Section 3.3 and includes an overview of the adsorption process and analysis of the mechanisms behind transient mobility. Finally, I present a discussion and conclusions in Section 3.4.

Methods: I used classical molecular dynamics simulations to examine the transient mobility of Pd atoms adsorbing onto MgO(100). Incoming atoms were assigned incident kinetic energies not exceeding 0.4 eV and the simulation cell was treated using stochastic boundary conditions to avoid reflecting phonons.

Results: My calculations show that deposited Pd atoms exhibit high mobility at temperatures below 80 K where contributions from thermal diffusion processes are negligible. With the selected deposition conditions, corresponding to Pd cluster growth experiments, 76% of the impinging Pd atoms can be expected to travel up to 20 Å away from the collision site before capture on a 5 K surface. Furthermore, the transient mobility of metal atoms on oxide surfaces is expected to decrease with decreasing incident energy and increase with decreasing incident angle. These results are compared and discussed in the context of prior studies of other surface diffusion processes, such as long jumps. At higher surface temperatures, however, any observed mobility can primarily be attributed to thermally activated processes rather than transient mobility mechanisms.

3.1 Introduction and Prior Work

The primary goal of my work is to study the properties of molecules on insulating surfaces and how their structure and interactions with the surface influence properties including adsorption, diffusion, and growth. A logical starting point to these studies is to examine the deposition and adsorption of adsorbates onto oxide surfaces. I began by investigating the simplest representation of such a system: single atoms landing on an MgO(001) surface. As an atom impinges on a sample surface, it can recoil directly away from the surface *via* scattering or it may travel along the surface for a significant amount of time while dissipating excess energy into phonons and electronic excitations [45]. It will eventually either desorb or become trapped and thermally equilibrated at the surface. Fast transient dynamic processes that precede the equilibrium adsorption state can have a noticeable affect on the growth kinetics, intermediate structures, and final structures of deposited films and islands [46]. There has been a significant amount of both experimental [47, 48, 49, 50, 51, 52, 53, 54, 55, 56] and theoretical [57, 58, 59, 60, 61, 62, 63, 64] work on the adsorption of metal atoms onto oxide samples and thin films, facilitated by the development of scanning probe methods including NCAFM. Most of these studies, however, focused on the equilibrium diffusion pathways of already adsorbed atoms or the structures and properties of clusters grown on the surface. I selected Pd on MgO as a prototypical system since it is one of the best studied systems of this type [51] and can be represented using classical force fields. In particular, the growth of Pd clusters on the MgO <100> surface at high temperatures has been reasonably well described using rate equations and the nucleation at defects model [56]. Xu *et al.* [57] suggest that the apparent fast diffusion of Pd at low temperatures towards defect sites can be explained by the fact that small clusters diffuse faster than individual atoms. Furthermore, experimental studies of a similar system, Au on MgO, discusses the possibility of transient mobility of deposited Au atoms [65].

Experimental studies of atomic adsorption on various substrates have long suggested that adsorbing atoms may possess enhanced mobility before equilibrating at the surface at temperatures where the contribution from thermally activated diffusion should be negligi-

ble. To explain these experimental observations, transient mobility was often included into kinetic Monte Carlo simulations and rate calculations [66, 67, 68, 69, 70]. However, the mechanisms responsible for this process were not well understood. One proposed mechanism that has been explored is the downward funneling or steering [71, 72] of deposited atoms. Another mechanism that has been proposed is that of transient or ballistic mobility [67]. Transient mobility describes a situation where atoms gain energy due to adsorption or condensation and use this energy to travel along the surface. There have been many experimental and theoretical investigations on the topic both confirming and contradicting the existence of transient mobility [69, 70, 71, 72, 73, 74, 75, 76, 77, 78, 79, 80, 81, 82, 83, 84, 85, 86, 87, 88, 89, 90, 91, 92, 93] in various systems. However, the mechanisms behind the transient mobility of metal atoms on oxide surfaces have not been explored. In this chapter I emphasize the potential importance of the transient mobility of metal atoms deposited at oxide surfaces, especially at low temperatures, and provide an insight into the mechanisms behind this mobility.

The entire adsorption process can be partitioned into several key parts. The first part is the initial collision of the atom with the surface. This portion of the adsorption process is similar to scattering mechanisms that have been studied in the past [94, 95, 96, 97, 98, 99, 100, 101, 102, 103, 104, 105]. Experimental data and theoretical studies using molecular dynamics have shown that a small percentage of atoms thermalize on the surface before absorbing energy from surface vibrations and desorbing again. The focus of scattering studies, however, has been on the properties of the scattered or desorbed atoms rather than those that were stabilized on the surface.

The second part happens after the initial collision when adatoms are initially mobile on the surface. This can be compared to prior studies of the thermally activated diffusion of equilibrated adsorbates. The diffusion of single atoms has been studied in detail and is well described in a review Antczak and Ehrlich [106]. Langmuir [107] initially described the atoms as hopping between spaces with separation a, and gave the diffusivity in terms of the lifetime (t) of the atom at a particular site as:

$$D = a^2/2t \tag{3.1}$$

Bassett and Webber [108], however, have shown that diffusion is not necessarily one dimensional and may involve several simultaneous events. There has been a significant amount of work exploring mechanisms by which atoms are able to jump from one nearest neighbor binding site to the next [109, 110, 111, 112, 113, 114, 115, 116, 117]. The surface diffusion picture further evolved when Tully *et al.* [118] and DeLorenzi *et al.* [119] observed through simulation that at higher temperatures jumps can occur between sites separated by several lattice spacings. These long jumps were then studied and verified both theoretically [113] and experimentally [114]. More examples of theoretical and experimental work can be found in the review article by Antczak and Ehrlich [106].

In this chapter I focus on the adsorption of Pd atoms on the MgO(100) surface and demonstrate that Pd atoms undergo complex dynamics upon adsorption to the surface. These processes are dependent on the site of the initial collision with the surface and on the temperature of the surface. I discuss the energy dissipation mechanisms involved in the thermalization of impinging Pd atoms at the surface and examine the temperature dependence of transient mobility. Finally, I compare these mechanisms to those of long jumps in surface diffusion, scattering, and slip-stick friction and use them to make predictions regarding atomic and molecular mobility at low experimental temperatures.

3.2 Theoretical Methods

Classical atomistic simulations of Pd interaction with the MgO(001) surface were performed using the GULP code [120]. These included static geometry minimizations, diffusion barrier calculations, and an extensive series of molecular dynamics simulations of the collisions of Pd atoms with the surface at different surface sites and temperatures. In addition, further molecular dynamics simulations were performed using the SciFi code [121]. Examples files for these calculations can be found on the supplementary disk attached to this thesis.

3.2.1 Classical Force Field

To describe the properties of a MgO(001) surface and the interactions between Pd atoms and the surface, I used a classical force field developed by Y. Long and N. X. Chen [63]. These potentials were originally fit to plane wave DFT calculations using the GGA approximation and ultrasoft pseudo-potentials. It was suggested by Kolodney [122] that the relative size of the impinging atom can play a role when modeling the collisions of large atoms with a compact surface such as MgO. Fortunately, this force field effectively takes into account the radii of the atoms within the system. In order to represent a large enough surface area to simulate the entire adsorption process and the subsequent energy dissipation and atomic mobility, a large number of surface atoms is required. To reduce complexity and energy drift in my simulations, the force field chosen does not incorporate the shell model [123] and thus neglects the polarizability of surface O ions. They therefore do not describe the rumpling of the MgO(001) surface [124]. The corresponding displacements of the surface ions of MgO, however, are small and are not expected to qualitatively change the results of my simulations. Using these methods, the most favourable Pd atom adsorption site was determined to be above an oxygen site on the MgO surface with a calculated adsorption energy of 0.9 eV. This is consistent with previously calculated [63] values and experiment [125, 126]. Pd atoms can diffuse through several possible pathways by hopping between various oxygen sites on the (001) surface. The corresponding diffusion barriers were calculated with both the GULP and SciFi codes using both the constrained minimization and Nudged Elastic Band methods [127]. The lowest diffusion barrier was found to be 0.3 eV. This corresponds to a jump between the positions above two nearest neighbour surface O ions, and is in agreement with prior work [63].

3.2.2 Molecular Dynamics Setup

To simulate collisions of Pd atoms with the MgO(001) surface I used an NVE micro canonical ensemble. The MgO sample was represented using a finite cluster of atoms which was

to be large enough to contain the entire trajectory of the Pd atom and avoid artificial effects. Prior studies have highlighted that transient mobility can be artificially induced due to insufficient slab thickness [73]. Furthermore, since I used the NVE ensemble and kept energy constant throughout the simulation, the MgO cluster had to be large enough to absorb the energy of the incoming Pd atom with a negligible change in the overall temperature of the surface. With these considerations, the MgO cluster I constructed contained a total of six planes of 18 x 18 atoms (1944 atoms in total) and represents an ideal terrace on the MgO(001) surface. My calculations indicated that this cluster is large enough that Pd atoms directed at the center of the block are captured and thermalized before reaching the edge of the cluster.

In addition to constant energy simulations, I also performed simulations using stochastic boundary conditions [128, 129] as an alternative method of handling energy in the system to verify my results. When using stochastic boundary conditions, energy is absorbed by atoms near the simulation boundaries to mimic the behavior of a macroscopically large surface or bulk material. Two adsorption sites were investigated using both constant energy conditions and stochastic boundary conditions. The first adsorption site was the one near the Mg lattice site and the second was the one near the O lattice site. A total of five simulations were performed at each site. Adsorbing Pd atoms were observed to travel the same distance on the surface in both types of simulations with a standard deviation of less than one lattice distance. These results show that the NVE ensemble and the system size employed are sufficient to qualitatively describe the adsorption and subsequent mobility of a Pd atom on MgO(001).

Pd atoms can be deposited on the MgO surface experimentally at a variety of surface temperatures ranging from 5 K to several hundred K. On these surfaces with variable temperature, the rate of Pd atom diffusion can be estimated using the Arrhenius rate equation with the previously calculated diffusion barrier of 0.3 eV and an attempt frequency of 2.2 x 10^{12} s^{-1}. This attempt frequency was estimated by taking the harmonic frequency of Pd-O stretch vibrations of a Pd atom adsorbed on the MgO surface (see Supporting Figure B.1).

This model predicts that transient mobility should be observed at temperatures below 80 K where the Pd atom is immobile over typical experimental time-scales. Any manifestations of mobility at these temperatures should be directly related to the adsorption process. It has been proposed that at low incident energies and low surface temperatures quantum effects may be present in the system [105, 130, 131]. Indeed these effects were shown to be significant in examples involving H atoms in the temperature range of 30-150 K [132]. However, the mass of the Pd atom is much larger than that of a H atom and these effects are not expected to be significant in my system.

In order to achieve a level of comparability with experiments, I considered the incident energies of impinging Pd atoms in the context of experimental deposition conditions. One popular deposition method is electron-beam evaporation where a rod of material is heated until atoms are thermally desorbed [58]. In this case, I estimated that Pd atoms would evaporate at a temperature of around 3200 Kelvin which corresponds to the boiling point of the material. The incident kinetic energies of electron beam evaporated Pd atoms can then be estimated to be within a range of 0 - 0.4 eV.

In order to determine the sample size required to qualitatively describe the adsorption process, I performed ten simulations of a Pd atom adsorbing onto the MgO surface at a selection of collision sites along the (100) direction of the surface between Mg and O. If the collision time of Pd atoms with the MgO surface is much greater than the frequency of surface vibrations, the incoming atom will interact with the average positions of surface atoms. However, if it is shorter, Pd will interact with the instantaneous positions of the surface atoms and result in many unique trajectories. Modeling such trajectories requires much more extensive sampling. The frequency of surface vibrations in this case was estimated by using the phonon spectra of the MgO surface [57] and compared to the time during which a Pd atom interacts with an initial Mg or O surface site during the collision process. This interaction time was estimated by monitoring the length of time during which the incoming atom interacts with the site of collision in my simulations before moving on to another adsorption site. In this case I defined interaction to take

place when the Pd atom to Mg (or O) potential is nonzero. This corresponds to a Pd to Mg (or O) distance of less than 4 Å (see Supporting Figure B.2). According to this criterion, I predicted an average interaction time of about 5 x 10^{-13} seconds with 0.4 eV of Pd incident energy (see Supporting Figure B.3). During this time, the Pd atom will experience on average five surface vibrations during the initial collision. Pd atoms with a lower incident velocity will interact with the initial collision site for even longer and be exposed to even more surface vibrations. However, these results indicate that extensive sampling may still be necessary.

To further assess the amount of statistical sampling required, I performed another 100 simulations for Pd atoms with 0.4 eV incident kinetic energy colliding perpendicular to the MgO <100> surface above a Mg site and another 100 simulations above the O site. The initial conditions for these simulations were produced by first equilibrating the system for varying amounts of time to generate a range of unique starting positions and velocities. The atoms within the surface were initially assigned a randomly generated Gaussian distribution of velocities and allowed to equilibrate for 10 ps and a set of starting positions and velocities was taken every 1 ps afterwards. The total distance travelled of the Pd atoms in these simulations had a standard deviation of less than one lattice distance for Pd atoms colliding near Mg, while all 100 simulations of Pd atoms impinging near O sites resulted in capture at the collision site. However, the exact trajectories and final adsorption positions of these Pd atoms were quite varied. These test calculations indicate that five simulations per adsorption site should be sufficient to qualitatively predict the distances travelled by impinging Pd atoms.

In order to reduce the huge number of possible incoming Pd trajectories, I then assumed the experimental setup can be described as a situation where the Pd source is macroscopically far away from the surface. This meant that all incoming Pd atoms should have momentum perpendicular to the surface and start out with zero lateral velocity. Thus any observed Pd lateral motion can be attributed to the adsorption process. I will, however, qualitatively discuss the effect of changing the incident angle, incident energy, and surface

temperature.

Finally, Pd atoms were believed to approach the surface with an even distribution above all sites. In order to simulate such an even flux of atoms, I used a planar mesh of evenly spaced points above the surface to represent the entire range of possible Pd atom starting positions. Each Pd atom starting position was then treated by performing simulations using a set of five unique starting trajectories. Since this initial grid of starting positions represents an even flux of incoming atoms rather than an even distribution of collision sites, steering effects experienced by the incoming atoms are already included in these calculations . Unless specifically stated, the MD simulations presented in the next section were performed with Pd atoms starting from these points 6.0 Å away from the surface with 0.4 eV of incident kinetic energy (KE). A 5 K surface temperature was chosen for the MgO(001) surface to avoid thermally activated diffusion.

3.3 Results

The entire process that occurs when Pd atoms are deposited onto a MgO surface can be partitioned into several important events. These include the initial collision which is followed by a momentum change, lateral motion, thermalization, and thermally activated diffusion between adsorption sites. My simulations demonstrate that some incoming Pd atoms are immediately captured at optimal adsorption sites upon contact with the surface while another fraction of the incoming atoms are either scattered or reflected. The remaining Pd atoms first exhibit significant lateral mobility along the surface before becoming thermalized. The average distance travelled by these atoms is higher when they initially land closer to Mg surface sites. I will focus further discussions mainly on these mobile atoms in order to investigate the mechanisms behind transient mobility.

3.3.1 Overview of the Adsorption Process

The dynamics properties of impinging Pd atoms can be qualitatively understood by analyzing the interactions between the incoming atom and the surface as defined by the adiabatic potential energy surface of a Pd atom at the MgO surface. Pd atoms experience varying diffusion barriers depending on the height above the surface and the direction at which they are travelling, as shown in Figure 3.1. At large distances the atom-surface interaction is entirely attractive due to the attraction between the large Pd atom and surface O^{2-} ions. This global attractive interaction greatly increases the percentage of incoming atoms that are captured at the surface. At short Pd-Mg distances, however, the repulsive interaction between Pd and Mg must be considered.

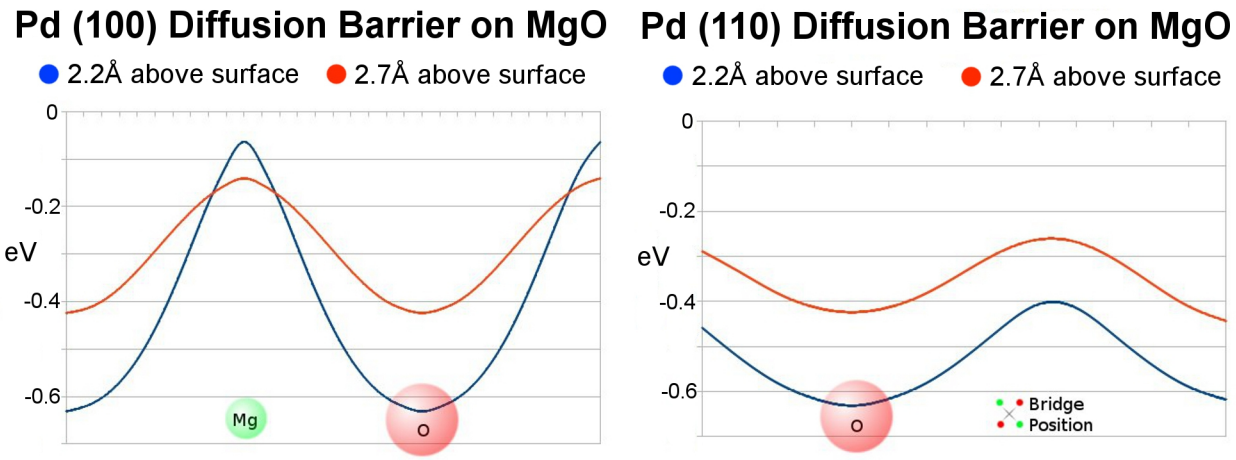

Figure 3.1: Diffusion barriers for Pd along the MgO(001) surface along the (100) and (110) directions as the Pd atom travels 2.2 Å and 2.7 Å above the surface. The barrier for motion when Pd travels at a greater height above the surface, the barrier for motion is reduced by nearly 50% in the (100) and (110) directions.

The fate of an incoming Pd atom depends greatly on the initial collision site. In particular, when Pd atoms landed within a radius of about 0.8 Å near O sites, they were immediately captured at the collision site (see Figure 3.2). These immobile adsorbing atoms were estimated to make up about 20% of the total incoming distribution. However, Pd atoms landing elsewhere on the surface were observed to exhibit significant transient mobility. These mobile atoms represented about 76% of the total distribution of incoming atoms. Finally, some of the Pd atoms that landed near Mg sites or bridge sites were

scattered from the surface. These scattered atoms were estimated to represent 4% of the total incoming distribution. The region around Mg or the bridge site near which Pd atoms were observed to scatter had a radius of 0.3 Å in my simulations. However, even within this region some of the Pd atoms gained enough lateral kinetic energy to avoid being scattered. The distribution of the average distances travelled by a Pd atom before thermalization at one site is summarized in Figure 3.2 as a function of lattice position. Deposited atoms that initially arive near a surface Mg atom were observed to gain enough mobility for some Pd atoms to travel up to 20 Å away on a 5 K surface.

Mg	22	20	12	9	5	0	0	**O**
22	20	11	15	9	5	0	0	0
20	11	16	16	11	7	5	0	0
12	15	16	13	S	5	7	5	5
9	9	11	S	S	S	11	7	9
5	5	7	5	S	13	16	15	12
0	0	5	7	11	16	16	11	20
0	0	0	5	9	15	11	20	22
O	0	0	5	9	12	20	22	**Mg**

Figure 3.2: The average mobility of Pd atoms adsorbing on MgO(001) with 0.4 eV incident energy in angstroms with respect to Mg and O lattice positions. Atoms landing near bridge positions were often scattered as indicated by a mobility of S. Incoming atoms landing near Mg were mobile while atoms landing near O were captured immediately. Areas corresponding to high Pd atom mobility are highlighted in green, areas of low mobility are highlighted in red, and areas where Pd atoms were scattered are indicated in white.

The trajectories of Pd atoms moving along the MgO surface were observed to exhibit a variety of patterns. Approximately 10% of the mobile atoms travelled along the (100) surface axes by passing directly over Mg atom lattice positions or in the (110) direction by passing directly over bridge sites in order to reach the next O lattice position. These atoms can be thought of as simply travelling over the diffusion barriers shown in Figure 3.1. The rest of the adsorbing Pd atoms moved *via* combinations of the (100) and (110) direction trajectory segments as the atom was deflected away from potential energy peaks

near Mg and toward wells near O. A representative trajectory of a typical transiently mobile adsorbing Pd atom is shown in Figure 3.3. The energy barriers in both the (100) and (110) directions decrease with increasing Pd atom height above the surface, as shown in Figure 3.1. This means that when the Pd atom is travelling at a significant height above the surface, it is less likely to be captured due to reduced corrugation. However, as the mobile Pd atom dissipates its excess energy, it settles closer to the surface in the potential energy well near O and eventually becomes thermalized. Furthermore, the energy barrier to diffusion is much greater in the (100) direction than in the (110) direction. As the Pd atom dissipates energy it will eventually be unable to overcome the (100) energy barrier and will prefer to be deflected towards the lower (110) barrier instead. The representative trajectory shown in Figure 3.3 contains both of these types of motions. The Pd atom in this trajectory landed above the Mg surface site and initially moves in the (100) direction. However, as it slowed down the Pd atom was observed to move predominantly in the (110) direction.

In the following sections I analyze the processes involved in Pd-surface collisions and energy dissipation in more detail to understand the origin of the transient mobility of Pd atoms and the character of the trajectories described above.

3.3.2 Energy and Momentum Transfer

I start by analysing the representative trajectory of an adsorbing Pd atom that was shown in Figure 3.3. The corresponding variations in Pd atom kinetic energy as it moved along this trajectory are presented in Figure 3.4. As Pd initially approached the surface near a Mg site, it came into range of attractive forces (see Figure 3.4) and began to accelerate until it reached the repulsive part of the interaction potential.

The initial collision process involves elastic surface deformation, which is remarkably similar to the mechanisms described by early calculations [94, 133]. This initial surface distortion depends directly on the incident energy of the incoming Pd atom. For example, in simulations where the Pd atom collided directly above an Mg site on the surface with

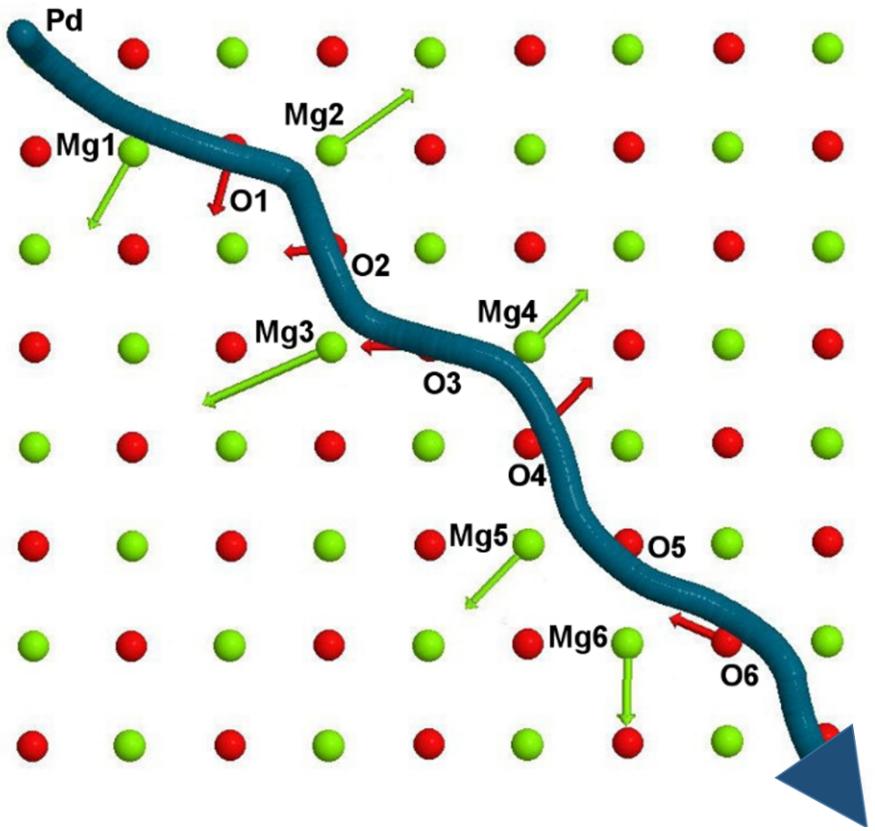

Figure 3.3: The trajectory of a Pd atom as it diffuses from the top left hand corner along the MgO (100) surface after adsorption. Mg atoms are shown in green, O atoms are shown in red, and the trajectory of the Pd atom is shown in blue. The adatom was deflected away from Mg atoms and towards O atoms resulting in a combination of (100) and (110) direction motions. The Mg and O atoms that experienced the greatest displacements due to interaction with the Pd atom are labelled. The lengths of these atomic displacement vectors were magnified by a factor of 20 for visibility.

an incident energy of 0.4 eV, the shortest Pd-Mg distance that I observed was 2.36 Å. The Mg atom was displaced downward by about 0.3 Å, as shown in Figure 3.5. The magnitude of this displacement is several times larger than the amplitude of zero-point vibrations of Mg ions in MgO at this temperature range.

During the collision process the Pd atom also gained some lateral momentum due to steering effects towards an attractive O atom while it momentarily displaced a nearby Mg atom due to repulsive interactions. These interactions resulted in a non-zero kinetic energy at the first minimum shown in Figure 3.5 as only the vertical component of velocity reached zero. When the surface relaxed, the Pd atom deflected away from the Mg ion with signifi-

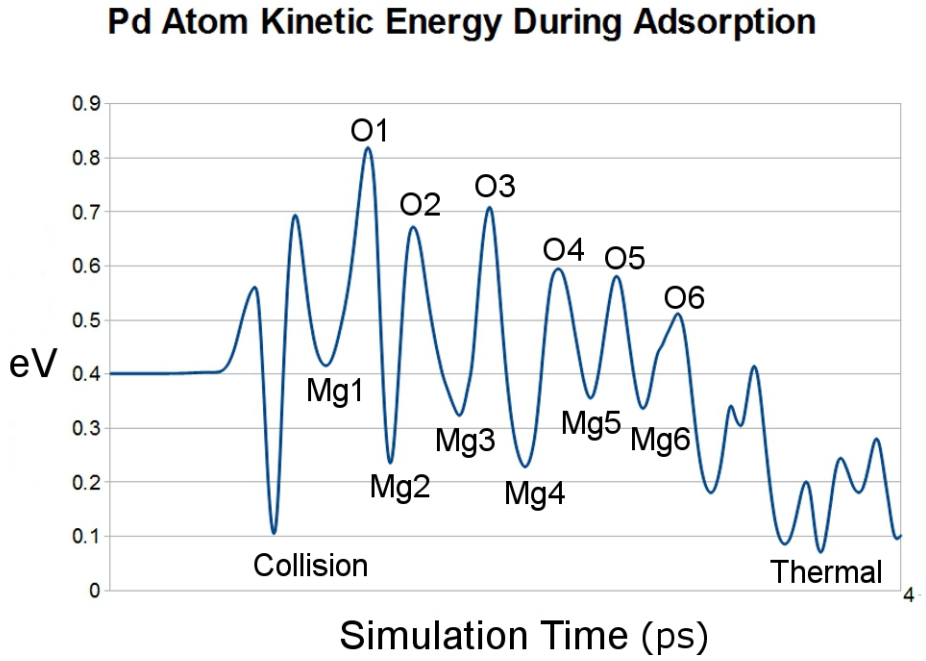

Figure 3.4: The kinetic energy of the Pd atom throughout the adsorption and thermalization process. The incoming atom initially possessed 0.4 eV of incident energy before colliding with the surface. It experienced velocity maxima when it moved towards attractive O atoms and minima as it was deflected away from repulsive Mg atoms. Eventually enough energy was dissipated and the Pd atom was thermalized and captured at an adsorption site above O.

cant lateral momentum and moved towards an attractive O atom, gaining kinetic energy in the process. The Pd atom then continued to move across the surface. It was deflected away from Mg atoms and reached a kinetic energy minimum each time as the components of its velocity were reversed. It then gained energy moving towards O atoms, reaching a kinetic energy maximum as it passed near each one. In each of these processes, part of the energy was dissipated by surface vibrations until the Pd atom became thermalized and was captured on the surface near an attractive O atom.

In contrast, Pd atoms adsorbing above an O site were observed to initially gain a large amount of adsorption energy before compressing the surface and reversing velocity. The minimum Pd-O distance at the turning point was observed to be 2.0 Å, with a 0.3 Å displacement of the O atom. However, the effects of lateral steering were negligible at these positions as the Pd was steered directly downward, generating very little lateral momentum.

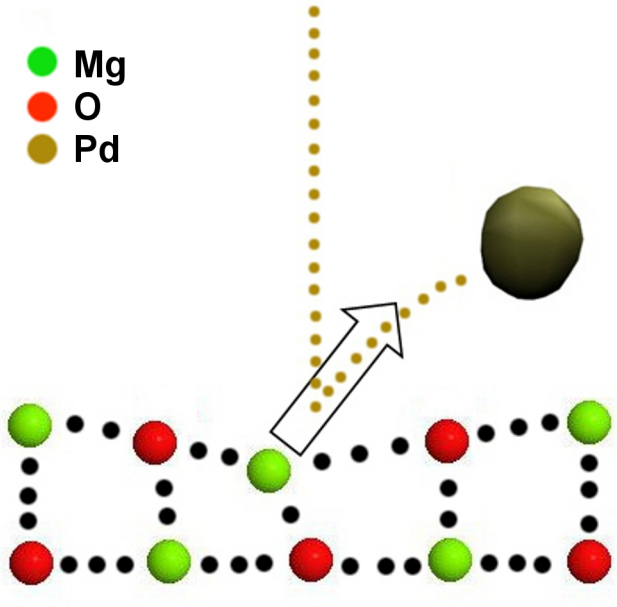

Figure 3.5: A schematic diagram showing how incoming Pd atoms compress the surface as they collide. The Mg and O surface atoms are displaced momentarily, absorbing energy from the Pd atom. A portion of the energy is then transferred back into the adatom in the direction indicated by the arrow as the surface relaxes.

Therefore the lateral momentum gained when Pd later reversed its velocity on the surface was nearly zero. Initially it moved up and down almost vertically before settling in the O potential well with insufficient energy to overcome the previously calculated barriers for motion (see Figure 3.4). Since the heavy Pd atom is strongly attracted to O, it moved together with the surface O atom on the return motion of the deformed surface to effectively dampen the surface oscillations. This efficiently dissipated most of the energy into surface phonons. This strongly inelastic process thermalizes Pd atoms very efficiently and prevents transient mobility, as is clearly seen in Figure 3.4. The dynamic behavior of incoming Pd atoms above an O surface site is remarkably similar to that predicted by simpler lattice models [134, 135, 136].

Transient mobility has often been previously attributed to a release of the latent heat during condensation or adsorption [69, 70, 91, 92, 93]. In my simulations, Pd atoms gained the most adsorption energy interacting with O surface sites rather than Mg sites and would be expected to gain the most mobility when adsorbing near O. However, the distance that these mobile atoms were able to travel before thermalizing was much greater when they

landed near Mg sites rather than O sites. Partitioning the velocity of the Pd atom into vertical and lateral components reveals that atoms adsorbing near Mg exhibit much higher lateral components of velocity on average than those adsorbing near O, as shown in Figure 3.6. I note that there is strong correlation between transient mobility and the lateral component of kinetic energy acquired by Pd during the collision process. This highlights the importance of momentum transfer in facilitating transient mobility. Another important factor is the efficiency of energy dissipation during the initial collision, which is much higher at the attractive O site in comparison to the repulsive Mg surface site [135, 136].

Mg	0.50	0.48	0.49	0.40	0.31	0.23	0.16	**O**
0.50	0.50	0.51	0.51	0.42	0.31	0.23	0.16	0.16
0.48	0.51	0.50	0.44	0.36	0.27	0.21	0.23	0.23
0.49	0.51	0.44	0.37	0.29	0.21	0.27	0.31	0.31
0.40	0.42	0.36	0.29	0.21	0.29	0.36	0.42	0.40
0.31	0.31	0.27	0.21	0.29	0.37	0.44	0.51	0.49
0.23	0.23	0.21	0.27	0.36	0.44	0.50	0.51	0.48
0.16	0.16	0.23	0.31	0.42	0.51	0.51	0.50	0.50
O	0.16	0.23	0.31	0.40	0.49	0.48	0.50	**Mg**

Figure 3.6: The maximum lateral velocity of the Pd atom after collision in eV with respect to Mg and O lattice positions with 0.4 eV incident energy. Lateral velocity after collision is greatest near Mg sites rather than O sites in contrast to adsorption energy. Sites resulting in high lateral velocity are highlighted in green while sites with resulting in low lateral velocity are indicated in red.

During the initial stages of the trajectory the Pd atom travels 2.7 Å above the surface where it interacts only weakly with the surface, resulting in greatly reduced energy barriers, as shown in Figure 3.1. When the kinetic energy of the Pd atom is greater than the energy barrier for diffusion, it will continue to move along the surface. However, after enough energy has been dissipated and Pd is no longer able to overcome these diffusion barriers, it will become trapped in an energy well in the vicinity of an O surface atom. As it oscillates above the O adsorption site the Pd atom will continue to exchange energy with the surface

until it becomes fully thermalized (see Figures 3.3 and 3.4).

3.3.3 Dependence on Deposition Conditions

In order to highlight the importance of incident kinetic energy in comparison to adsorption energy, I performed additional simulations at lower incident energy with the results shown in Figure 3.7.

Mg	20	8	5	0	0	0	0	**O**
20	8	5	0	0	0	0	0	0
8	5	5	0	0	0	0	0	0
5	0	0	0	0	0	0	0	0
0	0	0	0	0	0	0	0	0
0	0	0	0	0	0	0	0	5
0	0	0	0	0	0	5	5	8
0	0	0	0	0	0	5	8	20
O	0	0	0	0	5	8	20	**Mg**

Figure 3.7: The average mobility of Pd adsorbing on MgO (001) in angstroms with respect to Mg and O lattice positions with 0.005 eV incident energy. Atoms landing near Mg still move large distances away from the site of collision, but a much larger percentage of atoms are immobile when adsorbing with lower incident energy. Sites resulting in high Pd atom mobility are highlighted in green while sites with low mobility are shown in red.

At very low incident energies, the transient mobility of incoming Pd atoms was greatly reduced as the energy gained from the adsorption process alone was insufficient to facilitate Pd movement across the surface. Atoms adsorbing near the bridge sites no longer scattered and only those that adsorbed very close to Mg sites were able to move along the surface. With such low kinetic energy the adsorbing atoms were not able to hop over the necessary diffusion energy barriers. The exceptions observed near Mg surface sites can be attributed to the repulsive interaction between Pd and Mg which resulted in the Pd atom deflecting laterally at greater heights above the surface. These Pd atoms moving across the surface experienced a lower energy barrier as shown in Figure 3.1 and were still mobile. This data supports the idea that deflection and scattering play a larger role in the initial mobility than

adsorption energy. Furthermore, it indicates that higher incoming velocities may increase mobility. This is in contrast to metal-metal systems, where the effect of incident energy was thought to be insignificant [73], the magnitude of incident energy here is substantial compared to adsorption energy (0.4 eV vs. 1.0 eV in Pd-MgO compared to 0.4 eV vs. 2-5 eV in metal-metal systems).

In addition to incident energy, the incident angle of adsorption has been theoretically shown to have an impact on the percentage of trapped versus scattered atoms in scattering experiments [133]. To examine this effect I also performed molecular dynamics simulations of Pd atoms adsorbing near O sites at a 45 degree angle. Under these conditions, the average distance traveled by a transiently mobile atom increased significantly for atoms arriving in a (100) lateral direction along the Mg-O bond (from 0 Å to 12 Å). Atoms arriving in a (110) lateral direction along the lowest energy pathway for diffusion over the bridging site were seen to exhibit an even larger increase (from 0 Å to 20 Å). These collision sites above O represent the largest diffusion barrier that the Pd atom must overcome in order to begin moving along the surface. Thus all other collision sites on the surface can be expected to exhibit even greater increases in mobility. These results indicate that incident angles play a significant role in determining the mobility of adsorbing atoms on oxide surfaces.

Many calculations have been made regarding the kinetics of various processes involving Pd on MgO [51, 56] and good experimental agreement was obtained without including the effects of transient mobility. This prior data, however, consists mainly of experiments performed at higher temperatures. As the surface temperature increases other effects begin to overshadow transient mobility and the atoms are able to diffuse thermally instead. To check the effect that surface temperature has on transient mobility I performed a series of simulations for surface temperatures of 5 to 280 K. Analyzing the energy transfer showed that increased surface temperature resulted in a small reduction in the amount of kinetic energy in lateral direction gained during adsorption, shown in Figure 3.8. This translated into a small reduction of the average distance travelled by Pd atoms impinging on the

surface at Mg sites at 120 K with respect to that at 5 K.

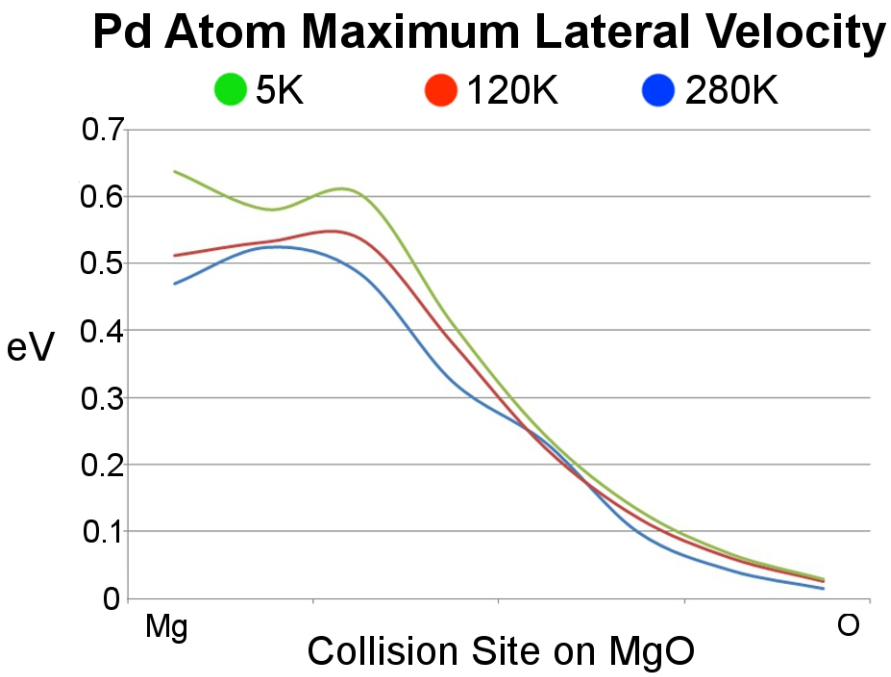

Figure 3.8: The Pd atom's maximum lateral velocity as it adsorbs with 0.4 eV incident energy onto surfaces of various temperatures is plotted along an Mg-O bond on the surface. Higher surface temperatures show a small reduction of the lateral kinetic energy gained by Pd atoms during adsorption.

These results are similar to prior experiment and theory of Hg atoms colliding with the MgO (100) surface [122]. As surface temperature was increased, a slight increase in Hg to surface energy transfer was observed. At higher temperatures the distance travelled by Pd due to thermally activated hopping mobility also increased. These results indicate that the role of transient mobility diminishes as surface temperature increases. In order to observe transient mobility, experiments should be performed at low temperatures to avoid thermal effects and promote lateral momentum transfer.

3.3.4 Energy Dissipation

The distance travelled by Pd after collision directly depends on how quickly it can dissipate kinetic energy. As the Pd atom travels past, the average positions of nearby vibrating surface atoms are altered significantly by attractive (Pd-O) and repulsive (Pd-Mg) forces,

as shown in Figures 3.3 and 3.9. After the Pd atom has moved on, the surface atoms relax back into their original positions. These large reversible displacements are anharmonic and a significant part of the Pd atom's kinetic energy is dissipated into crystal vibrations, as can be seen in Figure 3.4. The mechanisms of energy dissipation and related atomic displacements have been discussed in many publications in the context of atom-surface collisions [137, 138] and Atomic Force Microscopy [139, 140].

Molecular dynamics simulations allowed me to attain an insight into the dynamics of displaced surface ions. The surface relaxation has typically two regimes. At the start of the flight in Figure 3.3, the Pd atom is scattered from the surface Mg ions and moves in a zigzag trajectory along (100) surface directions. The accompanying O and Mg atom displacements are large (Figure 3.9) and directed predominantly perpendicular to the trajectory (Figure 3.3). The corresponding displacements of O1, O2, and O3 as a function of Pd position exhibit single loops shown in Figure 3.10.

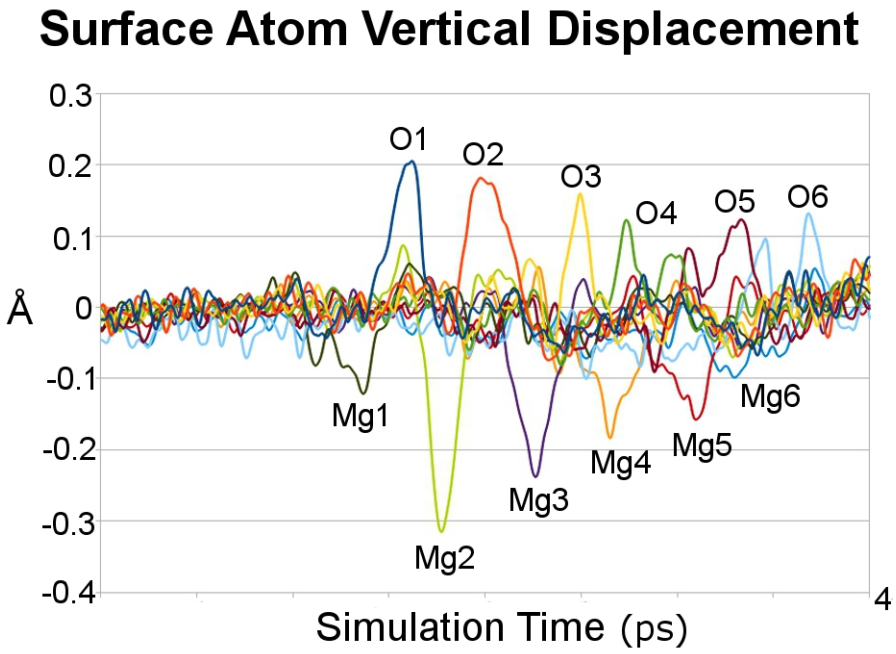

Figure 3.9: The height of O and Mg atoms with respect to the surface is shown during adsorption and thermalization. As the Pd atom interacts with O atoms, they are pulled up to 0.2 Å out of the surface towards it while Mg atoms are pushed up to 0.3 Å into the surface away from the adatom. Both O and Mg atoms return to their original lattice positions on the surface after the Pd atom has passed.

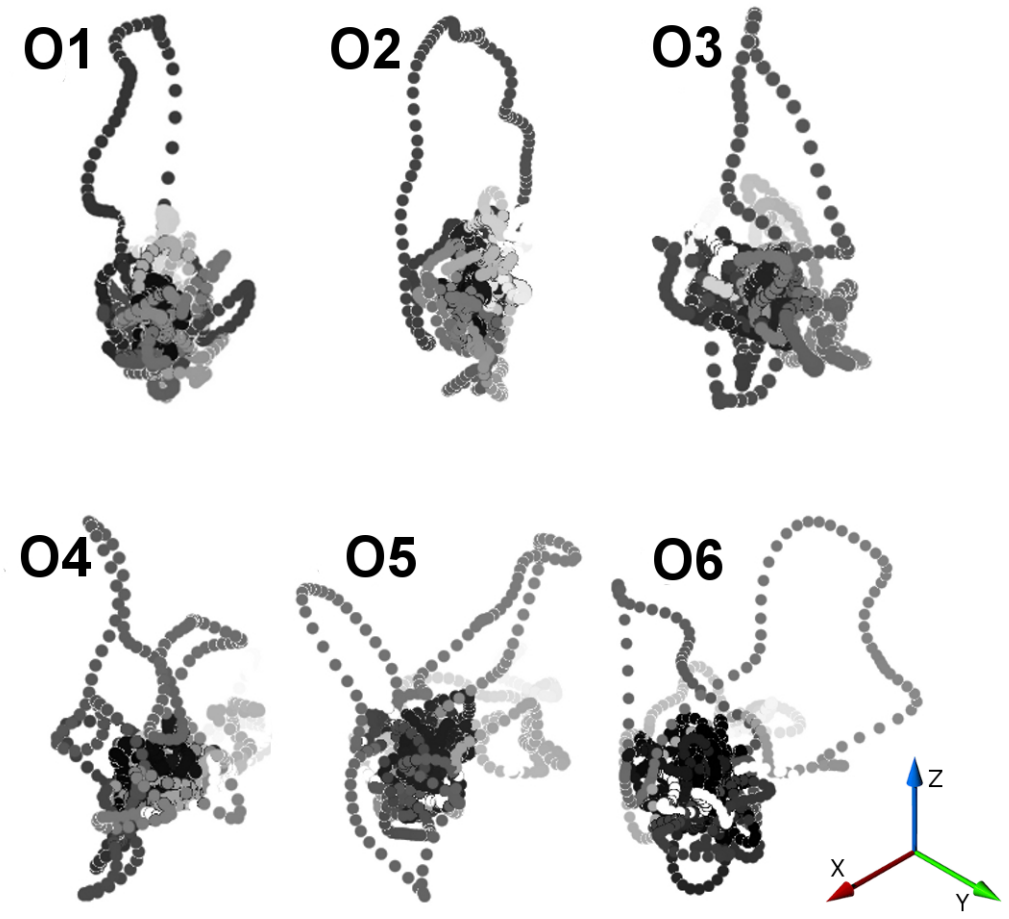

Figure 3.10: A side view of the positions of O atoms on the surface during adsorption and thermalization of a Pd atom is presented. Light regions indicate O positions prior to interaction with the adatom while dark regions indicate O positions after the Pd atom has passed. Two regimes are illustrated as O1-O3 show single loops while O4-O6 show double loops as the Pd atom slows down and O is more able to adjust to its position during the interaction.

Towards the end of the trajectory, however, the Pd atom‘s kinetic energy is much lower, as it moves along the (110) surface axis. This regime is characterized by double loops in the trajectories of O4, O5 and O6 shown in Figure 3.10. In these cases the surface O atoms adjust to the Pd position first by moving towards it and then settling back near their equilibrium lattice sites when the Pd atom moves directly above them. As the Pd atom leaves the vicinity of the O surface site, the O atoms are displaced outward a second time before reversing velocity and returning to their original lattice positions. The asymmetries of these displacement loops are characteristic of rate dependent hysteresis which has been

attributed to dissipative effects such as friction and is associated with power loss [141] in physical systems.

The energy required to displace O and Mg ions from their lowest energy positions during these surface deformation processes is absorbed from the mobile Pd atom. In contrast to the mechanism for O displacement, Mg displacement decreases as Pd atom velocity decreases and does not exhibit two energy dissipation regimes, as shown in Figure 3.9. This is due to the trajectory of the Pd atom deviating less from preferred pathways near O sites as it slows down. At the end of the trajectory, the Pd adatom interacts less with Mg atoms as it becomes confined to areas near O atoms.

It is interesting to note that as the surface O ions are displaced and relaxed, their trajectories exhibit saw tooth patterns similar to that found in the stick-slip Prandtl-Tomlinson model often used for understanding friction at atomic scale. This is also manifested in a characteristic increase in velocity that corresponds to the slip event. This is illustrated in Figure 3.11 where the velocity plot for O1 shows a sharp increase at the end of the Pd-O interaction, indicative of the slip portion of stick-slip motion, which can be clearly seen in Figure 3.10. Similar slip events occur at other O sites as well. The strain energy is then dissipated into surface vibrations.

3.4 Discussion and Conclusions

My molecular dynamics simulations of Pd atom deposition at a prototypical oxide substrate (MgO) exhibit a variety of adsorption-diffusion events that can be compared to prior work to gain additional understanding.

The initial energy transfer and deformation of the MgO surface are qualitatively similar to what is described in simpler atomistic models [94, 134, 135, 136] pertaining mainly to atomic collisions with metallic surfaces. A hot spot forms on the surface where the adsorbing atom lands [94], transferring a large percentage of translational kinetic energy to the surface. The focus of prior work has been on the energy transfer away from this hot spot

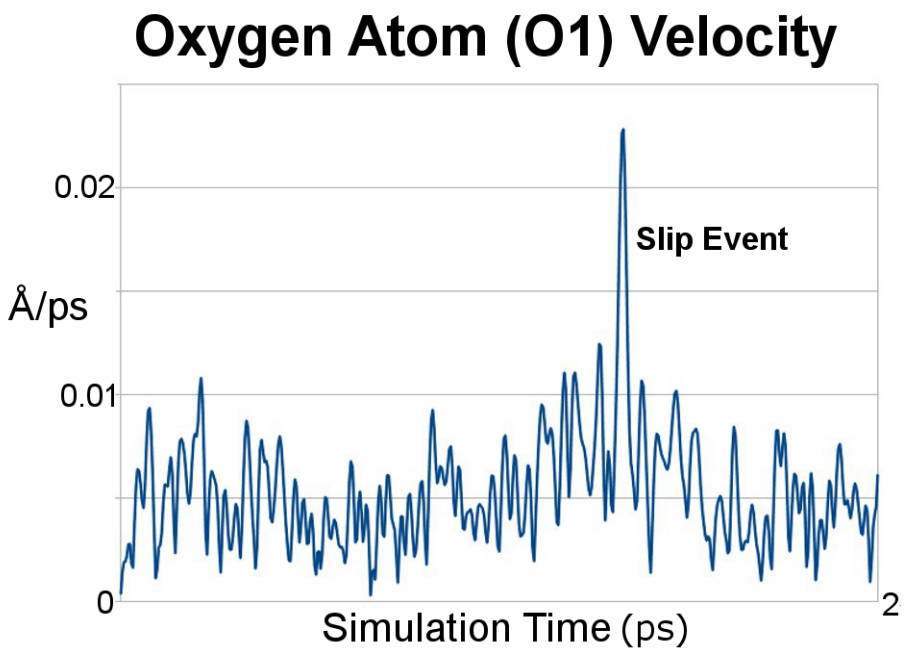

Figure 3.11: O atoms on the MgO surface during simulation of Pd adsorption and thermalization exhibit a sharp increase in velocity at the end of the Pd-O interaction as the adatom passes by. The O atom in this figure corresponds to O1 in Figure 3.3. This increase in velocity is similar to that observed in stick-slip motion.

and on scattered atoms. What is important to consider in the context of transient mobility, however, is the resulting lateral motion of the adatom, enabling it to begin traveling across the surface. When adsorbing on top of an oxygen binding site, even though the energy gained through the Pd-surface interaction is much greater, the Pd atom does not gain a significant lateral component to kinetic energy. It is able to dissipate energy very efficiently and thus does not exhibit transient mobility. This indicates that the dominant factor in enabling mobility is deflection rather than energy gain through adsorption. This effect is also confirmed by my results for smaller incident angle deposition.

The mobility of Pd following adsorption can also be examined in the context of thermal diffusion mechanisms. When comparing trajectories of Pd on MgO with long jump diffusion mechanisms several similarities are quickly noticeable. Long jumps have been studied extensively [142, 143, 144, 145, 146, 147, 148] and are defined as a sequence of successive jumps during which the velocity of the adatom is not reversed and it does not spend significant time near any one adsorption site. Additionally, long jumps exhibit correlated

behavior in that the subsequent hops are influenced by the previous ones rather than being governed by random hops. Many of these properties are shared by atoms exhibiting transient mobility after adsorption. The likelihood of long jumps for Pd on MgO has in fact been predicted to be significant at room temperature [144]. Energy transfer between the adatom and the surface will have an impact on both long jumps during diffusion and transient mobility. In both cases, the faster the adatom can transfer energy to the surface, the faster it will thermalize at a binding site. It has been shown previously that energy transfer between the adatom and surface has an effect on long jumps. It has also been suggested [142, 143, 144, 148, 149] that relatively low diffusion barriers, relatively low adsorption energies, and a large difference between the frequencies of adatom motion and surface phonon vibrations all contribute to less efficient energy transfer. These effects predict that Pd on MgO should have significantly more mobility than metal on metal systems at high surface temperatures. In contrast, my simulations predict a decrease in lateral kinetic energy and hence transient mobility with increasing surface temperature. This effect may be primarily due to long jumps gaining their initial energy from interacting with surface phonons. This initial energy will be reduced at lower temperatures. In contrast, atoms exhibiting transient mobility gain initial energy from the collision process which generates lateral velocity via momentum transfer.

Finally, the mechanism of energy dissipation in which the interaction of Pd with the surface O atoms exhibits stick-slip behavior is similar to the Prandtl-Tomlinson model of friction [150]. The Prandtl-Tomlinson model is based on a simple mechanical picture where a tip atom is attached via a spring to an object sliding over the surface. Due to the interaction with surface atoms, the sliding atom sticks in a potential energy well until the lateral force of the spring is sufficient to cause a jump into the neighboring site. The energy provided by piezo scanning the tip above the surface at a constant force [151] is dissipated into the tip and surface phonons. Similarly, the Pd atom sticks to the surface O ions, causing their displacements, and the ensuing slip into the energy minimum is accompanied by the energy dissipation into surface phonons.

To summarize, my molecular dynamics simulations at conditions aimed at modeling experimental deposition show that a large percentage of Pd atoms arriving on a MgO (100) surface are mobile even at 5 K. Depending on where the adatom adsorbs, varying amounts of its kinetic energy can be converted into the lateral motion. The atom then dissipates energy as it travels along the surface via a stick-slip like mechanism until it has lost enough energy and becomes trapped. The mobility of the adatom is similar in many ways to long jumps in surface diffusion. Long jumps, however, gain energy by interacting with phonons on the surface and as surface temperature decreases they disappear. Transient mobility on the other hand has been shown to be more dependent on scattering or deflection at an Mg site than energy gained from interacting with the surface phonons and must be observed at low surface temperatures. Finally, the deposition angle and incident energy have been shown to significantly enhance transient mobility.

Chapter 4

Adsorption and Mobility of Single Molecules: Co-Salen on NiO(001)

Aims: This chapter covers my results from studying Co-Salen molecules on NiO(100). NCAFM experiments performed using metallic tips were able to image single Co-Salen molecules on NaCl(001) and NiO(001), however, theoretical studies were needed to explain the differences observed in these two sets of experiments. Section 4.1 gives an introduction including a description of prior studies performed on the Co-Salen molecule on NaCl(001). Section 4.2 briefly describes the experimental methods used by A. Schwarz and J. Grenz to perform NCAFM measurements. Section 4.3 presents an overview of the theoretical methods I used to perform electronic structure calculations on this system. Section 4.4 describes the results covering adsorption, electronic structure, diffusion, and imaging of Co-Salen on the NaCl(100) and NiO(100) surfaces. Finally, discussion and conclusions to this work are presented in Section 4.5.

Methods: In order to accurately represent the NiO(001) surface I used a hybrid functional and employed an extensive basis set to avoid basis set superposition error (BSSE). The combination of these two factors, however, results in a prohibitively large increase in computational expense. This expense was mitigated by generating auxiliary basis sets and using the auxiliary density matrix method (ADMM). These methods were previously

described in Chapter 2.

Results: Density functional theory (DFT) calculations predict that the molecule adsorbs with the central Co atom on top of an oxygen ion and is in the lowest energy configuration aligned ± 4° away from the <110> directions, dependent on the chirality of the molecule. Combining my theoretical predictions with experimental data allowed me to identify bright spots in NCAFM images as oxygen sites on NiO(001) and determine the exact adsorption geometry and position of the molecule. Additionally, I calculated the lowest energy barriers for diffusion of the Co-Salen molecule on NiO(100) and compared the results to experimental data. Comparing these results with previous studies of Co-Salen on NaCl(001) illustrate that minor differences between substrates can result in qualitative differences in the character of adsorption of individual molecules and the ensuing growth of thin films.

4.1 Introduction and Prior Work

After investigating the properties of single atoms deposited onto the MgO surface, I moved on to study larger molecules adsorbed to the NaCl and NiO surfaces. I initially introduced the importance of studying such systems in the context of friction and wear. However, the properties of these systems are of wide interest and critical to many other fields of surface science. For example, it is necessary to understand the interaction between the molecule and the surface in the fields of molecular electronics [152, 153] and magnetism [154] where the electronic and magnetic properties of the molecule may be heavily influenced by the surface. Studies show that it is possible to tune the band gap of insulating surfaces by using deposited layers of organic molecules [155, 156, 157, 158]. These materials could then be used in dye sensitized solar cells. The general knowledge gained from studying single Co-Salen molecules on NiO(001) can provide insight that is applicable to a wide array of applications.

In this chapter I present my results on the properties of single Co-Salen molecules adsorbed onto NiO(001). The Co-Salen molecule ($Co(C_{16}H_{14}N_2O_2)$) is a metal-organic complex that is known for the ability to coordinate oxygen. It is a paramagnetic metal organic Schiff base complex that contains one square planar Co(II) at the center. This Co atom is bonded to two N atoms and two O atoms in a banana shaped structure with aromatic rings on either side, as shown in Figure 4.1. The molecule is chiral and possesses a C_2 symmetry due to deformation of a C_2H_4 bridge between the two N atoms..

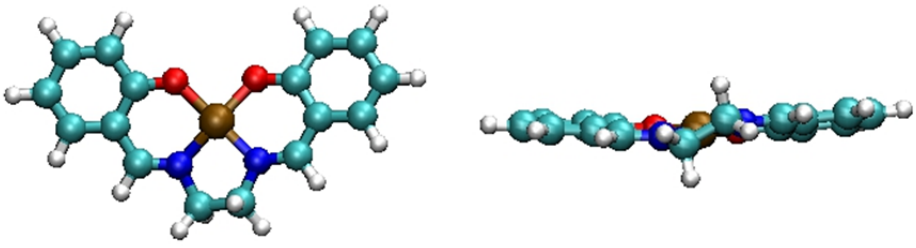

Figure 4.1: The Co-Salen ($Co(C_{16}H_{14}N_2O_2)$ molecule is shown above. The free molecule is chiral due to the deformation of a C_2 bridge between two N atoms and possesses a Co center bonded to two N atoms and two O atoms. C atoms are shown in light blue, N atoms in dark blue, O atoms in red, H atoms in white, and Co atoms in brown.

The structure of the Co-Salen molecule is similar to many friction modifiers and wear inhibitors, most notably MoDTC [1] and ZnDTP [2]. It was previously deposited onto the (001) surface of bulk NaCl and studied using NCAFM with a Cr coated tip [3]. DFT calculations were used to identify the sub lattice, confirm the adsorption site and determine the orientations of the molecule on the NaCl surface. A total of 16 orientations on the surface aligned in the <110> and <100> directions were found in agreement to experiment.

In this study, Co-Salen molecules were similarly deposited onto the (001) surface of bulk NiO. However, despite the fact that both NaCl(001) and NiO(001) are bulk insulators with the same simple cubic crystal structure, differences in orientations, growth, and mobility were observed. I used DFT to characterize the electronic differences that arise due to subtle changes in surface geometry and discuss the implications these differences have on the adsorption geometry, diffusion, and film formation of single molecules. One critical aspect of this work is that it provided the opportunity to verify the DFT methods I employed using experimental observables, lending credibility to my unobservable predictions.

4.1.1 Noncontact Atomic Force Microscopy (NCAFM)

The study of molecular structures on surfaces provides a unique challenge that is well met by scanning probe methods. Organic molecules can often self-organize or self-assemble from molecular components into large scale physical components. However, these structures often represent states that can be easily deformed. In many cases, even thermal fluctuations are sufficient to drive the rearrangement of these structures, making it difficult to experimentally probe the system without changing its properties. These materials stand in contrast to traditional condensed matter systems, where the properties of a material can often be predicted because the components organize into stable crystalline lattices. While soft matter systems in general can be studied using a variety of techniques [159] including dynamic light scattering, various types of spectroscopy, the use of neutrons and x-rays, optical tweezers, electron microscopy, scanning tunneling microscopy, and atomic force microscopy, these challenges are well met by scanning probe methods in particular.

Scanning probe microscopy began when the scanning tunneling microscope (STM) was invented in 1981 by Binnig and Roher [160] who won the nobel prize in physics for the invention in 1986. However, since the STM relies on tunneling current, only conducting tips and samples may be used. This makes studying bulk insulators a challenge. Fortunately, in 1986 Binnig, Quate, and Gerber developed the atomic force microscope (AFM). With AFM, the force experienced by the tip due to interactions with the sample is measured instead, removing the requirement for conducting materials. The AFM is a widely used experimental technique for studying surfaces and noncontact AFM (NCAFM), a mode of operation designed to prevent destructive contact between the tip and the sample, is often used to study deposited molecules or films. Indeed, there have been many successful studies of individual molecules, molecular aggregates and complex structures on insulating surfaces using NCAFM in the past.[161, 162, 163, 164, 165, 166, 167, 168, 169, 170, 171]. However, the interpretation of experimental data is difficult and systematic high resolution studies are still rare.

The NCAFM techniques discussed in this chapter and in the rest of the thesis focus on measurements produced in the frequency modulation mode introduced in 1991 by Albrecht *et al.* [172] In this mode, the cantilever is oscillated above a sample at a constant amplitude while changes in frequency are recorded. To accomplish this, the deflection of the cantilever is monitored by reflecting a laser beam off the cantilever into a photodiode detector. The position of the cantilever is then precisely controlled using piezo-electric scanning devices. In this way, the surface can be scanned to produce a map of the tip-sample interactions which can be viewed as an image of the surface. These images can then be interpreted and compared with theoretical predictions.

4.2 Experimental Methods and Data

Co-Salen molecules were deposited onto the NaCl(001) and NiO(001) surfaces directly in the low temperature microscope using a miniaturized crucible and imaged using NCAFM

by A. Schwarz and J. Grenz at the University of Hamburg. Supersharp Si cantilevers (2 nm nominal tip radius) [173] were coated *in-situ* with a few nanometers of Cr to prepare the tip. The contact potential difference (CPD) between the tip and sample was determined by recording $\Delta f(U_{\text{bias}})$-curves. $U_{bias} = U_{CPD}$ was applied between tip and sample to minimize long-range electrostatic interactions. As previously described [174], these curves were also used to characterize the metal coated tips. More detailed information about the methods used to deposit and image Co-Salen molecules on NaCl(001) and NiO(001) can be found in previous publications [3, 175].

While images of Co-Salen molecules on NaCl(001) and NiO(001) share some similarities, there were several noticeable qualitative differences between the two surfaces. The adsorption site and geometry of each Co-Salen molecule can be identified using the simultaneously imaged anions on the surface, as shown in Figure 4.2A.

This evaluation can be made unambiguously since the Cr coated tip is attracted to the surface anions, resulting in bright spots in the image [174, 3, 175]. On NaCl(001), Co-Salen was observed to adsorb in 16 Co-Salen orientations on the surface. These corresponded to aligning the axis of the molecule in either the <100> or <110> directions [3] with two 5 ° offsets in each direction due to the asymmetry of the molecule, as shown in Figure 4.2D.

The geometry and orientation of Co-Salen on NiO(001) was unambiguously determined in the same way as on NaCl, as shown in Figure 4.3. On NiO(001), however, analysis of the experimental data revealed that Co-Salen molecules were oriented in 8 orientations on the surface rather than 16. These orientations corresponded to adsorption geometries where the axis of the molecule was aligned in the <110> directions, as shown in Figure 4.3.

In the experimental images shown in Figure 4.2B and 4.3B, the number of molecules observed in each configuration is not equal. However, since the sample size is small, these results are within a reasonable deviation from the expected value for an even distribution of orientations. Furthermore, when higher concentrations of Co-Salen molecules are deposited, they are observed to exhibit island growth on NaCl and layer by layer growth on NiO. These results cannot be explained through interpretation of the experimental im-

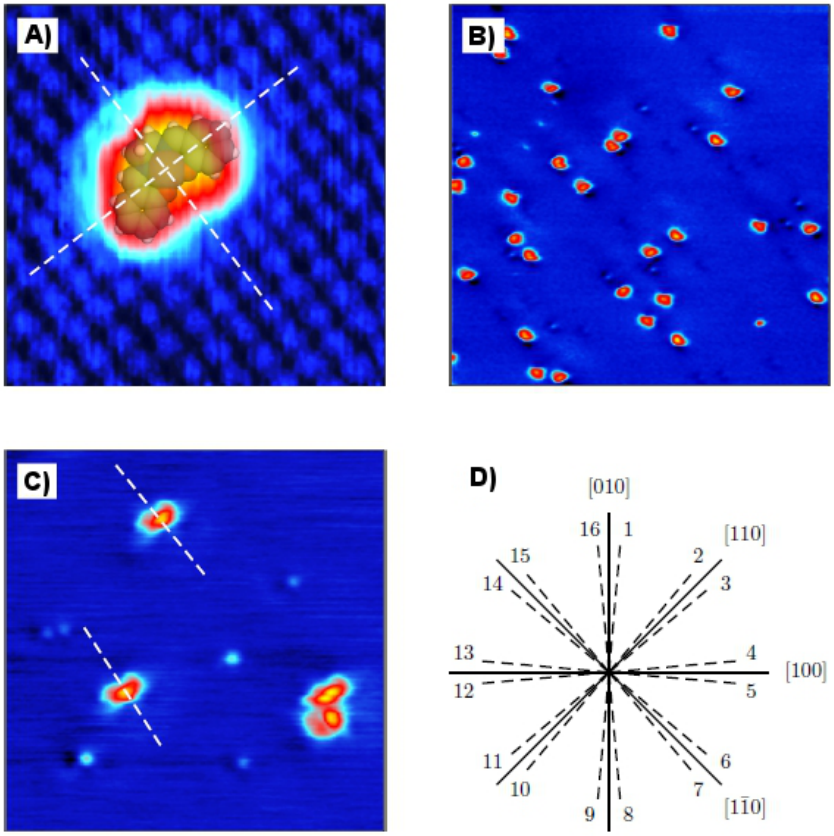

Figure 4.2: The experimental distribution of Co-Salen molecules on the NaCl(001) surface illustrates 16 possible orientations of the molecule corresponding to the <100> and <110> direction orientations. A) The adsorption site and geometry can be unambiguously identified using the simultaneously imaged surface anions. B) A larger area of the surface with many Co-Salen molecules. C) A closer look at several of the Co-Salen molecules illustrates their orientations with respect to the surface. D) Analysis of all the observed molecules shows that Co-Salen exhibits 16 possible orientations on NaCl(001).

ages alone, so I used DFT to characterize the interactions between Co-Salen and the two surfaces.

4.3 Theoretical Methods

It would have been ideal to perform my DFT calculations for Co-Salen on NiO(001) using the same methods as previous calculations for Co-Salen on NaCl [3]. However, due to the complexity of the NiO(001) system this was not possible. In particular, the lattice constant of NiO is smaller than that of NaCl and more surface atoms were required in order to generate a slab large enough to accommodate the Co-Salen molecule. This was further

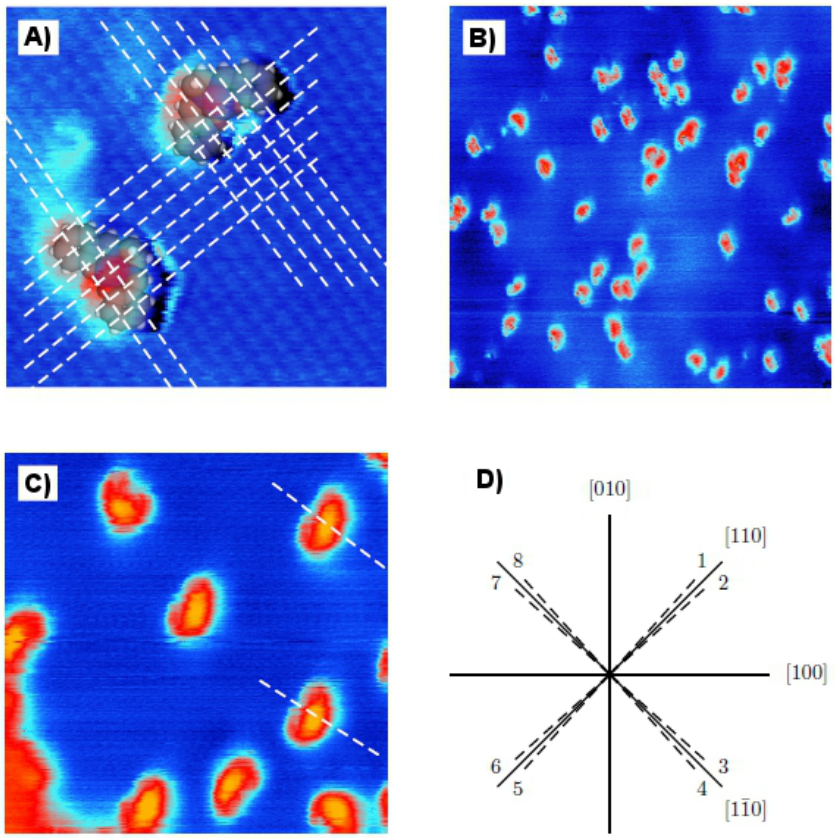

Figure 4.3: The experimental distribution of Co-Salen molecules on the NiO(001) surface illustrates a total of 8 possible orientations of the molecule corresponding to orientations in the <110> directions. A) The adsorption site and geometry can be unambiguously identified using the simultaneously imaged O atoms on the surface. B) A large area of the NiO(001) surface showing many Co-Salen molecules in a variety of configurations. C) A closer look at several Co-Salen molecules illustrates their orientations with respect to the surface. D) Analysis of all the observed molecules shows that Co-Salen exhibits 8 possible orientations on NiO(001).

complicated by the fact that NiO is antiferromagnetic at temperatures below 525 K. A much larger periodic unit cell (4 atoms along each lattice vector) is needed to properly reproduce the alternating pattern of Ni spin states. In order to meet these computational challenges, I performed DFT simulations using the CP2K code and the efficient mixed Gaussian and plane waves approach [13] (GPW) as described in Chapter 2. These calculations included geometry minimizations to find the lowest energy adsorption geometries on the surface and calculations to estimate barriers for diffusion and rotation of the molecule. In order to reasonably represent the electronic structure of NiO(001) and ensure comparability with prior calculations on NaCl, I selected the B3LYP [7, 8] hybrid functional.

The extensive MOLOPT basis set [19] was used to minimize basis set superposition error. These basis sets were derived to be used with psuedopotentials proposed by Goedecker, Teter, and Hutter (GTH) [18]. Using pseudopotentials describes only the valence electrons (1 H, 4 C, 5 N, 6 O, 17 Co, and 18 Ni valence electrons) and reduces the number of electrons, basis functions, and primitive Gaussians per atom that must be included in the calculation. Calculations of the Co-Salen molecule on the NiO (100) surface using the MOLOPT basis set and the B3LYP hybrid functional have a BSSE of less than 0.02 eV. The expense of using a hybrid functional combined with an extensive basis set was mitigated by employing the Auxiliary Density Matrix Method (ADMM) [17]. A 3 layer 288 atom NiO(001) slab was selected by increasing the size of the cell until adsorption energy converged. This ensures that interactions between periodically translated Co-Salen molecules were negligible. Finally, a 400 Ry plane wave cutoff was selected by similarly increasing it until adsorption energy converged. Finally, I employed the semi-empirical dispersion correction method [176] described in Chapter 2. In this work Ni and Cr parameters were unavailable and the atoms were approximated as Ar. Ar was selected as a reasonable approximation for the Ni ion. All other elements were assigned default values. Examples files for optimizing a Co-Salen molecule on the NaCl and NiO surfaces using CP2K can be found on the supplementary disk attached to this thesis.

4.4 Results

4.4.1 Method Verification

Before studying the Co-Salen molecule on NiO(001), I first had to verify that the methods selected are able to accurately reproduce the electronic structure and geometry of both the Co-Salen molecule and the NiO surface. In Chapter 2 I evaluated the differences between performing a full DFT calculation on small fitting sets and employing the ADMM using optimized auxiliary basis sets. The differences in total energy that I calculated were negligible (10 meV) and the method was able to produce good one electron energy levels

as well. In this work I performed an additional evaluation of the ADMM directly on the Co-Salen molecule. My results on the Co-Salen molecule using ADMM indicated an error in total energy of less than 5 meV when compared to using only a primary basis set with no observable changes in the geometry of the gas phase molecule. This confirms that the methods I have chosen are indeed able to accurately represent the Co-Salen molecule and the NiO(001) surface.

Using the MOLOPT basis set and the B3LYP hybrid functional, I calculated the band gap of a clean NiO(001) surface to be 3.6 eV. This value is comparable to a prior experimental value of 4.3 eV [177]. My calculations produced a negligible surface rumpling of less than 1%, which corresponds to a Ni-O bond length deviation of less than 3% in the surface layer. These results are also in agreement with prior experimental results [178]. This demonstrates that the selected basis set, functional, and system size are able to produce accurate surface properties. Furthermore, these methods result in a BSSE of less than 0.1 eV when considering a Co-Salen molecule adsorbed onto NiO(001).

Since one of the primary objectives of this study was to explain differences observed between a previous study performed on the NaCl(001) surface [3] and new experimental data collected on the NiO(001) surface, my calculation methods had to be tested to ensure that they indeed produce comparable results to prior work. The simplest way of accomplishing this was to calculate the properties of Co-Salen adsorbed onto the NaCl(001) surface and compare my results to the previous theoretical and experimental study [3].

Consequently, I treated the Co-Salen molecule on NaCl(001) and was able to reproduce the previously obtained minimum energy configurations obtained using embedded cluster techniques [3]. These included energy minima corresponding to geometries where the Co-Salen molecule was oriented in the <100> and <110> directions with the <110> orientation of Co-Salen being the lowest in energy. The adsorption energy in this lowest energy configuration was calculated to be 0.60 eV which can be considered as a sum of several contributions. The total adsorption energy for Co-Salen on NaCl represents contributions of 0.02 eV from BSSE, 0.18 eV from vdW (semi-empirical dispersion corrections),

and 0.42 eV from DFT. These values are comparable to the results obtained from previous calculations that produced an adsorption energy of 0.68 eV which was similarly decomposed into 0.16 eV from BSSE, 0.35 eV from vdW, and 0.47 eV from DFT. These results are summarized and compared in Table 4.1. These results are in good agreement with the previous work, however, the Co to surface distance produced by my calculations is shorter by about 0.4 Å.

	NaCl Prior Work	NaCl Current Work
Lattice Constant	5.65 Å	5.65 Å
Adsorption Energy	0.68	0.60 eV
BSSE	0.16 eV	<0.02 eV
vdW Contribution	0.35 eV	0.18 eV
DFT Contribution	0.47 eV	0.42 eV
Co to Surface Distance	3.4 Å	3.0 Å

Table 4.1: The properties of Co-Salen on NaCl obtained previously and with the current method. The contributions from vdW corrections, DFT, and the BSSE in each calculation are compared. Note that the BSSE calculation was performed for the full system and the effect cannot be assigned to vdW or DFT contributions of the interaction.

After demonstrating that the methods I chose to treat Co-Salen on NiO(001) were able to reproduce previous results on NaCl(001), I proceeded to compare the differences in the character of bonding, adsorption geometries, and diffusion between the two systems. The new methods and basis set employed predicted a larger deformation of the adsorbed molecule with the Co complex closer to the surface and the aromatic rings farther away from the surface. However, the binding energy, minimum energy adsorption geometry, and the average height of the molecule with respect to the surface plane all remain comparable.

4.4.2 Differences in Adsorption Geometry

After verifying the methods used to treat the Co-Salen molecule, NiO(001), NaCl(001), and the adsorbed systems, I moved on to study the adsorption geometry of Co-Salen on NiO. The adsorption geometry of a single Co-Salen molecule on the NiO(001) surface was calculated and compared to prior work on the NaCl surface in order to explain the experimentally observed differences.

The Co-Salen molecule was initially positioned above NiO with the plane of the molecular board parallel to the surface plane. In order to account for all the possible stable adsorption geometries, I considered a wide range of other starting geometries as well. These additional configurations were generated by rotating the molecule in a clockwise direction around the Co atom, translating the molecule in increments of 0.01 nm along the <100> direction, and similarly translating the molecule along the <110> direction. The molecular geometry was then minimized by allowing all the atoms within Co-Salen and the first two layers of NiO to relax. In the lowest energy configuration the Co-Salen molecule was orientated in the <110> direction with the Co atom directly above a surface O ion and the two molecular O atoms above Ni surface ions. This configuration can be seen in Figure 4.4.

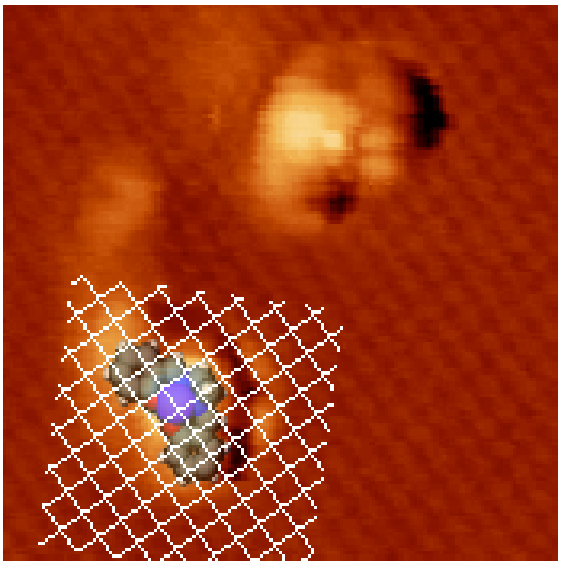

Figure 4.4: $(5.5 \times 5.5)\,\mathrm{nm}^2$ high-resolution NCAFM imaging showing two Co-Salen molecules along with the atomically resolved substrate. The grid indicates the positions of bright spots in relation to the half-transparent ball model fit to one Co-Salen molecule. This demonstrates that the molecule adsorbs with its central Co atom on top of bright spots on the surface, identifying them as O atoms. Parameters: Deposition at 27 K and imaging at 8 K with Δf = -6.1 Hz, $c_z = 147\,\mathrm{N/m}$, $A = 4.8\,\mathrm{nm}$, $f_0 = 188\,\mathrm{kHz}$, $Q = 261909$.

In Figure 4.4, the apparent height, length, and width of the molecule were estimated to be 180 pm, 1.8 nm, and 1.0 nm, respectively. These values are comparable to the expected values of 200 pm, 1.3 nm, and 0.6 nm. However, this is not surprising when considering

that NCAFM images always represent a convolution of the tip and the sample. A ball model of the molecule was superimposed over the NCAFM image in order to illustrate the predicted adsorption geometry. Additionally, a grid overlay is shown which corresponds to the positions of bright spots on the surface and indicates the position of O atoms on the NiO(001) substrate. These bright protrusions can be unambiguously identified as negative ions due to the nature of the metallic tip. This will be further discussed in Chapter 5. Since the tip exhibits a dipole moment where the positive end is always oriented towards the sample, it always results in an attractive interaction near O atoms, greatly reducing the complexity of interpreting these results. The lowest energy adsorption geometry prediction shown in Figure 4.4 places a Co atom above O on the NiO(001) surface, in agreement with my theoretical predictions.

In contrast to results on the NaCl surface, however, my calculations on NiO did not find a second energy minimum when Co-Salen was aligned towards the <100> directions. The shorter lattice parameter of NiO results in increased commensurability between Co-Salen and the surface. However, when the molecule is rotated towards the <100> orientations, molecular O atoms come much closer to surface anions than on NaCl, as shown in Figure 4.5.

As a result, the local minima near the <100> directions are destabilized by repulsive interactions between molecular O atoms and surface anions. This effect explained why only 8 stable energy configurations were observed on NiO(001) compared to the 16 that were previously seen on NaCl(001).

It is important to note that the periodic nature of my simulations means that Co-Salen molecules are also arranged periodically, as shown in Figure 4.6A. Although the level of coverage is similar to the experimental images presented in Section 6.2, the Co-Salen molecules within my periodic model cannot change their orientations with respect to each other in order to further reduce the energy of the system.

Finally, in addition to the differences observed on NaCl and NiO that arise to commensurability effects, I also predicted that Co-Salen molecules adsorbed onto NiO(001) are

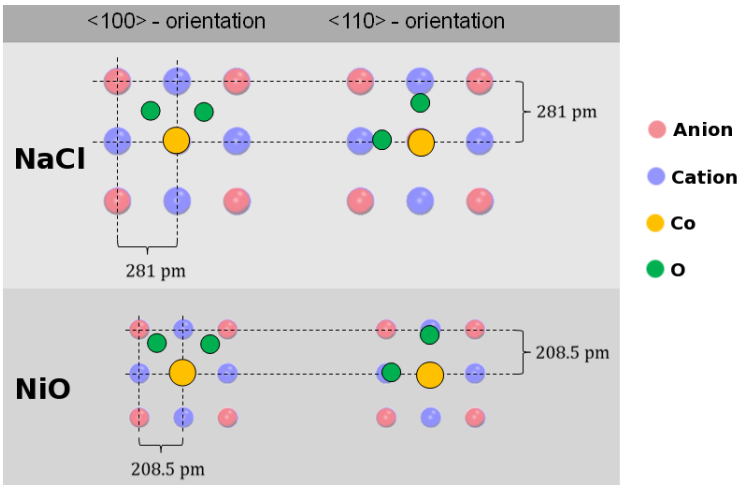

Figure 4.5: A schematic diagram illustrating the commensurability between Co-Salen molecules in the <100> and <110> orientations and the surface. The Co-Salen molecule exhibits three interactions with the NiO (100) surface. The molecular Co atom interacts with a surface O or Cl atom while molecular O atoms interact with surface Ni or Na atoms. The lattice constant on NiO is smaller than on NaCl and matches the bond lengths found in the Co-Salen molecule. As it rotates on NiO, the molecular O atoms come into close proximity to surface O atoms to destabilize the local minima found in the <100> directions.

more distorted. DFT calculations showed that the expected distance between the Co atom and the surface plane was only 2.5 Å on NiO compared to 3.0 Å on NaCl. Consequently, the more weakly bound aromatic portions of the molecule move to compensate, as shown in Figure 4.6B. These distortions can be quantified by considering the energy difference between the adsorbed geometry of a Co-Salen molecule and that of a Co-Salen molecule in the gas phase. This distortion energy is greater by 0.12 eV on NiO than on NaCl, while the deformation of the NiO surface itself was calculated to be 0.09 eV less than on NaCl. Furthermore, due to the asymmetrical C_2H_4 bridge of the Co-Salen molecule, my results predicted that the distorted molecule should also be chiral. In my simulations, the height of each aromatic ring was measured from the hydrogen atom at each end of the molecule to the surface plane and revealed a 0.5 Å difference between the two sides, as shown in Figure 4.6B. Experimental NCAFM images of Co-Salen on NiO are indeed asymmetrical, however, it is difficult to prove that this effect is related to the chirality of the single molecule itself. It is highly possible that this is at least partly due to tip-convolution.

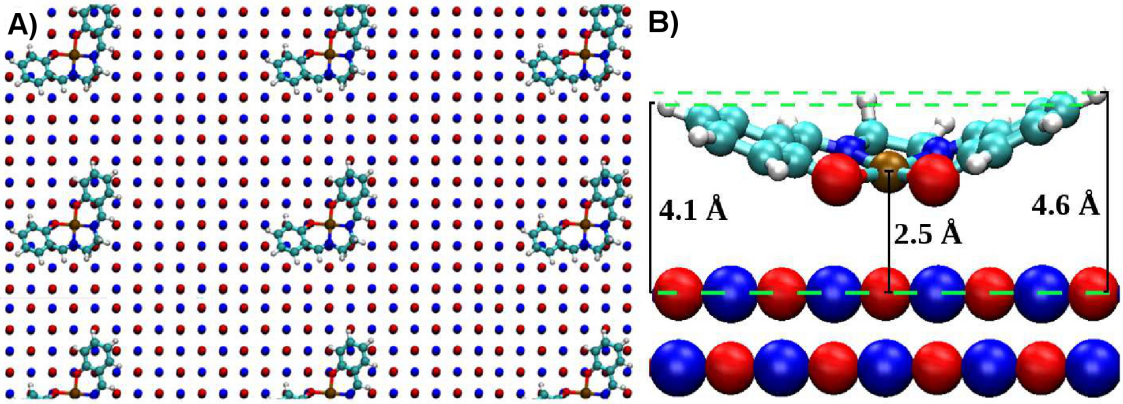

Figure 4.6: A) The theoretical system size employed results in a concentration of Co-Salen molecules on the NiO(001) surface that corresponds to roughly 1/3rd monolayer coverage. The band gap of the system and dipole formed do not change with decreased coverage, indicating an accurate representation of one Co-Salen molecule interacting with the surface. C atoms within the molecule are shown in light blue, O atoms are shown in red, N atoms in blue, and H atoms in white. On the surface, Ni atoms are shown in blue and O atoms are shown in red. B) A schematic of the Co-Salen molecule adsorbed onto NiO(001). The asymmetry of the Co-Salen molecule results in a difference in height between the two aromatic rings on either side of the structure.

Using these results I was able to propose a model that explained the experimentally observed differences in adsorption geometry between Co-Salen molecules adsorbed onto NaCl and NiO. My predictions indicate that Co-Salen interacts more strongly with the NiO surface than with the NaCl surface. However, careful characterization of the interactions between Co-Salen and NaCl and NiO was still needed to explain the mechanisms behind these observations.

4.4.3 Differences in Electronic Structure

In addition to the destabilization of minima corresponding to the <100> orientations of Co-Salen on the surface of NiO, commensurability of the Co-Salen molecule with the NiO(001) surface also enhances adsorption energy of the molecule. A closer examination of the charge density difference plot of the adsorbed system, as shown in Figure 4.7, reveals that the molecule adsorbs to NiO(001) with three strong local interaction regions. The Co atom interacts with an O atom on the surface while the two O atoms of the molecule interact with surface Ni atoms, strengthening the bond beyond the interaction predicted

for the previously studied NaCl system.

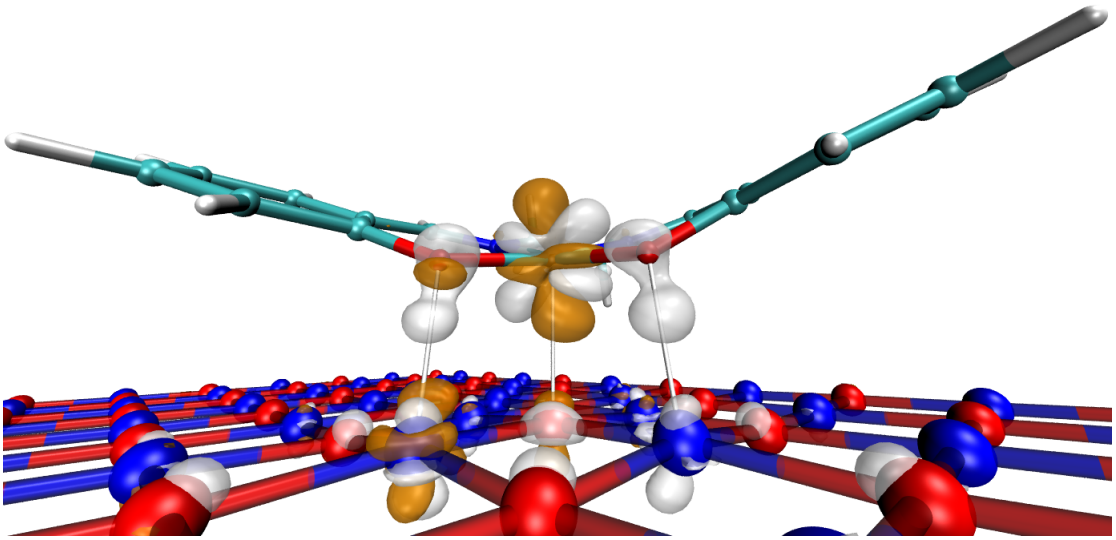

Figure 4.7: The difference in charge density induced by Co-Salen interacting with the NiO(001) surface is shown. Three regions of interaction are visible with positive isosurfaces represented in silver and negative isosurfaces represented in gold. The Co atom on the molecule interacts with O on the surface while O atoms on the molecule interact with the Ni atoms on the surface.

My calculations gave a 1.33 eV adsorption energy on NiO(001) compared to only 0.6 eV on NaCl. The BSSE in these results was predicted to be less than 0.02 eV using the counter poise correction method [15, 16] and reduced the binding energy on NiO(001) to 1.31 eV. This adsorption energy was further partitioned into a long-range dispersion component of 0.66 eV and a DFT contribution of 0.67 eV. These individual contributions to the binding energy of Co-Salen on NaCl and NiO are summarized and compared, as shown in Table 4.2.

A careful analysis of adsorption energy components reveals that while the commensurability effect does enhance the adsorption energy of Co-Salen molecules on NiO, as evidenced by an increase in the DFT contribution from 0.42 eV to 0.67 eV, it is not the only mechanism responsible for increased binding energy. The larger ionic charges present in NiO interact more strongly with the Co(II) atom and O atoms within Co-Salen to further increase adsorption energy. Finally, the lattice constant of NiO is also much smaller than that of NaCl. There are many more surface atoms within vdW interaction range

	NaCl	NiO
Adsorption Energy	0.60 eV	1.31 eV
BSSE	<0.01 eV	<0.02 eV
Dispersion Correction	0.18 eV	0.66 eV
DFT Contribution	0.42 eV	0.67 eV
Work Function Change	0.04 eV	0.40 eV

Table 4.2: The adsorption energies and change in work function of Co-Salen on the NaCl and NiO surfaces are tabulated for comparison. The results illustrate a stronger interaction with the NiO surface which is in agreement with the experimentally observed growth modes on each surface.

of the Co-Salen molecule when it is adsorbed onto NiO(001) which greatly enhances the adsorption energy, as indicated in Table 4.2.

The molecule-surface interaction was then further characterized by analyzing the work function change within the system. When a Co-Salen molecule interacts with a surface, if there is significant electronic relaxation, charge transfer may occur or a dipole moment may be formed. I used the parallel plate capacitor model [179] to characterize this effect by averaging the electrostatic potential of the system in the xy planes parallel to the surface. This revealed a 0.40 eV difference in vacuum level (or shift in work function) due to the adsorption of Co-Salen on NiO, as illustrated in Figure 4.8. A script for plotting this difference in vacuum level can be found on the included disk.

In contrast, when the same technique was applied to a Co-Salen molecule adsorbed to NaCl, the calculated difference in vacuum level was an order of magnitude smaller (0.04 eV) (see Supporting Figure C.1), indicating much less charge transfer or polarization of the system. This value for the change in the work function corresponds to a 4.4 D vertical dipole moment in the adsorbed system, which can also be partitioned into several contributions. My calculations showed that the total dipole moment of the Co-Salen on NiO(001) system was composed of a 2.4 D contribution due to distortion of the molecule, a 0.3 D contribution due to distortion of the surface, and a 1.7 D contribution due to electronic polarization or relaxation of the full adsorbed system. For comparison, I then examined a single Co-Salen molecule in the gas phase, which was found to possesses a dipole of 6.0 D aligned along the symmetry axis of the molecule with the positive end

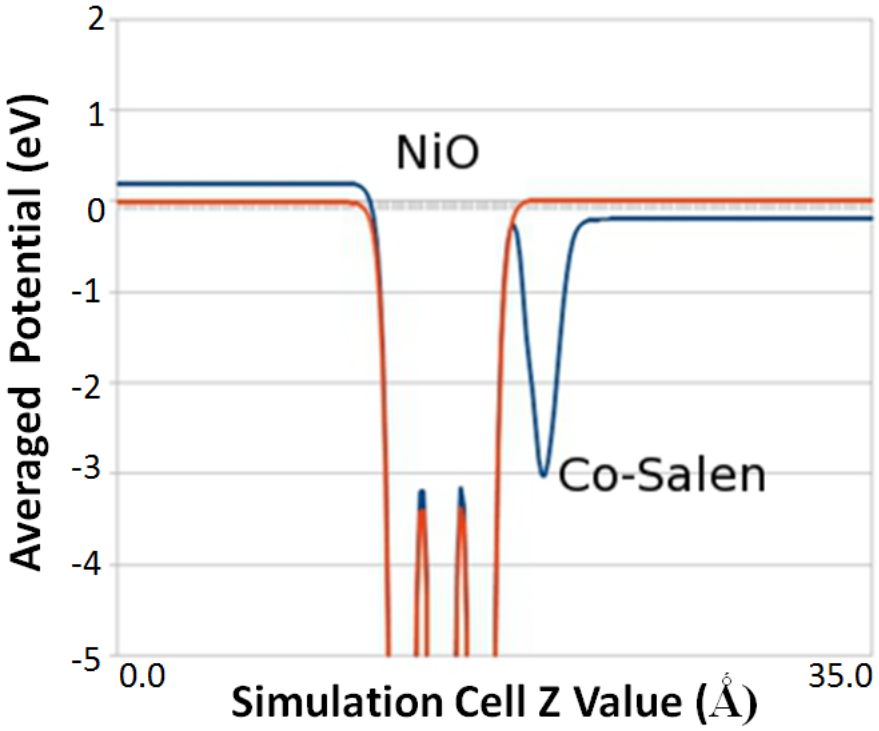

Figure 4.8: The average electrostatic potential of the system in the xy plane is plotted from one side of the simulation cell to the other. The clean NiO surface is represented in red and the Co-Salen decorated surface is represented in blue. A difference in 0.4 eV is observed when the molecule binds to the surface indicating the formation of a dipole in the vertical direction.

pointed towards N atoms, and the negative end pointed towards the O atoms. This dipole moment sits parallel to the surface plane when Co-Salen is adsorbed onto NiO or NaCl. Finally, I confirmed that these results represent the interaction between a single Co-Salen molecule and the NiO(001) surface by adjusting the size of the surface slab.

These effects can also be described in terms of electron transfer, analyzed *via* Mulliken [180] population analysis or Bader charge analysis [181]. Mulliken population analysis of the adsorbed NiO system describes the interaction as a charge transfer of 0.25 e between the Co-Salen molecule and the NiO surface. However, since Mulliken analysis is heavily dependent on the nature of the basis functions used and I employed a fairly diffuse basis set in this work, this can probably be assigned to polarization rather than actual electron transfer. This conclusion is well supported by my results using Bader charge analysis, a technique that evaluates charge density minima, which describes the interaction as a 0.02

e charge transfer.

Examining the charge density difference plot shown in Figure 4.7, it is clear the interaction can be characterized as the formation of covalent bonds rather than charge transfer. These same interactions are responsible for the increased deformation of the Co-Salen molecule that I observed in the NiO system, which further contributes to polarization. My calculations predicted that the Co-Salen molecule already possesses a 6 D dipole moment along the symmetry axis which results in local attractive interactions when they approach each other on the surface in a favorable configuration. However, when adsorbed to the NiO surface, Co-Salen exhibits an additional 4.4 D component to the dipole moment that is oriented perpendicular to the surface plane. This vertical dipole moment serves to decrease the attractive interactions between Co-Salen molecules on the surface since parallel dipoles repel. This repulsive interaction, combined with an increased adsorption energy were used to explain qualitative differences in growth between the NaCl(001) and NiO(001) surfaces which are discussed in a later section.

Finally, molecules adsorbed onto oxide surfaces have also been used to tune the band gap of insulating surfaces [155, 156, 157, 158]. My DFT calculations estimate the HOMO/LUMO gap of Co-Salen to be 3.6 eV, the band gap of the NaCl(001) surface was calculated to be 6.6 eV, and the band gap of the NiO(001) surface was calculated to be 3.6 eV. On NaCl(001), when Co-Salen binds to the surface, the HOMO/LUMO gap of the combined system is reduced to 3.6 eV, which corresponds simply to the gap of the molecule. However, on NiO(001), the highest occupied levels of the molecule lie below that of NiO, producing a 3.3 eV band gap for the Co-Salen on NiO(001) system. These results show that careful selection of the molecule and substrate and an understanding of the electronic structure of the system is important in understanding the mechanisms and interactions between organic molecules (or metal-organic complexes) and insulating surfaces.

4.4.4 Diffusion Barriers and Manipulation

In addition to adsoption geometries, NCAFM images can sometimes also provide information on the diffusion barriers for small molecules on the surface. To provide a comparison, I calculated the barriers for the rotation and diffusion of small CO molecules on the NaCl(001) and NiO(001) surfaces. One important difference between the geometries observed in these systems was that the <100> direction orientation on NiO is destabilized. As previously described, on NaCl(001) the lattice constant is such that when the Co-Salen molecule is rotated in the <100> direction, the O atoms are not positioned close enough to be repelled by surface anions. On the NiO surface, however, this repulsive interaction destabilizes the local minimum in the <100> direction resulting in half the number of total observed adsorption geometries. Since this work focuses on NiO, I compared the diffusion barriers for Co-Salen molecules oriented in the <110> configuration. On NiO, my calculations predict a 0.6 eV barrier for the minimum energy pathway that corresponds to a simple translation of the molecule along the <110> direction. In comparison, I calculated the barrier for rotation of the Co-Salen molecule around the Co atom on NiO(001) to be 0.8 eV, indicating that translation is more likely to occur than rotation. These results are in good qualitative agreement with experimentally observed tip-induced motions, as shown in Figure 4.9.

The combined theoretical predictions and experimental data for Co-Salen on NiO(001) demonstrate that the Co-Salen molecule moves in a straight line along the <110> direction when manipulated. Furthermore, my calculations estimate the barrier for a similar diffusion process of Co-Salen on NaCl to be 0.4 eV. These results are consistent with experimental observations that Co-Salen is more easily manipulated on NaCl(001) than on NiO(001).

Finally, the experimental image in Figure 4.9 is a good example of a process that occurs during the course of collecting one NCAFM image. Since the molecule moves in the <110> direction as it interacts with the metallic tip, it appears as a long ridge feature in the image.

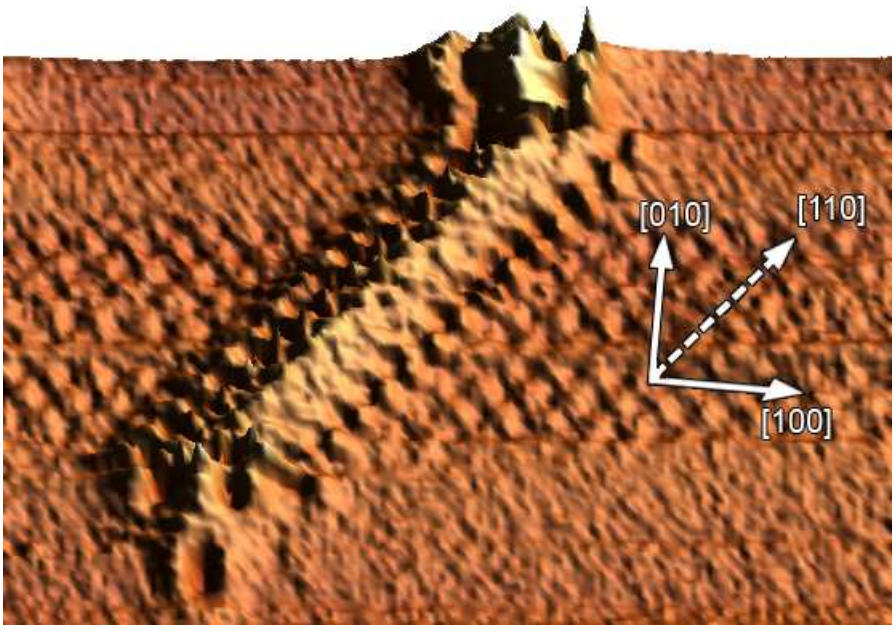

Figure 4.9: $(7.2 \times 5.2)\,\mathrm{nm}^2$ NCAFM image depicting the tip-induced motion of the Co-Salen molecule on NiO(001). While the tip scans upwards in the [010] direction, the molecule is observed to move along the [110] direction corresponding to the minimum energy pathway for diffusion. Parameters: Deposition at 30 K and imaging at 8 K with Δf = -11.81 Hz, $c_z = 155.3\,\mathrm{N/m}$, $A = 6.47\,\mathrm{nm}$, $f_0 = 193$,kHz, $Q = 143563$

4.4.5 Differences in Growth

All of the properties discussed so far combine to influence the morphology and growth modes of Co-Salen films grown when higher coverages of molecules are deposited on NaCl and NiO. Another experimentally observed phenomenon that could not be explained without theoretical results is the difference in growth modes observed on NaCl(001) and NiO(001). When Co-Salen molecules are deposited at low coverage onto NaCl(001) at room temperature, the molecules are seen to aggregate at step edges, as shown in Figure 4.10A. As more Co-Salen molecules are deposited nanostructures begin to form on the surface, as shown in Figure 4.10B.

This type of growth is commonly described as island growth. However, when the same molecules are deposited onto the NiO(001) surface layer-by-layer growth is observed instead. Co-Salen molecules deposited at low coverage onto NiO(001) initially aggregate at step edges as previously observed on NaCl(001), as shown in Figure 4.11A. At increased

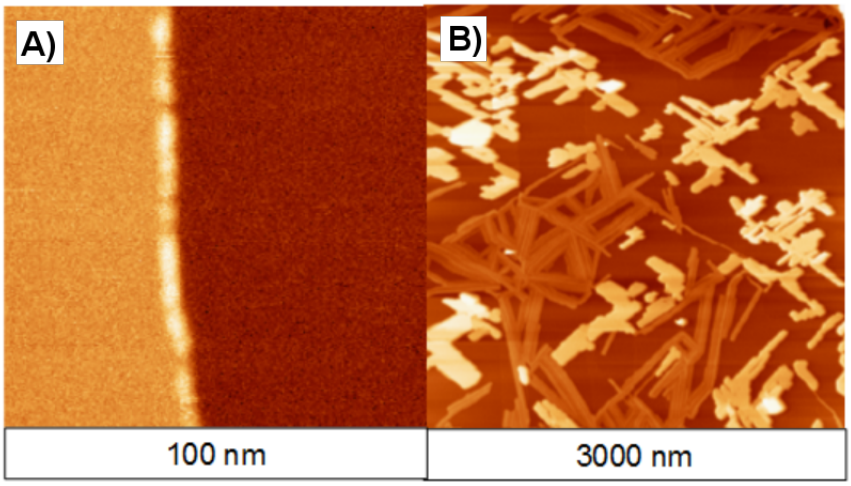

Figure 4.10: A) An NCAFM image of a step edge on the NaCl(001) surface after deposition of approximately 0.2 monolayers of Co-Salen molecules. The terraces are clean while molecules appear to aggregate at the step edge. B) An experimental image of the nanostructures formed on NaCl(001) after the deposition of several monolayers of Co-Salen molecules.

coverage nanostructures are noticeably absent and disordered layer structures are observed instead, as shown in Figure 4.11B.

These differences can be explained using the DFT results previously presented in this chapter. On NaCl(001), the molecule-surface interaction is relatively weak (0.6 eV adsorption energy) while on NiO(001) this interaction is much stronger (1.3 eV adsorption energy). Furthermore, Co-Salen molecules repel each other on NiO(001) due to the vertical dipole moment generated during adsorption. The combination of these properties means that Co-Salen molecules are much more likely to aggregate and interact with each other on NaCl(001) than on NiO(001), resulting in the observed nanostructures. These results indicate that the fine balance between competing interactions within a system can qualitatively change the morphology and structure of deposited films.

4.5 Discussion and Conclusions

In this chapter I studied the adsorption of Co-Salen molecules on NiO(001) by combining NCAFM data taken using a Cr coated tip and DFT. The use of a metallic tip enabled

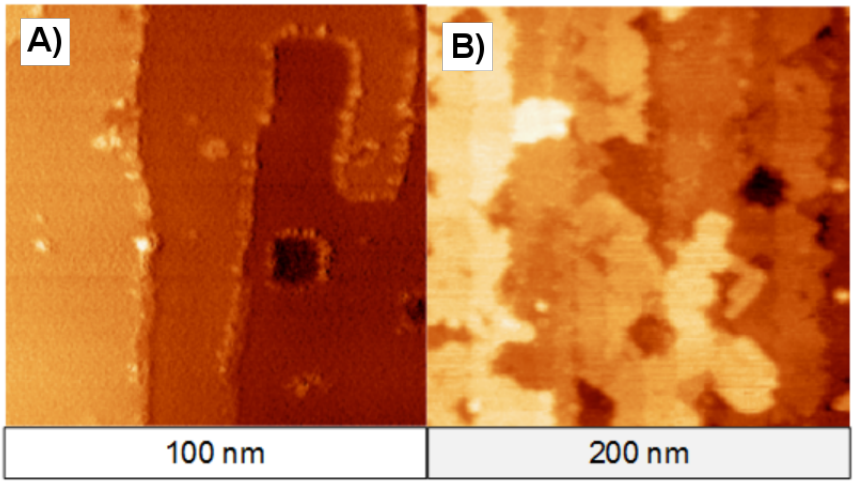

Figure 4.11: A) An NCAFM image of a step edge on the NiO(001) surface after deposition of approximately 0.2 monolayers of Co-Salen molecules. The terraces are clean while molecules appear to aggregate at the step edge. B) An experimental image of the layer structures formed on NiO(001) after the deposition of several monolayers of Co-Salen molecules. These structures are much less ordered than the ones observed on NaCl(001) and grow layer-by-layer.

simultaneous resolution of both the molecule and the substrate. DFT calculations predicted that Co-Salen adsorbs with the Co atom directly above a surface O, allowing me to confirm that the bright spots do indeed correspond to surface anions.

The theoretical results I presented on the adsorption geometry and the distribution of orientations of Co-Salen on NiO(001) was compared to previous data on NaCl(001). Despite the fact that both surfaces are bulk insulators with a simple cubic crystal structure, several qualitative differences in the adsorption, mobility, and growth of Co-Salen molecules were observed. In particular, the shorter lattice distance of NiO resulted in improved commensurability with the Co-Salen molecule. This increased the adsorption energy while simultaneously destabilizing the previously low energy configurations corresponding to orientations where Co-salen was aligned in the <110> directions. These results successfully explained why Co-Salen molecules were observed in 16 orientations on NaCl but only 8 on NiO. Furthermore, my calculations predicted that Co-Salen binds more strongly to NiO than to NaCl due to several major factors. The first two are reflected in the DFT contribution to adsorption energy. The increased ionic charges present in NiO result in stronger

interactions with the Co(II) and O atoms of the Co-Salen molecule. Additionally, since the molecule-surface commensurability is higher on NiO, the molecule is able to interact with the surface in attractive regions through the formation of covalent metal-oxygen bonds. These interactions were clearly visible in the charge density difference plot of Co-Salen adsorbed onto NiO(001) and results in a 4.4 D vertical dipole moment. The third important contribution is the result of increased vdW interactions with a closely packed NiO substrate. These interactions helped explain the differences in growth observed on NiO and NaCl. A strong molecule-surface interaction coupled to a weak molecule-molecule interaction on NiO results in layer by layer growth, while a weaker molecule-surface interaction and stronger molecule-molecule interactions results in island growth on NaCl.

The experimentally observed tip-induced translation of the Co-Salen molecule was then shown to be in good agreement with my DFT calculations of minimum energy pathways on the surface. Furthermore, these translations are closely related to the minimum energy configurations of the molecule on the surface. Co-Salen was observed to move in the <110> direction on NiO(001), which corresponds to the lowest energy pathway for diffusion and the symmetry axis of the molecule in the minimum energy configuration. It is suggested that symmetry may play a large role in systems where the molecule-substrate interactions are relatively weak [182]. Finally, the relative ease of inducing tip-induced displacements on NaCl(001) was in line with my predictions that the diffusion barrier is lower than on NiO(001).

The results of this study provided some insight into the balance of molecule-molecule and molecule-surface interactions that determined the mode of growth that was observed when depositing Co-Salen molecules on NaCl(001) and NiO(001). On NaCl, the molecule was well described by its gas phase behavior. My calculations showed that there is a dipole of 6 D orientated along the symmetry axis of the molecule which sits parallel to the surface plane. On NaCl, the out of plane contribution to this dipole moment is negligible (<0.1 D). The interactions between these molecular dipoles pull the molecules together into rows, and at nucleation sites the weak molecule-surface interaction allows dimerization and

island growth to occur [183]. However, on NiO the molecule has a much larger adsorption energy and is much more distorted. These effects when combined with electronic relaxation resulted in a total out-of-plane dipole of 4.4 D in my calculations. On NiO(001), this interaction is of comparable magnitude to the in-plane dipole and is repulsive between molecules. While Co-Salen molecules should still adsorb parallel to each other on the surface due to the remaining in-plane dipole, the attractive interaction that pulls them together into rows is absent. Furthermore, a much stronger molecule-surface interaction hinders dimerization since the molecules prefer to remain flat on the surface. Finally, I calculated diffusion barriers that suggest that the aggregation of Co-Salen molecules is kinetically limited. At the low temperatures and moderate coverage of these experimental images, the majority of deposited Co-Salen molecules are isolated. This can be partly attributed to the lack of strong molecule-molecule interactions. However, in many previous studies of the deposition of atoms or small molecules, the deposited atoms (or molecules) were able to migrate to step edges at low temperatures where thermal diffusion should be suppressed. This effect has been termed transient mobility and is often included in rate calculations and kinetic Monte Carlo simulations [66, 67, 68, 69, 70] in order to achieve good agreement with experiment.

In summary, the Co-Salen molecule and the NiO(001) surface ions were simultaneously resolved using a Cr tip with NCAFM. My results show that combining DFT with NCAFM experiments can provide rich information on the adsorption energy, adsorption geometry, and diffusion of individual molecules at insulating surfaces that is unavailable to other surface science techniques. Importantly, these studies highlight the role that commensurability between the molecule and the surface can play in determining the strength of the interactions present in the system. The relative strength and weakness of molecule-molecule or molecule-surface interactions can qualitatively change the growth processes on insulating surfaces. These are important effects that I will focus on in later chapters of this thesis. Finally, while DFT calculations helped greatly in the interpretation of the NCAFM data presented in this chapter, it is clear that the imaging mechanism and the character

of the metallic tip is not well understood. These tips appear to be able to achieve atomic resolution on the NaCl and NiO surfaces, however, they could not resolve individual atoms within the Co-Salen molecules.

Chapter 5

Atomic Force Microscopy with Metallic Tips

Aims: The next important step of my studies on molecules on bulk insulators was to ensure that any comparisons made between my predictions and experimental NCAFM results are accurate and unambiguous. This chapter describes the point dipole model that I used to represent metallic tips. Interpretation of experimental AFM data is often difficult and requires detailed knowledge of the structure of the tip. Metallic tips, however, can be approximated as a point dipole at large tip-sample distances, greatly reducing the complexity of interpreting and simulating images. I give an introduction in section 5.1, a brief description of the experimetal methods used by A. Schwarz and J. Grenz to collect the NCAFM data used in this chapter in 5.2, and present the theoretical methods I used in section 5.3. I then present the results of my *ab initio* studies of metallic tip asperities in section 5.4.1 and describe the point dipole model that I used to represent Cr coated NCAFM tips in section 5.4.2. Finally, I use experimental data of CO molecules on NiO(001) to test the point dipole model in section 5.4.3 and strengthen the argument that metallic tips appear atomically sharp by using a CO molecule on the surface to image a Cr coated tip in section 5.4.5. Imaging mechanisms and the origin of contrast are covered in section 5.4.6. I conclude with a discussion of the more general applicability and implications

of these methods in section 5.5.

Methods: I have written a computer code to convert the Hartree potential file from DFT calculations performed using the CP2K code into a 3-dimensional force field file. This force field is used as one part of my model for the metallic tip which is then used in conjunction with a VAFM code [184] to simulate images that can be directly compared with experimental data. In these simulations the interactions between a metallic tip and the sample are represented as a sum of the macroscopic vdW interactions, the local vdW interactions, and electrostatic interactions.

Results: The metallic tip‘s macroscopic parameters, structure of the microtip, and the magnitude of the dipole moment are directly fit to experimental data. Using these parameters, VAFM scan-lines over single CO molecules on NiO(100) were simulated and compared directly to experimental data. The results show that this method can achieve quantitative agreement while greatly reducing the complexity of modeling the AFM tip.

5.1 Introduction and Prior Work

Since the overall philosophy that I have outlined involves a direct comparison between theoretical predictions and experimental observations, the accurate interpretation of experimental data is critically important. While DFT results can be compared to NCAFM images to interpret data, as demonstrated in the previous chapter, a true understanding of the imaging mechanisms can only be achieved with an accurate representation of both the tip and the sample. It is widely acknowledged that knowing the exact structure of the NCAFM tip apex is vital for understanding and interpreting high-resolution NCAFM images [185, 186]. It is logical then that using well characterized, atomically sharp, stable tips is critical when imaging molecules at surfaces with atomic resolution and for accurate analysis of the experimental data. However, such tips are difficult to prepare and this often becomes a matter of trial and error.

The solution to this problem depends on the development of characterization techniques and methods of controlling the atomic structure of the tip. One successful strategy that has been used in the past is to characterize tips using field ion microscopy (FIM) [187]. However, it is not practical to analyze every tip before and after they are used for measurements. Instead, the need to characterize the tip can be somewhat alleviated by functionalizing it using a small molecule, such as CO [188], or a Xe atom [189]. The imaging strategy when using functionalized tips is typically based on measuring short-range repulsion forces [190], which has both advantages (intramolecular resolution) and disadvantages (image distortion or manipulation of the adsorbed molecules). Unfortunately, such controlled functionalization of the AFM tip is difficult to achieve in some systems.

Microfabricated Si cantilevers with integrated pyramidal Si tips are the most commonly used tips in NCAFM experiments. These Si or oxidized Si tip apices can exhibit a wide range of possible tip structures due to the presence of directional covalent bonds. Since NCAFM images always represent a convolution of the tip and the sample, a wide array of possible tip models must be tested in order to find reasonable agreement between simulation and experiment [191]. Metallic tip apices, on the other hand, are often atomically

sharp and stable, which allows for atomic resolution. These tips can be expected to have a pyramid-like termination [192]. As discussed in the previous chapter, experiments using Cr coated Si tips have been able to achieve good atomic and chemical resolution when imaging binary ionic surfaces at rather large (>0.5 nm) tip-sample separations [193, 174, 3]. Additionally, such tips can be routinely prepared *via* thermal evaporation *in-situ* [193] and the conductivity of the coated tip can be checked to ensure that it is metallic [174]. This method of tip characterization confirms that the metal coated tip is free of adsorbed small molecules and other contaminants. Cr coated tips were used to unambigiously determine the adsorption site and geometry of single Co-Salen molecules on NaCl(001) [3] and NiO(001) [175] surfaces with atomic accuracy. One major advantage of this technique is that these metallic tips can be used to atomically resolve flat surfaces at large tip-sample separations and minimize risk of contamination by the surface. In these studies, the chemical resolution achieved was attributed to the existence of a dipole moment at the metallic tip apex, however, the magnitude and origin of this dipole was not well understood.

The primary mechanism responsible for image contrast in these NCAFM experiments using metallic tips has previously been attributed to the Smoluchowski effect [194]. This states that step features on metal surfaces possess dipole moments due to an incomplete screening of the positive ion cores by conduction electrons. This mechanism is consistent with experimental data on the influence of step edge density on the work function of Au(111) [195], Cu(111) [195], Pt(111) [196], and W(110) [196]. In these studies, the presence of a dipole moment with a 0.1-0.2 D magnitude was confirmed. Theoretical studies then predicted that the dipole moment is proportional to step height and screening length [197]. However, the magnitude of these dipole moments are too small to explain the experimentally observed image contrast in NCAFM experiments. In order to have significantly larger dipole moments at the tip apex, sharper pyramidal features containing lower coordinated atoms must be present [174]. The existence of such tip features can be inferred from various experiments but their existence cannot be proven by directly imaging the tip.

In this chapter I introduce a procedure for characterizing metal-coated tips and generating virtual AFM (VAFM) images of molecules on bulk insulating surfaces. I demonstrate that the effective dipole moment of the tip can be determined using atomic resolution images of the surface. Chemical resolution of surface ions and images of small adsorbed molecules can then be well described by using a point dipole model to represent the tip. With this model, the most important tip feature is the magnitude of the dipole moment which can be extrapolated from experimental data. The exact structure at the metallic tip apex is less important when experiments are performed at large tip-sample separations. I demonstrate that this model is able to produce scan-lines that are in quantitative agreement with experimental data of adsorbed CO molecules on NiO(001).

5.2 Experimental Methods

The tip parameters that I used with the point dipole model were fit directly to experimental NCAFM data and experimental images and scan-lines of CO molecules on NiO(100) were used to compare and validate the model. These measurements were performed by J. Grenz and A. Schwarz at the University of Hamburg. The experimental methods are briefly described below and are reproduced from a joint publication in ACS Nano [198] where more detailed information can be found.

All measurements were performed at about 8 K with a home-built low-temperature ultra-high vacuum (UHV) force microscope [199]. The substrate, NiO, crystallizes in the rock salt structure with a lattice constant of 4.17 Å. Clean (001) surfaces were prepared by *in-situ* cleavage of single crystals at a pressure of about 1 x 10^{-10} hPa and subsequent annealing at about 500° C to remove residual charges. After cooling down the substrate in the cryostat, CO molecules were admitted *via* a leak valve and Co-Salen molecules were evaporated from a crucible. At these low temperatures both species are immobile, leading to a random distribution of well separated individual molecules on the surface, as previously shown in Figure 4.3.

High resolution AFM measurements were performed in the noncontact mode (NCAFM) using the frequency modulation technique (FMAFM) [172]. In this mode of operation the cantilever self-oscillates with constant amplitude A_0 at its resonance frequency f_0. Forces between the tip and sample shift the actual cantilever frequency f by $\Delta f = f - f_0$. To image in the noncontact regime, where attractive forces dominate, a suitable negative Δf was chosen as a set-point for the z-regulator. Scanning the tip line by line across the (x, y) sample surface while Δf is kept constant provides a $z(x, y)$ map of constant tip-sample interaction, *i.e.*, the topography.

To prepare a tip with an electric dipole moment at its apex, supersharp Si cantilevers (2 nm nominal tip radius) [173] were coated *in-situ* with a few nanometers of Cr. The contact potential difference (CPD) between the tip and sample was determined by recording $\Delta f(U_{\text{bias}})$-curves. $U_{bias} = U_{CPD}$ was applied between tip and sample to minimize long-range electrostatic interactions. As previously described [174], these curves were also used to characterize the metal coated tips.

5.3 Theoretical Methods

I studied the NiO(001), Cr(110), and Cr(001) surfaces using the mixed Gaussian and plane waves approach [13, 200] as implemented within the CP2K code. The calculations discussed in this chapter include geometry minimizations and molecular dynamics of the bare surfaces and surfaces with adsorbed CO molecules.

NiO(001) with adsorbed CO molecules was treated using many of the techniques described in Chapter 2. The B3LYP [7, 8] hybrid functional was used to properly describe the electronic structure of the NiO surface. I was able to produce a NiO band gap of 3.6 eV compared to an experimentally measured value of 4.3 eV [177] and obtained negligible surface rumpling which is consistent with experimental results [178]. Additionally, previous calculations suggest that the B3LYP functional can produce reasonable bond lengths for the CO molecule adsorbed onto NiO, however, the results suffered from a very large

basis set superposition error (BSSE). To solve this problem, I used basis sets designed to minimize superposition error in molecular systems (MOLOPT) [19] and calculated the adsorption energy of CO on NiO(001) to be 0.3 eV in agreement with prior studies [201, 202]. These basis sets were derived to be used with pseudopotentials proposed by Goedecker, Teter, and Hutter (GTH) [18]. These pseudopotentials describe the core electrons so that only the valence electrons (1 H, 4 C, 5 N, 6 O, 17 Co, and 18 Ni valence electrons) must be included explicitly in the calculation. This reduces the number of electrons, basis functions, and primitive Gaussians per atom. Furthermore, this method predicts that the CO molecule adsorbs upright in a slightly tilted configuration in agreement with prior calculations [201]. My results indicated a total tilt of 6°. The expense of simultaneously using a hybrid functional and extensive basis sets was mitigated with the ADMM [17] as previously described. The auxiliary basis sets for Ni and Co were obtained by averaging the parameters optimized using small fitting environments as described in Chapter 2. For all other elements in the system, auxiliary basis sets were taken directly from the standard CP2K distribution (pFIT3) [17]. The results demonstrate that this basis set and functional produce accurate surface properties and can reasonably represent the adsorbed system, while reducing the BSSE to less than 0.1 eV.

The NiO(001) surface was represented using a 3 atomic layer slab consisting of 288 atoms in total. The size of this slab was selected by increasing the size of the cell until adsorption energy converged in order to avoid interactions between molecules in the 2D periodic simulation. I similarly selected a plane wave cutoff of 400 Ry by increasing it until adsorption energy converged. Finally, I employed the semi-empirical dispersion correction method [176] described in Chapter 2. In this work the O atoms were assigned default values and Ni atoms in the surface were approximated as Ar.

I constructed Cr surfaces and tip asperities based on information from prior experimental studies. Field ion microscopy (FIM) experiments [187] performed on W NCAFM tips show that these metal coated tips are spherical and possess (110) terraces at the tip apex. However, the nature of FIM experiments means that any asperities present were

removed *in situ* using field evaporation by raising the tip voltage. In order to characterize the asperities that may be present on a NCAFM tip, I explored other experimental studies. Scanning electron micrographs (SEM) of sputtered Cr films on SiO_2 [203] confirm that deposited Cr films should be rough and exhibit a variety of asperities. Indeed prior studies confirm that not only are the deposited films quite rough, but that the morphology of these asperities depends on the method of deposition and the thickness of the deposited film [203, 204, 205]. Furthermore, these asperities can reasonably be expected to be pyramidal [192]. Using these results as guidelines I approximated Cr coated tips as macroscopic spheres terminated by (110) terraces. The tip apex was then modeled as a pyramidal asperity on the Cr(110) surface. I constructed a series of representative nano-tips out of pyramidal asperities on the Cr(110) surface, as shown in Figure 5.1. A second series of asperities were constructed on the Cr(001) surface in the same way. Both sets of Cr tip asperities were treated using a standard PBE GGA [5, 6] functional. The plane wave cutoff was selected to be 350 Ry and the MOLOPT [19] basis set was used for consistency. In these simulations, hybrid functionals were not needed as these parameters were able to produce work functions that were in good agreement with prior calculations. My results gave a 4.8 eV work function for the (110) surface and a 4.0 eV work function for the (001) surface in agreement with prior studies [174, 206]. Examples files for calculating Cr tip asperities and CO molecules on NiO using the CP2K code can be found on the supplementary disk attached to this thesis.

One of the major objectives in this chapter is to characterize the dipole moment of metal coated tips used in NCAFM experiments. While DFT can provide much information about the electronic structure of the system, explicit determination of the magnitude of the dipole moment is not straight forward and must be considered using some approximation. One way of calculating the dipole moment of these asperities is by examining the electrostatic potential averaged across the xy-plane in the 2-dimensional periodic cell. The presence of an asperity should shift the vacuum level on either side of the slab and change the work function if a dipole moment is present. This effect can be considered using the parallel

plate capacitor model [179]. The work function change is related to the magnitude of the dipole moment and the surface area as follows:

$$\Delta W = \frac{eD}{\epsilon_0 A}, \tag{5.1}$$

where D is the dipole moment due to the presence of an asperity, A is the area of the system, ϵ_0 is the electric permittivity of vacuum, and e is the unit of elementary charge. I used this method to estimate the dipole moment produced by model Cr asperities as well as the dipole moment produced by the CO molecule in the gas phase and adsorbed onto NiO(001). A script for calculating this work function change is provided on the supplementary disk attached to this thesis.

5.4 Results

5.4.1 Metallic Tip Characterization

The closest thing to experimental characterization of metallic STM and NCAFM tips is imaging them with FIM. In such experiments, tips are fabricated from polycrystalline and single-crystalline W(111) wires *via* DC electrochemical etching and used to image various surfaces [187]. These tips are studied using FIM both before and after they have been used for imaging and the results show that these tips possess atomic steps at the otherwise smooth surface. These step features can be expected to exhibit small dipole moments due to the Smoluchowski effect. However, these dipoles are expected to be within the range of 0.1-0.2 D and are an order of magnitude smaller than those predicted for Cr coated AFM tips [174].

The NCAFM tips employed to collect the experimental data used in this work were Si cantilevers coated with Cr. These Si cantilevers were coated with approximately 4 nm of Cr to produce a conducting path between the cantilever stage and tip apex. Cr was chosen because it adheres well to Si oxide. Indeed it has previously been used to facilitate

the deposition of other metals [203, 204, 205] on oxidized Si surfaces. Previous theoretical studies performed by Teobaldi *et al.* used a pyramidal Cr tip model [174] to predict that Cr coated tips should possess a dipole moment with the positive end oriented away from the surface. It was previously inferred that the dipole moment should always be oriented in this way due to the Smoluchowski effect. The Smoluchowski effect describes how a rough morphology leads to a reduction of the work function when considering the smooth contour of the electron density. Electrons cannot perfectly screen sharp structures on a surface, such as a step edge, due to finite screening length. Sharp features therefore, are expected to have dipole moment with the positive end pointing away from the surface. However, this may not always be the case. Here I illustrate how the dipole moment of the tip depends on the exact structure at the tip apex and the surface and show that my proposed tip model is consistent with experimental data.

I imagined the Cr coated tip as a macroscopic sphere terminated by Cr(110) terraces and constructed a series of representative nano-tips out of pyramidal asperities on Cr(110), as shown in Figure 5.1. The pyramid structure was chosen according to classic Wulff construction [207] in order to minimize the total surface energy. These pyramids were placed onto periodic slabs of Cr(110) since using Cr clusters rather than surfaces may lead to incorrect predictions. I then calculated the total dipole moment within each system shown in Figure 5.1 by evaluating the change in work function using the method described in Section 5.3.

The dependence of the magnitude of the tip dipole moment on the number of atomic layers in the pyramidal tip asperity is shown in Figure 5.2. These values are comparable with the previous results [174] that predict a 1.2 D dipole moment for a single adatom and a 6 D dipole moment for a three atom high pyramidal tip asperity. Previous experimental measurements on the Au and Cu surfaces [195] determined the dipole moment to be 0.16 D/step atom on Au and 0.5 D/step atom on Cu surfaces [195]. These experimentally measured dipoles are significantly smaller, however, they are attributed to step edge atoms that are better coordinated than single adatoms or atoms near the tip of a pyramidal

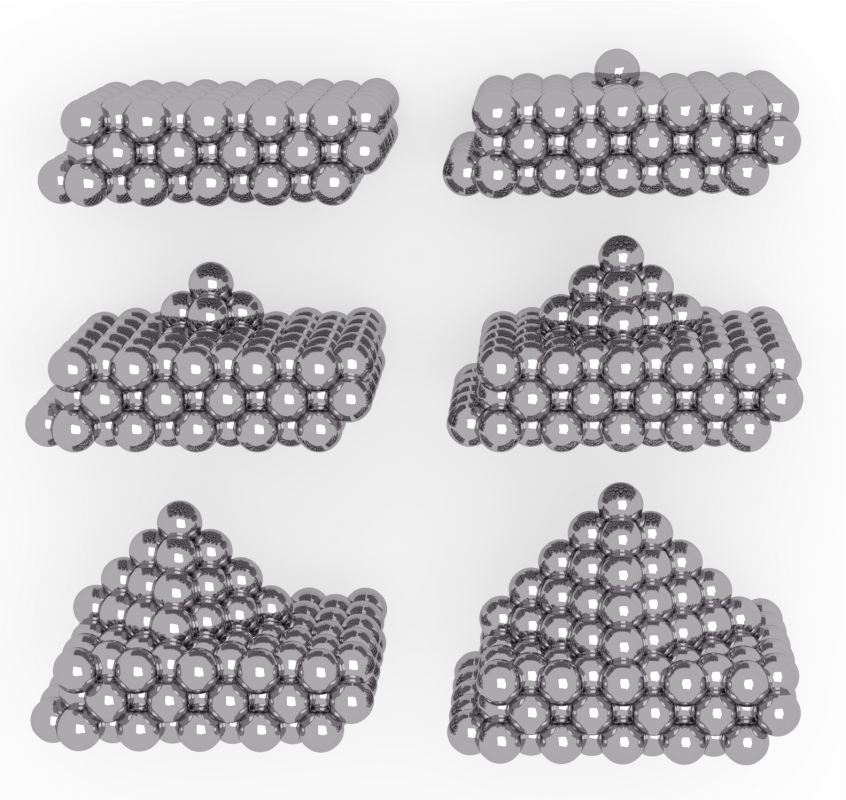

Figure 5.1: An array of pyramid features ranging from 0 to 5 atomic layers in height constructed on the Cr(110) surface. These pyramid features represent some possible stable atomic structures found on a vapor deposited Cr tip or surface.

asperity. Indeed it was previously predicted that the Smoluchowski effect should increase with increasing step height and decreasing coordination [197]. Therefore, larger pyramidal asperities that contain lower coordinated atoms would be expected to exhibit larger dipole moments in comparison to step edges on a metal surface.

While the results shown in Figure 5.2 confirm that larger pyramidal asperities do produce larger dipole moments, the magnitude of the dipole moment does not appear to scale linearly with pyramid height. In contrast, previous studies predicted that the Smoluchowski effect is expected to scale linearly with increasing step height [197], indicating that it may not be the only mechanism responsible for these dipole moments. Another mechanism that can contribute to the dipole moment is charge transfer between Cr facets that have differing work functions. My calculations give the work function of Cr (110) as 4.8 eV and the work function of Cr(100) as 4.0 eV. Within these systems it is reasonable that electron

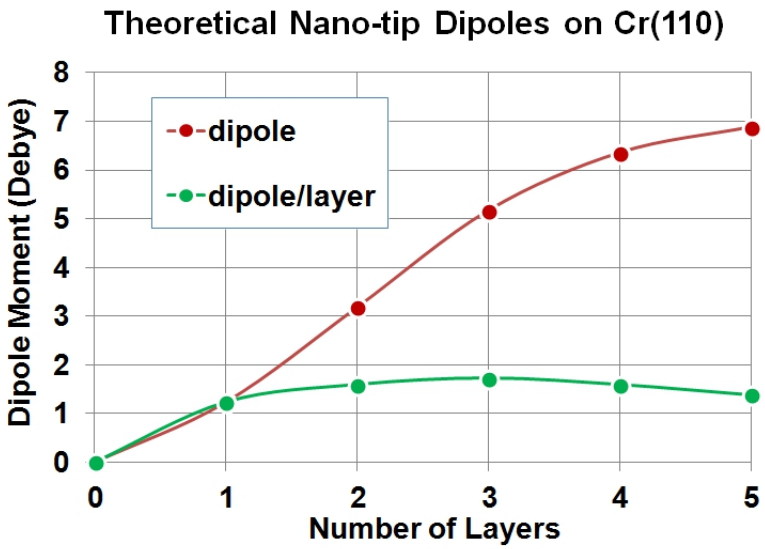

Figure 5.2: The total dipole moment of various pyramidal nano-tips as a function of pyramid height. These tips were constructed as pyramidal asperities on the Cr(110) surface. The dipole moment found at the tip apex of these asperities increases with pyramid size but should eventually converge to a maximum value.

transfer would occur from the exposed Cr(100) facets to the Cr(110) surface. This effect would increase as the size of the pyramids increase and more Cr(100) is exposed. As this happens, the work function near the pyramidal asperities decreases until it converges to the value of the Cr(100) surface. Eventually this should cause the total dipole moment at the tip to converge as well. This charge transfer effect combined with the Smoluchowski effect would produce much larger dipole moments that are consistent with the magnitudes needed to explain NCAFM experimental contrast. However, these results indicate that the dipole moment may not always be oriented in the same way as previously inferred. Depending on the surface morphology or material used, it may be greatly reduced or point in the opposite direction.

To illustrate this point, I considered the opposite example where pyramidal asperities are placed on the less stable Cr(100) surface. Since the work function of the surface is now only 4.0 eV, I expected the surface to transfer charge from the Cr(100) surface to the exposed facets instead. Using the same methods as before, the dipole moment of several pyramidal asperities on the Cr(100) surface were calculated and are shown in Figure 5.3.

These results confirm that pyramidal asperities on less stable surfaces may have reversed dipole moments due a reversal in charge transfer. Furthermore, the magnitude of the dipole moments produced in these two examples differ on average by 1 D. This is consistent with the fact that the Smoluchowski effect does not depend on the work function of the surface or exposed facets and would always contribute to the total dipole moment in the same way. On Cr(110) the orientation of the dipole moment due to charge transfer matches the contribution from the Smoluchowski effect and the two mechanisms work together in a constructive way. However, on the less stable Cr(100) surface, these two contributions oppose each other and result in a lower value for the total dipole moment. It is important to note that it is difficult to define the work function of a small facet and these comparisons are only qualitative. At the genuine nanoscale the distinction between these two effects blurs and all that can be considered is the net effect of electron density redistribution around the nano-tip.

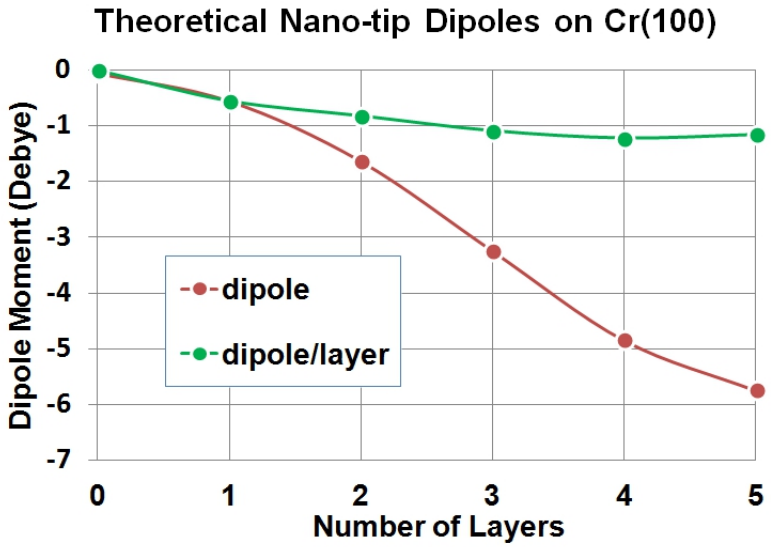

Figure 5.3: The total dipole moment of a series of pyramidal nano-tips on Cr(100) as a function of pyramid height. The work function of the Cr(100) surface is much lower than that of the Cr(110) surface, resulting in charge transfer from the surface to the asperity apex instead.

In the following sections I assume that the experimentally produced tips are terminated by stable surfaces. These would correspond to Cr(110) surfaces with pyramidal asperities.

These asperities would exhibit dipole moments with the positive pole pointed away from the tip, or towards the sample. I will then show that this dipole moment can be used to image the surface and that the imaging mechanism can be approximated using a point dipole model.

5.4.2 The Point Dipole Model

Theoretically I have shown that Cr coated tips used in NCAFM experiments can reasonably be expected to have significant dipole moments on the order of 1-10 D. However, these results are only qualitative and must be explored in conjunction with experimental data. To further quantify this model I used a point dipole to approximate the total dipole found at the metallic tip apex and constructed a complete model of the tip that can be used with virtual AFM (VAFM) codes. I then compared my results from VAFM simulations with experimental data obtained by imaging the NiO(001) surface with Cr coated tips. With this model, I demonstrated that it is possible to extrapolate the magnitude and orientation of the tip dipole directly from experimental data.

In NCAFM, the total force between the tip and the sample can be partitioned into several components. These contributions include the long-range vdW interactions between the macro-tip and the surface, mid-range electrostatic interactions between localized dipoles in the tip and sample, and local vdW interactions between the nano-tip and the surface, as shown in Figure 5.4. Short-range repulsive interactions, *i.e.* Pauli repulsion, can be ignored as long as experiments are performed at large tip-sample separations. In these experimental data sets, the average contact potential difference was compensated by applying an appropriate bias voltage between the tip and the sample, eliminating the need to account for long-range electrostatic interactions [174].

The contributions to total force were considered independently and later combined into a complete model of the tip. The first component that I examined was the long-range macroscopic vdW interactions between the macro-tip and the surface. At very large tip-sample separations, only these interactions are present, making it possible to collect

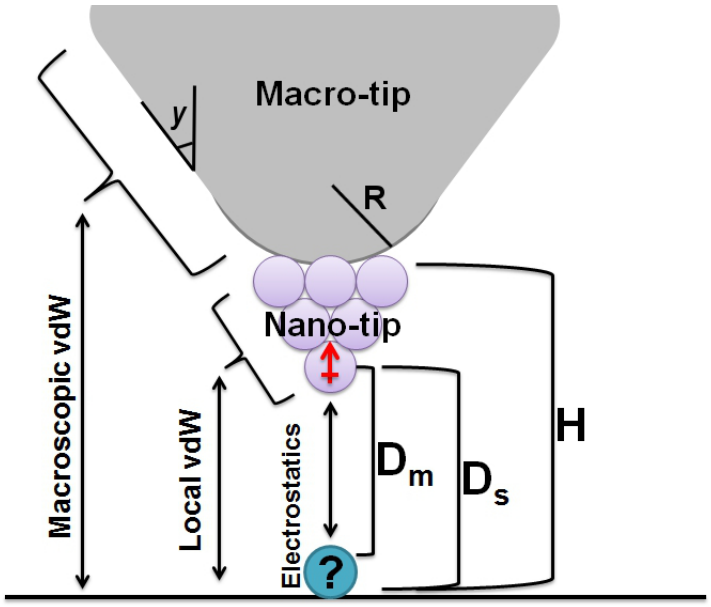

Figure 5.4: A schematic of the proposed tip model imaging the surface and a small molecule. The main contributions to force are macroscopic vdW interactions, local vdW interactions, and mid-range electrostatic interactions. Distance between the macro-tip and the surface is defined as H, distance between the nano-tip and the surface is defined as D_s, and distance between the nano-tip and the molecule is defined as D_m.

experimental data in a regime where only this contribution is dominant. This data can then be used to characterize the macroscopic properties of the tip. I account for the long-range macroscopic vdW interactions using an analytical expression where the parameters are directly fit to experimental data. Within this analytical expression, the macroscopic tip is represented by a conical section with a spherical cap and the force was calculated with respect to distance between the macro-tip and the surface as illustrated in Figure 5.4. The total long-range macroscopic vdW force on the tip can be expressed as follows:

$$F_z(H) = \frac{A_{\mathrm{H}} R^2 (1 - sin\gamma)(Rsin\gamma - Hsin\gamma - R - H)}{6H^2(R + H - Rsin\gamma)^2} + \frac{-A_{\mathrm{H}} tan\gamma(Hsin\gamma + Rsin\gamma + Rcos(2\gamma))}{6cos\gamma(H + R - Rsin\gamma)^2}, \tag{5.2}$$

where A_{H} represents the Hamaker constant, H represents the separation between the tip and the surface, R represents the tip radius, and γ represents the cone angle, as shown in Figure 5.4. This expression was originally derived by Argento et al. and more detailed

information can be found in their publication [208].

Since it is difficult to find unique solutions to equations composed of many variables, I constrained the parameters in order to obtain a physically meaningful fit. The macroscopic tip parameters for this model were constrained using available information about the tip and the materials used in the system. The Hamaker constant A_{H} can be calculated using Lifshitz theory from dielectric constants and refractive indices for a variety of inorganic materials [209]. In this model, I constrained the value to be within a range of 5×10^{-20} J to 60×10^{-20} J to represent a Cr tip interacting with a NiO surface. The tip radius was then constrained within a range of 1.0 to 10.0 nm, since the uncoated sharp Si tip had a radius of 2.0 nm before being coated by 4 nm of Cr. Finally since the tip should be quite sharp, I constrained the tip cone angle γ within a range of 0 to 90°. Using this model, the macroscopic vdW interaction can be calculated with respect to tip-sample separation. This separation was defined as the minimum distance between the surface plane and the macroscopic tip sphere H, as shown in Figure 5.4. The surface plane was defined as the average z-position of atomic nuclei on the NiO(001) surface.

With this model, I was able to optimize a unique set of parameters that well described the experimental data. These parameters were $A_{\mathrm{H}} = 39.6 \pm 11.2 \times 10^{-20}$ J, $R = 3.95 \pm 0.87$ nm, γ of 16.42±1.24°. Using these results, I could then extrapolate the absolute macroscopic tip-sample separation H for a given experimental dataset. This information became critical later on when discussing absolute distances between the nano-tip or dipole moment and the surface since tip-sample separation is typically difficult to obtain experimentally. A comparison between the force curve given by this model and an experimental force curve measured above the NiO(001) surface is shown in Figure 5.5.

With the long-range component accounted for, the next largest contribution to the total force comes from the electrostatic interaction between localized charges present in the metallic tip and the sample. This mid-range interaction is responsible for image contrast when the nano-tip approaches the surface at distances ($\mathrm{D_s}$) between 0.5 and 1.0 nm and dependent on the magnitude of the dipole moment at the metallic tip apex. In order to

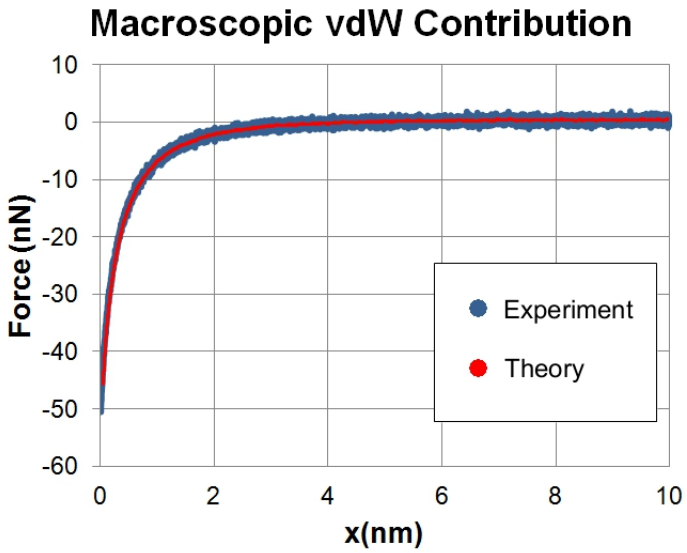

Figure 5.5: The experimental long-range force curve compared with the theoretical long-range force curve. The mathematical functions used were chosen to physically represent the metal coated AFM tip. Optimized tip model parameters: $A_{\mathrm{H}} = 39.6\pm11.2 \times 10^{-20}$ J, $R = 3.95\pm0.87$ nm, $\gamma = 16.42\pm1.24°$. The experimental data was taken with the following instrument parameters: $f_0 = 186.278$ kHz, c = 144±21 N/m, $A_0 = 0.6\pm0.1$ nm, Q = 20996. Note that the theoretical curve is analytical and that these instrument parameters were not needed in this calculation.

come up with a model to represent the total dipole moment of the tip, I examined a contour plot of the electrostatic potential near a three layer Cr nano-tip on the Cr(110) surface, as shown in Figure 5.6.

This contour plot shown in Figure 5.6A shows a spherical feature above the asperity, which could represent the positive lobe of a dipole moment. This spherical feature is centered near the apex atom and I examined the distance dependence of the local electrostatic potential, as shown in Figure 5.6B. This distance dependence corresponds to a dipole moment much better than a simple point charge which exhibits a simple 1/r relationship. In Figure 5.2, the dipole moment of a 3 layer pyramidal nano-tip was previously estimated to be 5 D. However, as seen in Figure 5.6B, the local electrostatic potential at the tip apex is well reproduced by using 3 D point dipole at the apex atom. The 5 D point dipole is unable to reproduce this potential when placed at the apex atom (see Supplementary Figure D.1). This discrepancy is easily explained since the previous DFT calculations estimated the dipole of the entire system, which would include contributions from other features such as

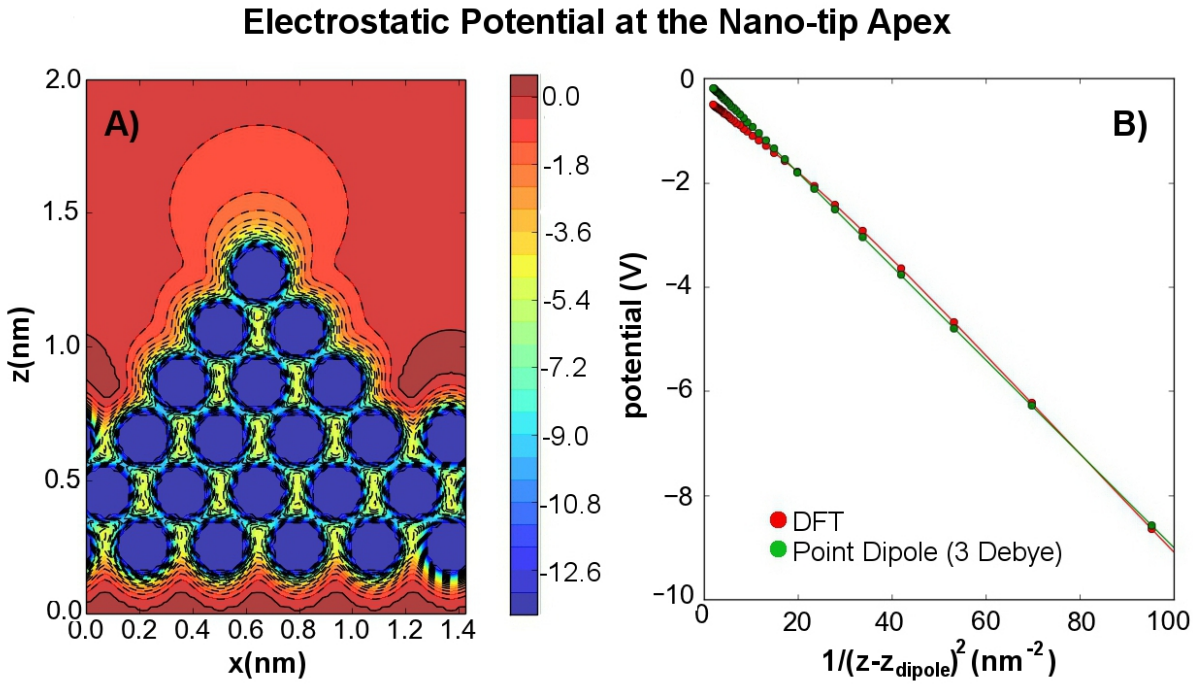

Figure 5.6: A) The electrostatic potential of a system containing a three layer nano-asperity on Cr(110) with a total dipole moment of 5 D. When the isosurface of this electrostatic potential is visualized, a large spherical feature appears above the apex atom that can be interpreted as the positive lobe of a dipole moment. B) A plot of the electrostatic potential with respect to distance away from the nano-tip apex. A 3 D point dipole positioned at the atomic coordinates of the apex atom is able to reproduce the local electrostatic potential obtained from DFT calculations.

pyramid edge atoms that are not near the apex atom.

My results demonstrate that a point dipole model can reproduce the local electrostatic potential at the tip apex, making it a reasonable approximation for representing metal coated NCAFM tips within the appropriate distance regime. If the mid-range electrostatic contribution to force is calculated using a simple point dipole representation, it becomes much simpler to simulate and interpret NCAFM experiments.

The final possible contribution to total force in this model comes from the local vdW interactions. These interactions are computed using a semi-empirical method [176] and include only the vdW interactions between Cr atoms at the tip apex and the sample. However, this contribution depends heavily on the exact atomic structure of the nano-tip, which cannot be probed experimentally. For this reason, I do not include these interactions

in my initial VAFM simulations and only discuss their importance afterwards in order to understand the differences observed between theoretical images and experimental ones.

Calculating Electrostatic Interactions

The electrostatic interactions between a point dipole and a sample can be calculated directly from DFT data, as long as several conditions are met. First, the tip-sample separation must be large enough that it is reasonable to assume that the structural deformation of the metallic tip and the surface can be neglected. This is easily accomplished when using metallic tips with NCAFM, since the ability to take long-range measurements is one of the main benefits of this technique. However, electronic relaxations are often significant and must also be considered. In particular, image charges may contribute significantly to the forces. Fortunately, the surfaces studied in this thesis are bulk insulators, and the only possible image charge in my system would be the one induced within the metallic tip itself by some surface feature. Furthermore, the distance between the image and the surface is much larger than the distance between the tip and the apex and this contribution to force is only a small fraction of the mid-range electrostatic component. The forces resulting from such image interactions can be estimated using previously published models [210].

My calculations estimate that when a typical 10 nm radius AFM tip interacts with a 5 D dipole moment on the surface at a tip-sample separation of 0.5 nm, the component that arises due to an image dipole contributes roughly 5% to the total mid-range force. In NCAFM experiments the tip oscillates continuously and the tip-sample separation usually refers to the distance between the tip and the surface at closest approach. This means that the metallic tip will only spend a small fraction of the oscillation cycle this close to the dipole moment on the surface, further reducing the overall effect of the image dipole. Furthermore, the mid-range electrostatic component is already only a small fraction of the total force (which is dominated by the macroscopic vdW interactions) so the image contribution can safely be neglected in my model for the sake of simplicity.

Within the boundaries of these approximations, the contribution to mid-range forces

can be attributed to electrostatic interactions between the dipole moment at the metallic tip apex and the sample. I approximated the AFM tip in this model as a point dipole far from the surface and the mid-range force between this tip and the sample can be expressed as shown:

$$F_z = \frac{d}{dz}[D_x \frac{dV_E}{dx} + D_y \frac{dV_E}{dy} + D_z \frac{dV_E}{dz}], \tag{5.3}$$

where F is the normal force felt by the tip, (D_x, D_y, D_z) represents the orientation and magnitude of the dipole moment of the AFM tip, and V_E represents the electrostatic potential of the system at each point of interaction. In the case of blunt tips or multi-tips, the tip structure can simply be represented as an array of dipoles. The force between a multi-tip consisting of n dipoles and the surface can expressed as shown:

$$F_z = \sum_{i=1}^{n} \frac{d}{dz}[D_{ix} \frac{dV_E}{dx} + D_{iy} \frac{dV_E}{dy} + D_{iz} \frac{dV_E}{dz}]. \tag{5.4}$$

I then combine this force contribution with the previously described macroscopic vdW contribution to generate a 3-dimensional force field. Using this force field, I performed VAFM simulations using a third party code [184] and produced scan-lines to compare with experimental data. A python script for generating this electrostatic force field from cube files can be found on the supplementary disk attached to this thesis.

Virtual Atomic Force Microscope

The virtual AFM (VAFM) was designed to bridge the gap between theoretical models and experimental data. Since the AFM is a complex instrument, interpretation of the data is rarely trivial and a full simulation of the instrument is necessary. The cantilever and the tip can be approximated using a harmonic oscillator model. The equation of motion of the cantilever [211] can then be expressed as:

$$m\ddot{z}(t) + \frac{m\omega_0}{Q}\dot{z}(t) + cz(t) = R(t)E(t) + F_{int}[x, y, z], \tag{5.5}$$

which describes a harmonic oscillator where m represents effective mass, ω_0 represents the resonance pulsation of the cantilever, c represents the stiffness of the cantilever, and Q represents the quality factor of the probe. The excitation amplitude R_t and signals $E(t)$ are then controlled by the feedback electronics of the instrument during imaging in response to the changing amplitude and frequency of the cantilever. These values are dependent on the oscillation amplitude and frequency of the cantilever. This makes it possible to control critical parameters such as oscillation amplitude A_0 or the frequency shift Δf (calculated with respect to the frequency of a non interacting tip and sample). Finally, F_{int} represents the conservative and dissipative interactions between the tip and the sample. The feedback electronics are modeled using several complex series of circuits composed of oscillators, filters, arithmetical operators, logical operators, and simple controllers. The design and implementation of these circuits is beyond the scope of this thesis and will not be discussed here. A more complete discussion of these models is given by Gauthier *et al.* [211] and was implemented by F. Federici Canova [184] in the VAFM code that I used in the work presented in this thesis.

In order to use the VAFM, values for f_0 ($2\pi f_0 = \omega_0$), c, and Q must be given. Ideally these should match the values provided by the manufacturer for the actual experimental cantilever. Furthermore, A_0 must be provided in order to set the amplitude of oscillation and Δf is required to set the tip-sample separation during imaging. These values will correspond to experimental set points. Finally, the interactions between the tip and the sample F_{int} must be provided in the form of a 3-dimensional force field as previously described. These models allowed me to accurately represent the motion of the cantilever and produce theoretical images that could be directly compared to experimental data. The version of the VAFM code used in this thesis and several example files can be found on the supplementary disk.

However, as illustrated in Figure 1.1, this only represents one component within a complex multi-scale system. An accurate 3-dimensional force field must first be generated before the VAFM code can be applied.

Extrapolating the Dipole Moment

With the previously described model, I was finally able to calculate the mid-range electrostatic interaction using the electrostatic potential of the sample obtained from DFT calculations and combine it with the macroscopic vdW contribution to generate VAFM scan-lines. The VAFM code [184] integrates the equation of motion of the cantilever and models the feedback circuits found within the real apparatus and provides a direct simulation of the real experiment. In all the simulated images I present, the parameters used (f_0, c, A_0, Q, and Δf) are exactly the same as the ones used during experimental AFM operation unless otherwise stated.

The experimental scan-lines presented in this section were taken using the methods described in Section 5.2. NCAFM images with atomic resolution of the bare NiO(001) surface were collected and I averaged 23 scan-lines along the [100] direction from one such image in order to obtain a mean atomic corrugation amplitude. I then adjusted the value of the dipole moment and the height of the nano-asperity in order to reproduce this averaged experimental scan-line, as shown in Figure 5.7. The general procedure I employed can be broken down into several steps. First, the macroscopic tip parameters were fit to a long-range experimental force curve as previously described. Using this model, I extrapolated the height of the macro-tip H that was required to reproduce the experimental Δf of -50 Hz. This was found to be 1.24 nm and represented the distance between the macro-tip and the sample. I then placed nano-asperities on top of this macro-tip and point dipoles at the apex atom of these nano-asperities. It is important to note that the distance between the tip dipole depends on the size of the nano-asperity. Nano-asperities ranging from 1-5 atomic layers high were used in combination with point dipoles ranging from 1-20 D in magnitude. The best agreement with experiment was achieved using a tip dipole moment of 7 D positioned at the tip apex of a 3 atomic layer high nano-asperity. This means that the macro-tip to sample distance was 1.24 nm, while the nano-tip to sample distance was 0.64 nm. The theoretical noise that can be seen in the theoretical scan-line in Figure 5.7 is due to the digital phase lock loop and the integration timestep employed within the VAFM

code.

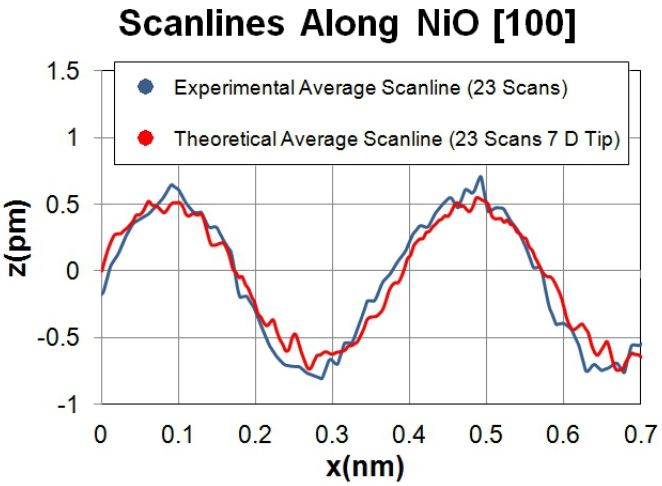

Figure 5.7: Experimental and theoretical scan-lines above the bare NiO(001) surface in the [100] direction. The theoretical scan-line was generated using a 7 D dipole moment and compared to the experimental average scan-line. Experimental parameters: $f_0 = 186.278725$ kHz, $c = 144 \pm 21$ N/m, $A_0 = 0.6 \pm 0.1$ nm, $Q = 20996$, $\Delta f = 50$ Hz.

Although the agreement between experimental and theoretical scan-lines for this dipole moment value and nano-asperity size is remarkably good, it is critical to note that the magnitude and position of the point dipole are interrelated and were not uniquely defined (see Supporting Figure D.2). They can only provide a rough description of the atomic structure of the tip in this case. Additionally, the local vdW interactions between the nano-tip and the surface will depend on the precise structure of the nano-tip which cannot be directly extrapolated from this data. At a nano-tip to sample separation of 0.64 nm, the local vdW contribution to image contrast is negligible. However, these interactions become increasingly important if images are taken at smaller nano-tip to surface distances D_s.

My results clearly show that at large tip-sample separations, a Cr coated tip can be represented as a spherical macro-tip terminated by a pyramidal nano-tip with a dipole moment of a few Debye positioned at the tip apex. Furthermore, these tips can be routinely produced experimentally with a fairly high success rate. Out of 36 metal coated tips, 26 were observed to possess sufficiently large dipole moments and were capable of atomic

resolution. In the other 9 cases the tip was either too blunt or not metallic.

5.4.3 Evaluating the Model: CO on NiO(001)

While the model I have proposed performs reasonably on atomically flat surfaces, the model must be tested on more complex systems. In order to fully evaluate this model, I compare theoretical scan-lines generated using the point dipole approximation with experimental scan-lines and images of small CO molecules adsorbed onto the NiO(001) surface. The CO molecules were experimentally deposited onto the NiO(001) surface and imaged using the same Cr coated tip as the one used to collect atomic resolution scan-lines in Section 5.2 of this chapter. Experimental images collected at constant Δf depict a large number of bright rings with central depressions (donuts) that appear darker than the surface level. These donuts correspond to individual CO molecules that can be found after deposition, as shown in Figure 5.8A. Scan-lines over the centers of 60 of these isolated CO molecules on NiO(001) were taken in the [100] direction, as shown in Figure 5.8B. I averaged these scan-lines to generate a mean scan-line for comparison with my predicted VAFM images. These virtual images were performed using the same point dipole model parameters and macroscopic tip parameters as in the previous section since the experimental tip is the same one that used for those measurements.

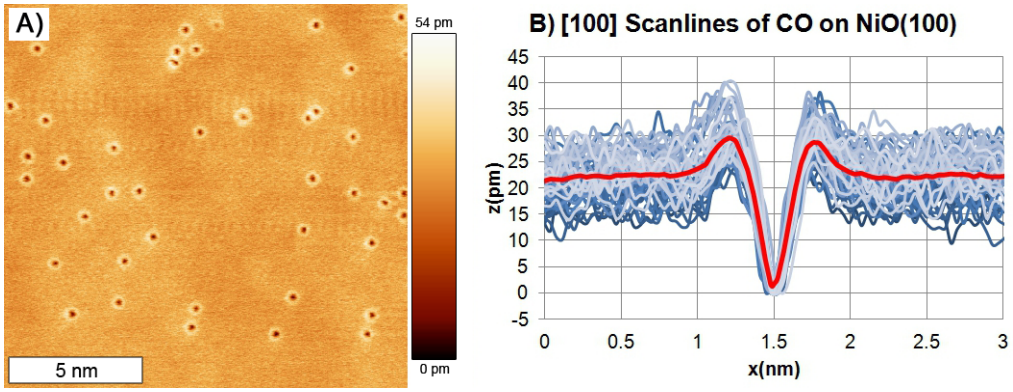

Figure 5.8: A) CO molecules on the NiO (100) surface imaged at 8K as bright rings with a central depression (donuts). B) 60 scan-lines above CO molecules along the [100] direction and a representative average scan-line. Blue lines represent individual experimental scan-lines while the red line represents the averaged scan-line. Experimental parameters: f_0 = 186.278 kHz, c = 144±21 N/m, A_0 = 0.6±0.1 nm, Q = 20996, Δf = -48 Hz.

In order to simulate the electrostatic component of force and generate VAFM images, I performed DFT calculations of the CO molecule adsorbed onto NiO(001). DFT calculations of the isolated gas phase CO molecule predicted a 0.1 D dipole moment along the molecular axis with the positive pole oriented towards the O atom. When adsorbed on NiO(100), the molecule sits perpendicular to the surface with the C atom above a surface Ni atom. I found the adsorption energy to be 0.3 eV, which is comparable to previous calculations [201, 202]. The adsorbed molecule exhibits an increased dipole moment with a magnitude of 0.4 D. The positive end of this dipole moment points away from the surface, or towards the O atom. Additionally, the CO molecule is tilted a total of 6° towards a Ni atom, with Ni-C contributing 2° and C-O contributing 4°. This value is qualitatively in agreement with prior theoretical predictions [201, 202] and within the error range of experimental estimates [212] of 12± 12°. Theoretically, VAFM images generated at 0 K produce a distorted ring structure due to the slightly tilted geometry of the molecule (see Supporting Figure D.3). However, this is not seen in any of the experimental images. This is due to the high surface symmetry in this system, which results in four energetically equivalent configurations for CO on NiO(001). The transitions between these configurations should most commonly occur *via* the lowest energy pathway which I calculated to have a barrier of only 0.006 eV. At the saddle point, the CO molecule sits in a purely upright configuration above the surface. This minute barrier is within the accepted error range of DFT and may be interpreted as negligible. Furthermore, I performed molecular dynamics simulations at 8 K in order to estimate the attempt frequency for switching between these equivalent states. The molecule was found to oscillate very quickly at a rate of 10^{13} Hz. This demonstrates that even at low temperatures, the molecule can rapidly switch between equivalent configurations. Since AFM scan rates are on the order of seconds and much slower than these processes, experimental images would show the average position of the CO molecule rather than the instantaneous position. To account for this, I averaged between the four equivalent tilted lowest energy configurations before producing VAFM images or scan-lines. This was accomplished by summing the four static force fields

and dividing the result by the number of equivalent configurations to produce an averaged force field.

The bright and dark spots in an NCAFM image of CO on NiO(100) taken using a metallic tip can be understood by considering the interactions present in the system. When the tip approaches a CO molecule on the surface, there is an initial lateral attraction between the tip and the molecule that arises due to the interacting dipole moments, as shown in Figure 5.9A. This interaction is responsible for the bright rings or donuts observed in experimental images. However, when the NCAFM tip is directly above the CO molecule, the dipole moment of the tip and that of the CO molecule on the surface are aligned with the positive ends pointed towards each other. This opposing interaction results in the dark spot in the middle of the bright rings. However, since Pauli repulsion would result in a qualitatively similar dark spot, it is difficult to confirm that the depressions observed in my theoretical images and in the experimental images are due to the same mechanism.

In order to determine whether the experimental contrast in question is truly only dependent on electrostatic interactions, I compared experimental and theoretical scan-lines. An averaged experimental scan-line was produced using 60 scan-lines in the [100] direction above isolated CO molecules and a theoretical scan-line was produced by averaging over the four equivalent tilted configurations of CO on NiO(001), as shown in Figure 5.9A. The theoretical scan-line was produced using a 7 D point dipole positioned 0.6 nm below the macro-tip to represent the Cr coated tip while the electrostatic potential of a CO molecule adsorbed onto NiO(001) obtained directly from DFT calculations. In this simulation, the absolute minimum distance between the CO molecule and the nano-tip (D_m) when the tip apex was directly above the molecule was found to be 0.46 nm. The corresponding minimum distance between the nano-tip and the underlying NiO(001) surface (D_s) at this position was 0.78 nm. Since the distance between the nano-tip and the NiO(001) surface is so large, my theoretical predictions indicate that it should no longer be possible to distinguish between Ni and O atoms. This is in agreement with the experimental data and confirms that the values for the absolute tip-sample separations given here are reasonable.

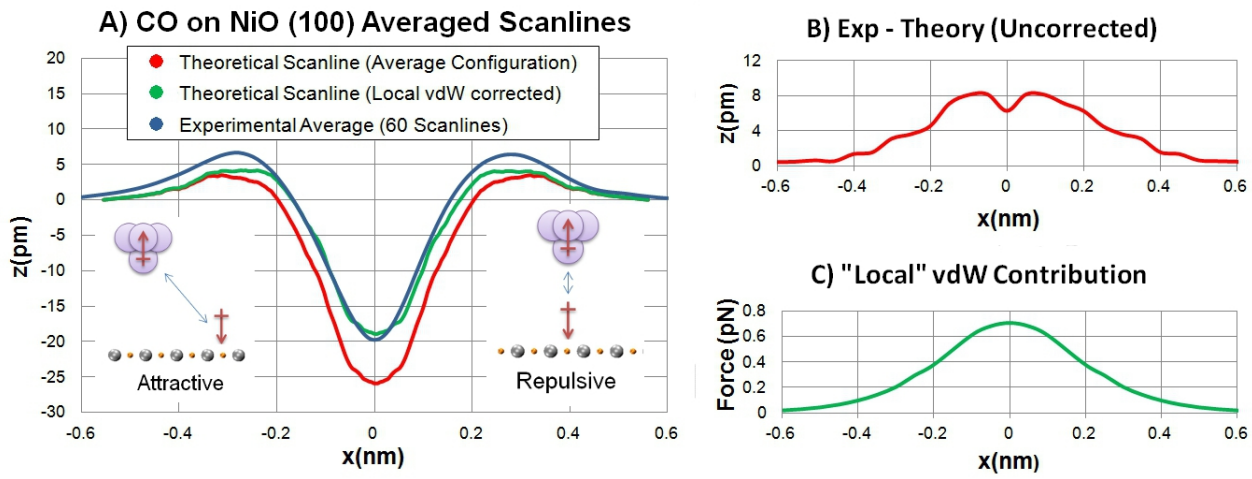

Figure 5.9: A) Experimental and theoretical scan-lines of CO adsorbed onto the NiO(001) surface in the [100] direction. They were produced using the same experimental parameters of f_0 = 190.444039 kHz, c = 151±21 N/m, A_0 = 1.0±0.1 nm, Q = 175903, Δf = -48 Hz. The theoretical long-range forces were fit to experimental data and the tip was represented as a 7 D point dipole 0.6 nm below the macro-tip. The experimental scan-line was produced by averaging over the data for 60 CO molecules on the NiO surface and the theoretical scan-line was produced by averaging over four energetically equivalent tilted states on the surface as well as the upright configuration. Including local vdW interactions improves agreement with experiment. B) The difference between experimental and uncorrected theoretical scan-lines with x=0 representing the center of the CO molecule. C) Local vdW interactions between the pyramidal nano-tip scanning 0.46 nm above a CO molecule. This contribution was computed using a semi-empirical scheme assuming an upright configuration for CO.

Theory predicts that the CO molecule is observed as a bright ring with a dark spot indicating repulsion at the center in agreement with experimental images. However, when comparing the theoretical and experimental scan-lines of CO above NiO(001), it is important to remember that this NCAFM data is produced by adjusting the cantilever height in order to maintain a constant frequency. In this context, the height at which the cantilever oscillates above the bare NiO(001) surface (far away from the CO molecule) can be defined as the surface level. This height will increase in the presence of attractive interactions and decrease in response to repulsive interactions. In the VAFM image that I calculated, the bright ring is 3 pm above the surface level while the depression is 26 pm below the surface level. The diameter of the ring, which I define as the horizontal distance between maxima (the brightest regions of the ring), was calculated to be 0.6 nm. In comparison, the averaged experimental scan-line gives a similar bright ring that is 6 pm above the

surface level with a standard deviation of 3 pm and a depression that is 20 pm below the surface level with a standard deviation of 2.5 pm. The experimentally observed diameter was 0.52 nm with a standard deviation of 4 pm. The total size of the CO molecule is about 1.5 nm in both theory and experiment. Additionally, the average height difference between maxima on opposite sides of the CO molecule can be calculated to see whether or not the theoretically predicted tilted configuration can be seen experimentally. I analyzed the 60 available CO scan-lines to find that this height difference between maxima is only 0.7 pm with a standard deviation of 2.2 pm. This indicates that the height of the ring is constant along the entire perimeter. Therefore, the CO molecule appears to be nearly perpendicular with respect to the surface. Furthermore, the total size of the CO molecule is identical in experiment and simulation, indicating that the image produced by averaging over all equivalent low energy configurations is consistent with experimental results. Since tip-convolution effects are not observed, the NCAFM tip used in these experiments should be atomically sharp in agreement with my pyramidal model of the tip apex.

While the scan-lines shown in Figure 5.9A are in good agreement, there are some minor differences that can be understood by considering the local vdW component to force. Taking the difference between the experimental and theoretical scan-lines yields a bell shaped curve as shown in Figure 5.9B. The largest discrepancy is found near the center of the curve when the NCAFM tip is positioned directly above CO and falls off with increasing distance. This difference may be accounted for by accounting for the local vdW interactions between the CO molecule and the pyramidal nano-tip. This force component will always be attractive and can be expected to reduce the depth of the depression and increase the height of the bright rings. I computed the local vdW interactions between a pyramidal nano-tip 0.78 nm (D_s) above the surface and an adsorbed CO molecule using a semi-empirical scheme [176], as shown in Figure 5.9C. At the point of maximum interaction, when the tip is directly above a CO molecule, my calculations predict that these attractive local vdW forces are 30% as large as the repulsive electrostatic contribution which improves the agreement between theory and experiment. The local vdW corrected scan-line can be

seen in Figure 5.9A. However, it is important to remember that while these forces appear to be the appropriate magnitude and sign to correct the differences between theoretical and experimental scan-lines, they depend heavily on the height and precise geometry of the nano-tip. Since the exact structure of the tip apex cannot be directly extrapolated from experimental data and many of the tip parameters that I optimized are already interdependent, simply correcting for these vdW interactions is difficult. For example, I have averaged over the 4 equivalent lowest energy configurations of CO on NiO(001) to produce the VAFM image. However, if the molecules spend a significant amount of time in a fully upright configuration, the predicted width of the ring and depth of the depression would differ. These interactions may prove to be of critical importance at shorter tip-sample distances. However, in the scope of this work, my results clearly demonstrate a simple point dipole model can achieve quantitative agreement with experiment when measurements are taken at large tip-sample separations.

5.4.4 Tip Sharpness and Resolution

I have shown that the point dipole model achieves excellent agreement with experimental scan-lines, however, collapsing the metallic tip into a single point dipole is too simple in some cases. The previously calculated experimental and theoretical lateral dimensions of CO molecules adsorbed onto NiO(100) were the same size, indicating that the tip appears atomically sharp at the apex and that convolution effects are negligible. In addition, the ring height was shown to be constant along the entire perimeter and implies that the metallic tip is symmetric. These properties are all consistent with the atomically sharp pyramidal nano-tip model. However, this does not prove that the tip actually is atomically sharp. It is important to note that unfunctionalized metallic tips do not produce the same level of contrast as CO functionalized tips in the short-range repulsive regime.

Instead of attempting to somehow prove that these tips are atomically sharp, it is more feasible for me to show that the point dipole model can account for multi-tips as well. Since NCAFM images are always a convolution of the tip, and CO molecules are

atomically sharp, it is possible to reverse the role of the tip and sample and use a CO molecule on the NiO(001) surface to probe the metallic tip instead. One such example is shown in Figure 5.10 where each surface feature is observed as a double ring. The first question that arises is whether these double rings are actually single molecules, rather than two CO molecules side by side. This assumption is consistent with both theoretical predictions and experimental observations. In all other experimental images of CO on NiO(001), such as in Figure 5.8, the bright donuts appear isolated which suggests that CO molecules do not aggregate on the NiO(001) surface. This observation is consistent with my theoretical calculations that predict a 0.4 D vertical dipole moment for adsorbed CO molecules. Since CO always adsorbs to the same surface site, these dipole moments would all be parallel with respect to each other and repel each other on the surface. If the observed feature can be identified as a single CO molecule, the only other explanation is that the metallic tip used to image them contains a double feature instead. Using the point dipole approximation, I represented this tip feature using two point dipoles that both interact with the CO molecule, as shown in Figure 5.10 B.

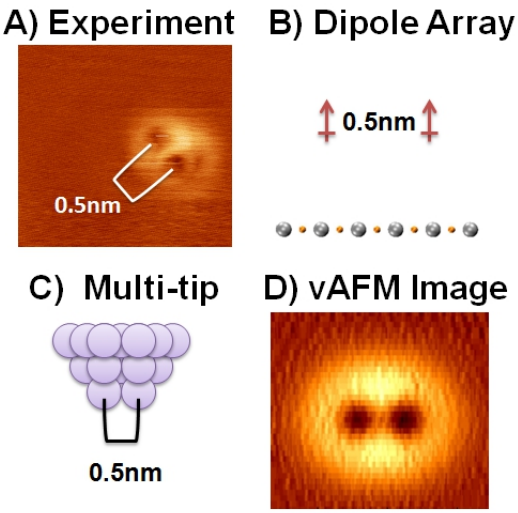

Figure 5.10: A) An experimental image of a double ring feature on the surface of NiO(001). The distance between the centers of these two rings is observed to be roughly 0.5 nm. B) The AFM tip collapsed into two point dipoles 0.5 nm apart. C) An atomistic representation of the Cr nano-tip containing two equivalent apex atoms 0.5 nm apart. D) A VAFM image produced using point dipoles positioned at each apex atom. The observed image shows a double ring feature with a distance of 0.5 nm between centers in agreement with experiment.

In the experimental image in Figure 5.10A both rings are the same size and height, which suggests that the two dipole moments within the tip interact similarly with the molecule. The simplest model that accounts for this is one where the two point dipoles are of the same magnitude and positioned at the same height with respect to the surface plane. The distance between these two dipole moments should correspond to the distance between the two rings in Figure 5.10 which I measured to be 0.5 nm. Using this information, I constructed an atomistic tip model to represent the multi-tip, as shown in Figure 5.10 C. The structure of this tip model is consistent with two neighboring pyramidal Cr asperities grown from a Cr(110) surface. The lateral distance between the two equivalent apex atoms is 0.5 nm, and I placed point dipoles at the atomic coordinates of each of these apex atoms. I then used the same macroscopic tip parameters and experimental set points to generate a VAFM image using the double tip. Unfortunately, this experimental data was collected as part of a different study and did not include a long-range force curve for or a set of atomically resolved scan-lines of the clean NiO(001) surface so I was unable to pursue quantitative agreement. However, Figure 5.10 D shows that qualitative agreement with experiment can still be achieved when using the point dipole model with generic parameters.

My results use the convolution of the tip and the sample to characterize the tip structure and confirm that the images of CO molecules on NiO(001) in Figure 5.8 A were obtained using a tip that appears to be atomically sharp and symmetrical.

5.4.5 Imaging Mechanisms and Contrast

Despite the fact that metallic tips appear atomically sharp and have been shown to resolve individual atoms on the NiO(001) and NaCl(001) surfaces in this study as well as individual CO molecules, the experimental results I have presented have so far been unable to achieve intramolecular resolution. This is largely due to a difference in imaging mechanisms. Such intramolecular resolution is often achieved using CO functionalized tips in the Pauli-repulsion regime, while metallic tips scan the surface at much larger tip-sample

separations. However, since metallic tips have large dipole moments, they may be well suited to probe the electrostatic potential of small molecules on the surface in order to image their dipole moments. Since Co-Salen is a large polar molecule, it provides me with a good example system in which to illustrate this point.

In the previous chapter, I mentioned that the Co-Salen molecule on NiO(001) possesses a 6 D dipole moment aligned along the symmetry axis with the positive end pointed towards the N atoms. This molecular dipole moment can be visualized using an isosurface of the electrostatic potential of the system from DFT calculations, as shown in Figure 5.11A. In this diagram the negative isosurface (Bright) represents regions where the metallic NCAFM would feel an attractive interaction. Experimentally these areas would result in bright spots in the image. The positive isosurface (Dark) represents regions where the tip would feel a repulsive interaction. Experimentally, these areas would then result in dark spots in the image. Note that the isovalue of the repulsive region (0.08 eV) is much smaller than the attractive region (-0.54 eV), which indicates a weaker interaction. In this figure, I employed a smaller isovalue in order to enlarge the repulsive region for the sake of clarity. Furthermore, when Co-Salen is adsorbed to NiO(001), it exhibits an additional 4.4 D vertical dipole moment. When this vertical component is combined with the intrinsic 6 D dipole moment of the molecule, the result is a tilted total dipole moment where the bright attractive region is enlarged, as illustrated in Figure 5.11B. These results show that although the atoms within the Co-Salen molecule cannot be resolved using these experimental techniques, it may be possible to image the dipole moment of the Co-Salen molecule.

In some previously presented images of Co-Salen on NiO(001) (e.g. Figure 4.4), a Cr coated tip was used to obtain atomic resolution of the surface while simultaneously imaging the Co-Salen molecule. However, the tip-sample separations needed to achieve atomic resolution of NiO(001) is less than 0.7 nm. If the combined system is imaged at that tip-sample separation, the tip-molecule separation would be too small and fall into a range where Pauli-repulsion and electrostatic interactions were present. At short distances, the

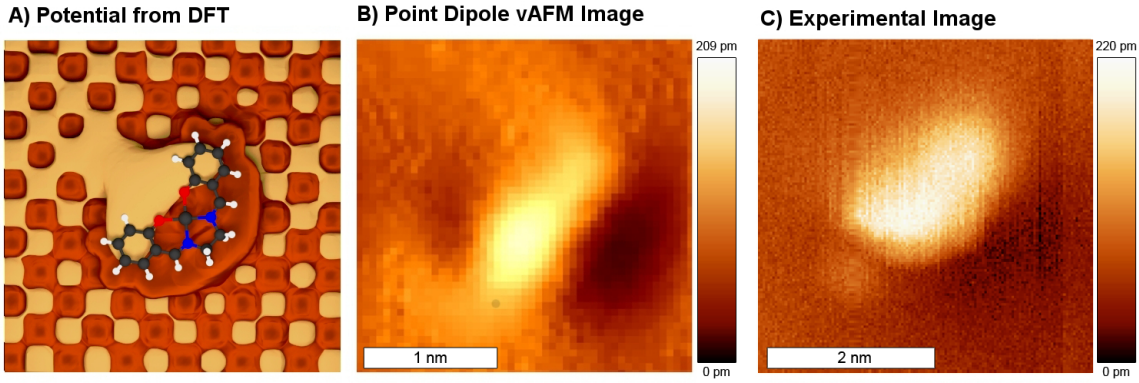

Figure 5.11: A) The electrostatic potential of a single Co-Salen molecule adsorbed onto NiO(001). Bright areas represent the negative isosurface (-0.54 eV) where the tip would experience an attractive potential while dark areas represent the positive isosurface (0.08 eV) or repulsive potential at long distances. B) A VAFM image taken far from the surface. It shows the Co-Salen molecule as a bright oval with a dark shadow on one side. At this range the metallic coated Cr tip is unable to distinguish between similar C or H atoms within the molecule. C) An experimental NCAFM image of a Co-Salen molecule on NiO(001) taken at long-range. Individual Co-Salen molecules do appear as large bright ovals with smaller dark shadows. Experimental parameters: $f_0 = 186.894$ kHz, $Q = 21392$, $A_0 = 5.0 \pm 0.5$ nm, $c = 145 \pm 22$ N/m, $\Delta f =$ -0.71 Hz

bright and dark lobes of the molecular dipole moment could not be consistently identified due to interfering repulsive interactions. However, when Co-Salen is imaged at much greater distances, the horizontal dipole moment of the molecule can be resolved, as shown in Figure 5.11C. The molecule seen in this experimental image consists of a large bright feature with a smaller dark shadow, in agreement with the simulated image in Figure 5.11B. This shadow can be seen in both the trace and retrace images, indicating that they cannot simply be explained as an effect of tip convolution.

These results highlight the mechanistic differences between NCAFM images collected using a metallic tip and prior work performed using CO functionalized tips within the short-range repulsive regime. While metallic tips were unable to resolve atoms and bonds within the molecule, they were able to probe the dipole moment of Co-Salen on NiO(001). This demonstrates that these two methods should be considered complimentary as they target different properties of the system.

5.5 Discussion and Conclusions

Combining my theoretical calculations with experimental results in this study allowed me to confirm that the Cr tips used in this work possess permanent dipoles with their positive ends oriented towards the sample surface. I partitioned the contributions to force into several key components to formulate a complete model of the tip. The long-range macroscopic vdW interactions between the macro-tip and the surface were included by using an analytical expression where the parameters were fit directly to experimental force curves. Mid-range electrostatic interactions were calculated by employing a point dipole model for the metallic tip and considering the interaction between this point dipole and the electrostatic potential of the sample. This approach was then validated by directly fitting the magnitude and position of a point dipole positioned at the nano-tip apex to atomic resolution experimental scan-lines of NiO(001) using VAFM. These optimized parameters were then put to the test by comparing simulated scan-lines above CO molecules adsorbed on NiO(001) to experimental scan-lines. I demonstrated that the point dipole model can achieve quantitative agreement with experiment as long as the measurements are performed at long tip-sample separations. The method I used for computing the electrostatic contribution to force is similar to the method presented in a previous study by Chelikowsky *et al.* [213]. However, the major difference is that in my studies I carefully justify the distance regime and force contribution that is represented in order to produce a quantitative method.

Based on these findings I propose that atomically sharp metallic tips, including metal coated Si cantilevers and wire tips, are generally terminated by a nano-asperity which can be described as a pyramid. The major benefit that this provides is that it eliminates the need to consider a large number of possible tip structures when using metallic tips. In contrast, standard Si or oxidized Si-tips exhibit a wide range of stable configurations and often several of these structures must be tested before good agreement between theory and experiment can be achieved[214]. I have also shown that this type of tip apex possess a significant electric dipole moment (a few Debye) that usually points with the positive end

towards the sample. Furthermore, this effective dipole can be collapsed into a single point dipole at long tip-sample separations, greatly reducing the complexity of calculating VAFM images. These properties facilitate the unambiguous identification of chemical species on polar surfaces at rather large tip-sample separations and since the orientation of the tip dipole is known, the complexity of interpreting experimental data is greatly reduced.

The simple nature of the point dipole model also lends itself to more general applicability. For example, metallic tips can also be functionalized using small CO molecules [188]. Such functionalized tips can then be used to image in constant height mode within the repulsive regime and can achieve intramolecular resolution [215, 216]. However, in the repulsive regime, the tip-sample separation is small and the strong tip-sample interactions at this range can result in image distortions and relaxation effects. Since the CO molecule itself has a dipole moment that points with the positive pole towards the O atom and adsorbs perpendicular to the the surface *via* the C atom on metal surfaces, such tips should also posess a dipole moment the positive pole pointing towards the sample. Therefore, CO functionalized tips can be expected to interact with the sample similarly to metal tips if measurements are taken at the relevant tip-sample separation. Unfortunately, these tips can only be prepared at low temperatures where CO molecules are immobilized on the surface and not all sample systems are suitable for CO adsorption. Another example where this model may be generally applicable is when standard Si tips are used to image the surface at large tip-sample separations. Since these tips are likely to be terminated by inert silanol or bisilanol groups [217], they should also possess dipole moments that can be modeled in a similar way.

In summary, some experimental advantages to using metallic tips are that they can be conveniently prepared *in-situ* and remetallized if they become contaminated. Theoretically, the most stable atomic configuration of the tip apex is a pyramid that possesses a large electric dipole moment that can be represented using a point dipole model. The orientation of this dipole is well justified, greatly reducing the complexity of interpreting experimental data and facilitating the chemical identification of ionic species on insulating surfaces at

large tip-sample separations. These benefits make it an ideal tool for studying molecules on insulating surfaces. The ability to image molecules on bulk insulating surfaces at large tip-sample separations with chemical resolution, accurately interpret the experimental data, and efficiently generate VAFM images for electronically complex systems allowed me to effectively combine my *ab initio* theoretical results with experimental observations.

Chapter 6

Competing Interactions on the Surface: CDB on KCl(001)

Aims: This chapter presents the results of studying the adsorption and film structure of CDB molecules (and several variations) deposited onto KCl(001). In Chapter 4 my results demonstrated how differences in lattice constants change the adsorption properties and film structures of molecules on insulating surfaces due to commensurability between the molecule and the surface. In this chapter, I investigated these effects further by examining several variants of the CDB molecule in order to highlight the importance of commensurability and the fine balance between competing molecule-molecule and molecule-surface interactions within the system.

Methods: I employed DFT in order to calculate each of the possible contributing interactions within the system. Using these results, I proposed models representing the most stable monolayer configurations. These structures were then treated using the point dipole model and VAFM images were generated for comparison with experimental data.

Results: My DFT calculations were able to quantify the various molecule-molecule and molecule-surface interactions present within this system. These competing interactions were used to successfully propose monolayer structures that could be qualitatively compared to experimental images. The CDB molecule was then modified experimentally

by changing specific parts of the molecule. These modifications were designed to target theoretically predicted critical interactions within the system and qualitatively change the morphology of the films formed. Finally, preliminary *ab initio* calculations revealed that CDB molecules should be mobile at room temperature, indicating that a more in depth study of dynamic processes is required.

6.1 Introduction and Prior Work

Thin films composed of organic molecules are of wide interest in surface science, including lubrication, catalysis, and molecular electronics. Controlling the structure of these films is important when designing new materials targeting specific functionalities. At low temperatures, deposited films should consist of random distributions of molecules or atoms. After a certain level of coverage has been reached, more complex structures are formed *via* a variety of growth modes. One example of such behavior was previously described for Co-Salen molecules deposited onto the NaCl and NiO surfaces in Chapter 4. Certain processes, such as transient mobility, may result in the low temperature aggregation of small clusters of atoms at step edges as described in Chapter 3. Furthermore, at room temperature, molecules on insulating surfaces are able to move across the surface and form nanostructures as seen for Co-Salen on NaCl. The growth modes and structures formed depend heavily on the interplay between molecule-molecule and molecule-surface interactions present in the system. Since commensurability with the surface can influence both the adsorption energy and the geometry, it should play a large role in determining which structures are formed and how.

So far, I have studied the adsorption properties of single Co-Salen molecules on NaCl and NiO where qualitatively different growth modes were observed on the two insulating surfaces. I proposed that these observations were primarily due to differences in commensurability which resulted in changes in the molecule-molecule and molecule-surface interactions within the system. An excellent proof of these concepts would be to demonstrate that the morphology of self-assembled structures can be changed by adjusting the molecule-molecule and molecule-surface interactions present in a system. This can be done by changing either the properties of the molecule or the substrate. Indeed, such adjustments designed to target the morphology of molecular structures have previously been demonstrated on metal substrates. Functional end groups have been incorporated into porphyrin molecules to fabricate 1D or 2D structures [218], highly ordered mixed phases of different molecules have been created [219, 220], and polymerization was used to guarantee

good lateral conductivity in the films formed [221, 222]. Furthermore, highly controlled self-assembly has also been demonstrated on semiconductor surfaces [223]. However, such control over the morphology of self-assembled structures on insulators has not yet been achieved.

One of the main challenges when self-assembling films on insulating surfaces is that site specific molecule-surface interactions are typically weak, which results in rapid diffusion and the dewetting of molecular layers [224, 225]. Prior studies have shown that π-stacking interactions between molecules can dominate weaker molecule-surface interactions [224, 225]. In order to address this challenge, two main strategies have been implemented in the past. The first strategy relies on modifying the substrate in order to limit diffusion and prohibit dewetting. Previous studies show that e-beam surface patterning of ionic surfaces limits diffusion [225], while using surfaces with high surface energies, such as calcite, prohibits dewetting [226]. The second strategy focuses on molecular design. It has been shown that some molecules can form wire structures through π-stacking [227, 228], while others can stabilize the molecular layers through hydrogen bonding [229]. Several experimental studies also report using polar groups to enhance adsorption onto ionic substrates [230, 231, 232]. However, due to the wide range of possible applications, there is no single set of guiding principles or design criteria to follow for self-assembled films on insulating surfaces. For example, molecular electronics applications may require that the molecules self-assemble in large, highly ordered, and defect free domains. In contrast, self-healing and the ability to smooth asperities are more important for lubricants, while catalysts aim to provide large numbers of accessible and effective reaction sites.

In this chapter, I discuss my results from using DFT to calculate the adsorption properties of single CDB molecules on the KCl(001) surface in order to characterize the molecule-surface interactions. I then computed the possible molecule-molecule interactions in the system in order to assess the relative strength of these competing interactions. Using this data, I then predicted low energy structures for a monolayer of CDB molecules on KCl(001) and compared my findings to experimental images. Since atomistic models cannot be di-

rectly compared to experiment, I used the point dipole model introduced in Chapter 5 to simulate VAFM images, which could be qualitatively compared to the appropriate experimental images. Finally, I calculated the differences in interactions that would arise from several modifications to the CDB molecule and used my results to explain the experimentally observed differences attributed to these modifications.

These results highlight the importance of carefully balancing the molecule-molecule and molecule-surface interactions when growing thin films on bulk insulating surfaces. The fine balance between these relatively weak competing interactions can be exploited when engineering films geared towards specific applications.

6.2 Experimental Methods and Data

In this chapter I will compare my theoretical results and predictions to experimental NCAFM images. The experiments described here were performed by my collaborators at Aix-Marseille University, and the molecules were synthesized specifically for these studies at the Université de Franche-Comté. A brief description of the experimental work performed is given in this section and more information can be found in our joint publication [233].

6.2.1 Custom Molecules

The molecules described in this chapter were synthesized by S. Lamare, F. Palmino, and F. Cherioux at the Université de Franche-Comté. They were designed with the goal of growing large-scale supramolecular frameworks on insulators *via* molecular deposition. In order to do so, the 1,4-bis(cyanophenyl)-2,5-bis(decyloxy)benzene (CDB) molecule was selected as a starting point to include specific molecule-molecule and molecule-surface interactions. CDB contains a triphenyl core which contains two cyano functional groups and two lateral decyloxy chains, as shown in Figure 6.1.

Each component of the CDB molecule is meant to promote a different molecule-molecule

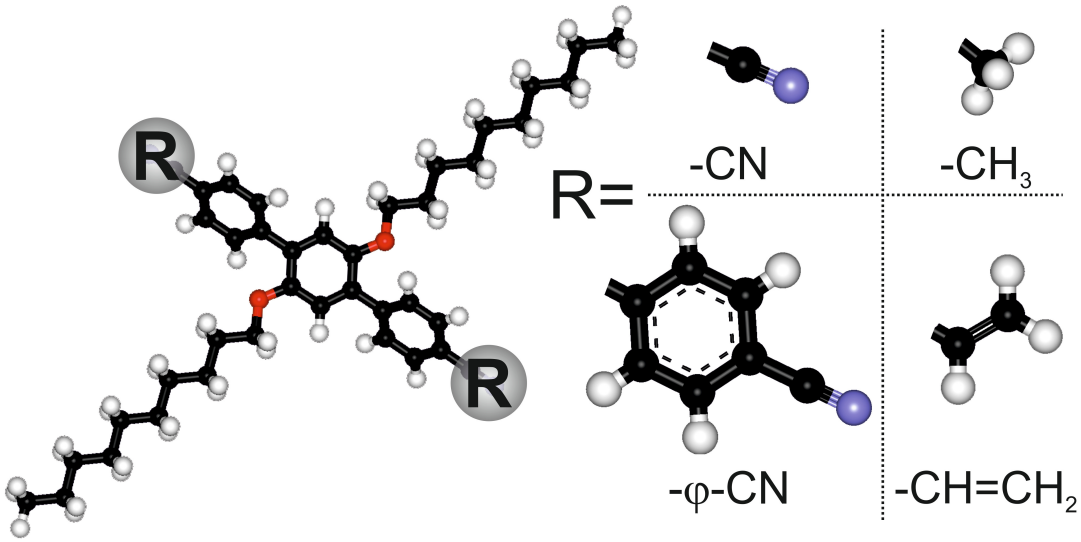

Figure 6.1: An atomistic representation of the CDB molecule and some of the possible structural variations.

or molecule-surface interaction. For example, the lateral decyloxy chains are meant to promote supramolecular self-assembly *via* van der Waals interactions between parallel aligned chains (interdigitation) [234]. The triphenyl core should contribute to molecule-molecule interactions through π-stacking [235]. Finally, the cyano functional groups are meant to provide site specific molecule-surface interactions [230, 231, 232]. Additionally the cyano groups are believed to interact *via* hydrogen-bonding which could enhance molecule-molecule interactions [236]. In order to investigate the role of the cyano groups, they were subsequently substituted by vinyl (1,4-bis(vinylphenyl)-2,5-bis(decyloxy)benzene) groups and methyl (1,4-bis(tolyl)-2,5-bis(decyloxy)benzene) groups.

6.2.2 Noncontact Atomic Force Microscopy

NCAFM experiments were performed by A. Amrous, F. Bocquet, L. Nony, F. Para, and C. Loppacher at Aix-Marseille University. The images shown in this chapter were acquired at room temperature using a commercial AFM (VT-AFM, Omicron Nanotechnology GmbH 65232 Taunusstein, Germany) equipped with home-built electronics and an RHK controller (SPM 1000, PLL Pro II, RHK Technology Inc. Troy, MI 48083 USA). The cantilevers used

in this chapter were Nanosensors (PPP-NCL, resonance frequency 150 kHz, spring constant 30 N/m, quality factor Q approximately 40000) operated at typical oscillation amplitudes A_0 of 10 nm.

The single crystal KCl substrate (MaTecK GmbH, 52428 Jlich, Germany) was cleaved *ex situ*, quickly introduced into UHV, and annealed at approximately 200°C for 1 hour in order to produce atomically clean substrates with large terraces. CDB molecules (and variations) were deposited using home-built crucibles at evaporation rates of approximately 1 ML (monolayer) per minute onto substrates kept at room temperature.

CDB molecules deposited onto KCl(001) were imaged using NCAFM at room temperature. Therefore, it was impossible to resolve single molecules on the surface. Instead, the images collected show a porous mesh-like structure as shown in Figure 6.2A. A closer look at the mesh structure reveals a periodic square network tilted approximately 8° with respect to the <100> direction of the surface, as shown in Figure 6.2B. While the physical meaning of the bright and dark spots in these images is unclear, the experimental data provided me with the periodicity and orientation of the monolayer structure with respect to the KCl(001) surface.

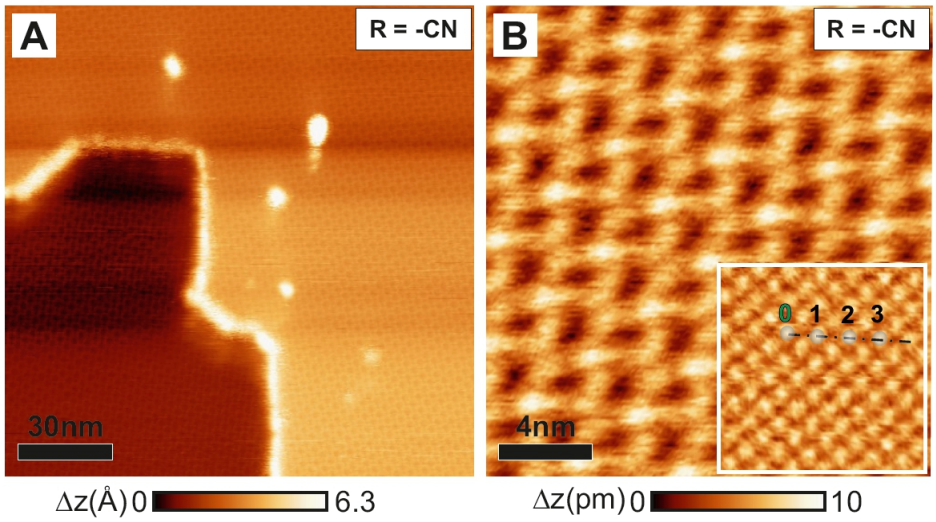

Figure 6.2: CDB molecules on KCl(001), A) NCAFM large scale topography image showing two different molecular domains separated by a monatomic step of the substrate. B) A molecular scale image and an inset indicating the orientation of the substrate with ionic resolution acquired on different areas of the substrate (inset frame edge=4 nm).

My initial task was to propose atomistic structures for the CDB network and select a model of the NCAFM tip in order to produce VAFM images that could be compared directly to these results. In order to do so, I had to accurately represent the molecule-surface interactions using a method that could represent the system periodically while constraining the CDB layer as little as possible.

6.3 Theoretical Methods

In this study I employed a multi-scale approach to study the layer structure of CDB molecules on KCl(001). DFT calculations were used to characterize the adsorption of single CDB molecules on the KCl(001) surface and compare the various competing interactions present in this system. I then used the information gained to predict monolayer structures and calculate their energies using the previously discussed periodic QM/MM scheme. Finally, I applied the point dipole model discussed in Chapter 5 to simulate a VAFM image that can be directly compared to experimental data.

6.3.1 Density Functional Theory

I performed DFT simulations to characterize CDB adsorption on KCl(001) and compare the relative strength of the competing molecule-molecule and molecule-surface interactions in this system. These calculations were made using the mixed Gaussian and plane waves (GPW) [13] method as implemented in the CP2K code. In this work I was able to properly represent the electronic structure of the surface with the PBE GGA density functional and the MOLOPT basis set [19], avoiding the need to use a computationally expensive hybrid functional. The HOMO-LUMO gap of bulk KCl(001) was calculated to be 5.6 eV using this method which can be compared to an experimental value of 7.6 eV [35].

The surface was represented using four atomic layers with one fixed layer at the bottom and three layers of relaxed atoms in order to reproduce the band gap, rumpling, and lattice constants. I employed semi-empirical long-range dispersion corrections [176] in order to

represent vdW interactions in the system, as described in Chapter 2. Finally, I chose the MOLOPT basis set [19] to minimize basis set superposition error (BSSE). Using these methods, the HOMO-LUMO gap of the KCl(001) surface was calculated to be 5.4 eV with a lattice constant of 6.3 Å. Surface K cations were displaced 0.03 Å into the surface plane, while Cl anions protrude 0.03 Å above the surface plane. These results are in line with experimental low energy electron diffraction (LEED) studies that observed a lattice constant of about 6.3 Å and surface rumpling on the order of 0.03 Å [36].

My DFT calculations included geometry minimizations of single CDB molecules and several variations of the molecule adsorbed onto KCl(001). The lowest energy configuration of each molecule was computed by placing the molecule onto the surface in a number of starting positions and optimizing the geometry. These starting positions were obtained by positioning the molecule so that the molecular board was parallel to the surface plane and rotating the molecule by 2° increments. This was repeated several times with the center of mass of the molecule above a cation, an anion, and a bridging site on the surface. I also studied the competing interactions within the system. In order to accomplish this, the molecule was divided into several main components by breaking bonds in order to examine the various contributions to interaction energy between molecules or adsorption energy on the KCl(001) surface. Each of these broken bonds was terminated with a H atom. The fragments studied include A) a hexane molecule representing the hydrocarbon chains, B) a benzonitrile molecule representing the functional groups of the larger CDB molecule, and C) a benzene molecule representing the core of the CDB molecule. Examples files for studying the CDB molecule on KCl using CP2K can be found on the supplementary disk attached to this thesis.

6.3.2 Periodic QM/MM

While the previously presented DFT methods were sufficient to accurately represent the single CDB molecule adsorbed onto KCl(001) with minimal BSSE, monolayer structures could not be handled using standard DFT methods. One of the major limitations to

performing *ab initio* calculations on this system was the need to use several atomic layers of atoms within the surface in order to produce a reasonable HOMO-LUMO gap and the electrostatic potential above the surface. As previously described, a full DFT calculation of bulk KCl in this case gives a band gap of 5.6 eV while a 4 layer slab replicated periodically in x and y to represent the KCl(001) surface produces a band gap of 5.4 eV. While this representation was not problematic when studying isolated molecules, I needed a much larger simulation cell to represent layer structures without imposing heavy constraints on the CDB molecules due to the periodicity of the system. The strategy that I used to reduce the computational cost of such calculations was to simply reduce the number of quantum atoms in the simulation.

In order to accomplish this, I used the 2-dimensional QM/MM embedding scheme [9, 10] described in Chapter 2 to reduce the number of KCl atoms that must be represented quantum mechanically. I treated the atoms within the CDB molecule and the first layer of the surface quantum mechanically, while the remaining surface atoms were represented using a set of classical potentials, as shown in Figure 2.3. These methods allowed me to perform calculations of periodic monolayer structures of CDB molecules on KCl(001).

6.3.3 Virtual Atomic Force Microscope (VAFM)

Theoretical NCAFM images were produced using the point dipole model of the NCAFM tip introduced in Chapter 5. When experimental images are taken at large tip-sample separations, it is reasonable to attribute the observed image contrast to electrostatic interactions between a dipole moment present in the tip itself and the potential of the sample. This method allowed me to produce a force field directly from DFT calculations, using the methods previously discussed in Chapter 5. While the experimental tips employed in this study are not metal coated tips as in the previous work, they may still possess permanent dipole moments near the tip apex depending on tip termination. The Si tips used in this work are likely to be terminated by inert silanol or bisilanol groups [217], which would result in a significant dipole moment at the tip apex. While the actual dipole moment of

this tip termination was unknown, previous calculations suggest that the dipole moment of an isolated silanol group is of the order of 1.5 D [237]. Fragments from the KCl surface also represent very plausible tip contaminants and would result in a dipole moment at the tip apex as well.

In this data set, I did not have access to long-range force curves that I could use to extrapolate the macroscopic tip parameters. Instead, I used the same tip radius (3.95 nm) and tip angle γ of 16.42° as in Chapter 5 to generically represent the Si tip. I used a Hamaker constant of 5.94 x 10^{-20} which was estimated for Si interacting with KCl using the same methods as before [209]. Since this contribution is macroscopic, it has a large effect on the frequency shift observed and can provide useful information regarding the true tip-sample separation when parametrized using experimental data. However, using a generic model in this chapter, I was only able to produce an image that could be used for qualitative comparison to experimental data. The final VAFM simulations were performed using the same tip parameters as in experiments: a 150 kHz resonance frequency, a 30 N/m spring constant, and 10 nm oscillation amplitude. Since Si tips are known to exhibit a wide range of terminations [185, 186], I simulated VAFM images using both negatively and positively oriented dipole moments of several magnitudes at several tip-sample separations for comparison. The best agreement with an appropriate experimental image was found using a positively oriented 10 D tip scanning 0.8 nm above the surface plane.

6.4 Results

6.4.1 Molecule-Surface Interactions

The CDB molecules were synthesized and deposited onto KCl(001) and imaged using NCAFM. However, since this set of experiments was performed at room temperature, I could not unambiguously identify the adsorption geometry and site, as I did previously with the Co-Salen molecule, due to thermal effects. In order to better understand the balance between the molecule-molecule and molecule-surface interactions, I began by characterizing

the adsorption of CDB molecules onto KCl(001). The molecule was positioned in various initial configurations on the KCl(001) surface, as described in the previous section. All atoms within the CDB molecule and the top 3 surface layers were allowed to relax. The lowest energy configuration of a single CDB molecule on KCl(001) is shown in Figure 6.3.

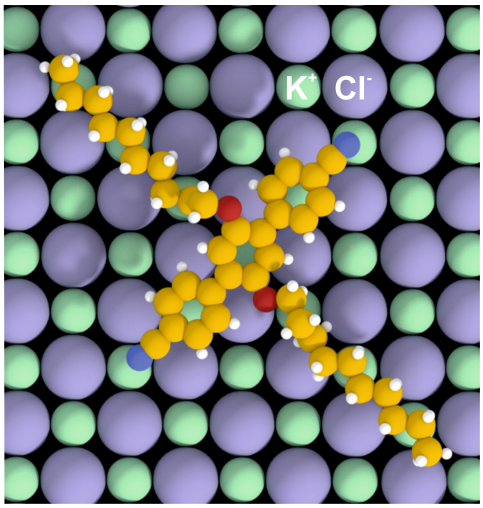

Figure 6.3: The theoretical minimum energy configuration of a single CDB molecule on KCl(001). K surface cations are shown in green while Cl anions are shown in purple. Within the CDB molecule, C atoms are shown in yellow, H atoms in white, O atoms in red, and N atoms in blue. The molecule lies flat on the surface with CN groups positioned above surface cations. The lowest energy configuration for the hydrocarbon arms corresponds to the cation rows on the surface.

The CDB molecule adsorbs onto KCl(001) with the axis of the molecule (defined as the line connecting the two CN groups) oriented along the [110] direction of the surface. In this configuration, the CN functional groups are able to interact with cations on the surface. In addition to this lowest energy adsorption geometry, the CDB molecule can be rotated around one CN endgroup in either direction in order to fit the other CN endgroup above nearby surface cation sites without much change in adsorption energy. This is due to the fact that, although the distance between the cations slightly increases, the molecule is still flexible enough to efficiently anchor to the surface. I partitioned the total adsorption energy in this system into contributions from electrostatic interactions and vdW interactions, as with Co-Salen molecules in previous chapters. The total adsorption energy was calculated to be 3.12 eV with a DFT contribution of 0.7 eV and a vdW contribution of

2.42 eV (calculated using semi-empirical dispersion corrections [20]). This partitioning of the adsorption energy indicates that more than 75% of the total adsorption energy can be attributed to vdW interactions with the surface. However, due to the homogeneous nature of the surface, these interactions are not site specific and do not influence the adsorption geometry of the molecule as much as more localized interactions. The geometry of the adsorbed molecule is instead governed by the electronic interactions between polar groups and the surface.

Further analysis of the adsorption of CDB molecules onto KCl(001) using Mulliken [180] population analysis or Bader charge analysis [181] reveals that a charge transfer within this system is negligible. Furthermore, an evaluation of the work function across the simulation cell reveals a negligible work function change. Finally, I examined an electronic density of states plot of a single CDB molecule adsorbed onto KCl(001), as shown in Figure 6.4.

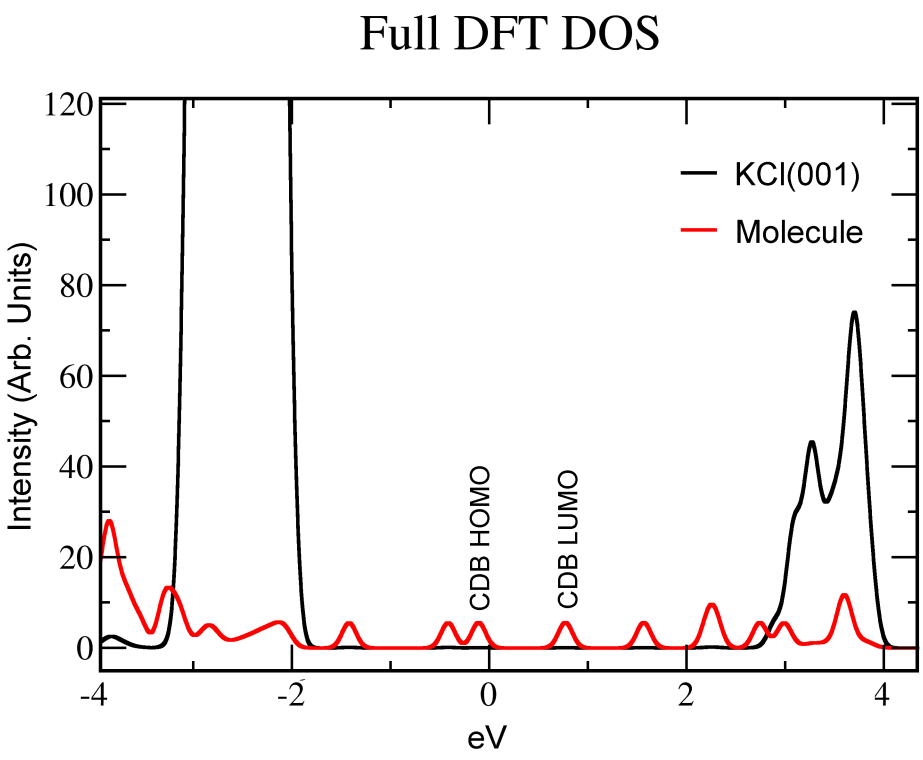

Figure 6.4: The electronic density of states plot of a CDB molecule adsorbed onto KCl(001). The total density of states has been projected into surface (Black) and molecule states (Red). The HOMO of the molecule lies nearly 2 eV above that of the surface and the LUMO of the molecule lies nearly 2 eV below that of the surface.

These results predict that the CDB molecule on KCl(001) can be characterized as physisorption, since the HOMO of the molecule lies nearly 2 eV above that of the surface and the LUMO of the molecule lies nearly 2 eV below that of the surface, as shown in Figure 6.4. Furthermore, it is important to note that these results were also used to validate the QM/MM scheme employed to simulate monolayer structures; a 1 eV reduction in the HOMO-LUMO gap of KCl(100) did not have any effect on the electronic structure of the adsorbed system.

In order to further characterize the different molecule-surface contributions involved in the CDB adsorption, I performed additional DFT calculations using the same setup on representative molecular fragments (cyanophenyl, decyloxy chains) adsorbed to the KCl(001) surface. The strongest molecule-surface interaction comes from interactions between the CN functional group of cyanophenyl and cation sites on the surface. The cyanophenyl molecular fragment adsorbs with N above a cation site while the attached benzene ring adsorbs parallel to the surface plane with combined adsorption energy of 0.7 eV. My results are consistent with previous calculations that give the adsorption energy of a physisorbed benzene ring as 0.5 eV [238] and the adsorption energy of a cyano group on KBr(001) as 0.2 eV [230, 232]. The adsorption energy of the CN group increases above anion vacancies, divacancies, and at step edges and kinks where it can simultaneously interact with more cations. This interaction also represents the strongest electronic interaction present in the system.

The second most significant electronic contribution to the adsorption energy is the interaction between O atoms of the decyloxy chains and the surface. In the unfragmented molecule the central phenyl ring adsorbs in a tilted configuration to minimize steric interactions with adjacent rings. This means that only one O atom can interact with the surface at a time and results in a net interaction that is much weaker than the CN interactions with the surface K ion sites. This is supported by the fact that the O atom to cation interaction was not observed in some low energy configurations (within 0.1 eV of the lowest energy monomer configurations).

Finally, I considered the interaction between the hydrocarbon chains and the KCl(001) surface. Due to rumpling on ionic surfaces, relaxing the surface resulted in the cations being displaced towards the surface (below the surface plane) while the anions were displaced away from the surface (above the surface plane) in agreement with the prior calculations [239] and experiments [36]. However, this does not noticeably change the adsorption energy of hydrocarbon chains on the surface. The differences in energy that I calculated by placing a decycloxy chain on the surface with various chain configurations were minor (<0.05 eV). This predicts that at room temperature, the hydrocarbon chains are expected to be quite mobile in contrast to the anchoring groups.

These results show that most components of the molecule-surface interactions within my system are not site dependent and only have minor effects on the adsorption geometry of CDB molecules on the surface. The only exceptions are the interactions between the CN functional group and cations on the KCl(001) surface and a much less prominent interaction between the CDB O atom and a surface cation. These CN groups can be thought of as the anchoring groups of the molecule. Furthermore, small energy differences between chain orientations on the surface hint that the dynamic properties of the CDB molecule on KCl may be important, especially at room temperature.

6.4.2 Molecule-Molecule Interactions

In addition to the molecule-surface interactions described previously, molecule-molecule interactions also contribute greatly to the structure of supramolecular films on KCl(001). I demonstrated in the previous section that the electronic properties of the molecule do not change significantly when adsorbed to the KCl(100) surface. This allowed me to study interactions between CDB molecules in the gas phase. As expected, oppositely oriented CN functional groups repel each other. However, these CN groups interact favorably with the hydrocarbon decyloxy chains of adjacent molecules. I calculated this interaction energy to reach a maximum of 0.18 eV at an optimal distance of 0.36 nm when the CN and CH_3 groups are positioned end to end. This value can be primarily attributed to vdW

effects with a 0.02 eV contribution from DFT and a 0.16 eV contribution from dispersion corrections.

The benzene rings within the core of the molecule were also predicted to attract each other when oriented in a parallel-displaced (side-by-side) configuration. This interaction was calculated to be on the order of 0.10 eV at an optimal distance of 0.28 nm between the centers of the rings. These values are consistent with prior studies that also estimate that a pi-stacking of parallel-displaced benzene rings can contribute up to 0.1 eV to molecule-molecule interactions [240, 241, 242, 243]. Finally, the hydrocarbon chains also attract each other with an interaction energy of 0.1 eV at an optimal distance of 0.5 nm.

Combining these molecule-molecule interactions with the previously calculated molecule-surface interactions allowed me to propose atomistic models for the supramolecular layer structures observed experimentally when CDB molecules were deposited onto KCl(001).

6.4.3 Monolayer Film Structure

Using the periodicity and orientation of the unit cell extrapolated from Figure 6.2 as a constraint and my previous data on molecule-surface and molecule-molecule interactions, I generated a total of 6 unique stable monolayer structures. These structures were produced by placing CDB molecules in various configurations on the surface and allowing the structures to relax. The lowest energy configuration that I obtained is shown in Figure 6.5. In this configuration, the CN functional groups are predicted to interact with the hydrocarbon chains of neighboring molecules as well as cations on the KCl(001) surface.

Since the CDB molecule is not quite symmetric, films can be either enantiopure (Figure 6.5A), racemic (Figure 6.5B), or somewhere in between. My calculations, however, predict that the enantiopure and racemic configurations are energetically degenerate. In the monolayer configurations shown in Figure 6.5 each CDB molecule gains 0.5 eV of interaction energy *via* neighboring molecules. However, due to distortions from the ideal adsorption geometry with respect to the surface, the monolayer configurations on KCl(001) shown in Figure 6.5 are only 0.3 eV more stable per molecule than isolated CDB molecules

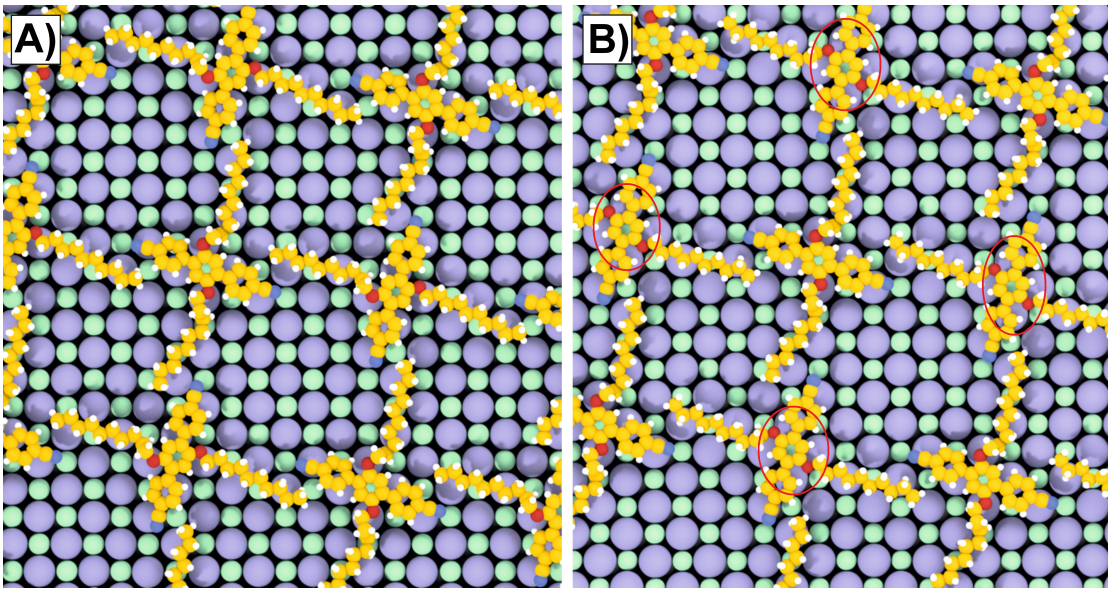

Figure 6.5: Atomistic representations of the monolayer structure of CDB molecules on KCl(001) as calculated by DFT. Surface K ions are shown in green and Cl anions are shown in purple. The C atoms are shown in yellow, H in white, O in red, and N in blue. The depicted enantiopure configuration (A) and the racemic configuration (B) are energetically degenerate. In both configurations the CN groups of the molecule interact with surface cations and the hydrocarbon chains of neighboring molecules. In the racemic configuration every second molecule is replaced with the enantiomer and marked in red for clarity.

on KCl(001). This results in a total adsorption energy per molecule of 3.4 eV in the monolayer configuration compared to a monomer adsorption energy of 3.1 eV.

While CDB molecules in the lowest energy configuration, as shown in Figure 6.5, are more energetically favorable than isolated CDB molecules on the surface, many of my other proposed film structures are only slightly higher in energy. For example, the alternate structure shown in Figure 6.6 results in a 3.3 eV adsorption energy per molecule. This configuration can be obtained by a simple rotation of every second molecule within the previously discussed lowest energy configuration. The energy difference between this structure and the one shown in Figure 6.5 is only 0.1 eV per molecule.

All of the stable monolayer structures that I found resulted in higher adsorption energies (per CDB molecule) than the isolated CDB molecule. Furthermore, all of the stable structures contained CN groups interacting with K atoms on the surface. This confirms that the interaction between the CN anchoring group and the surface is one of the dominant

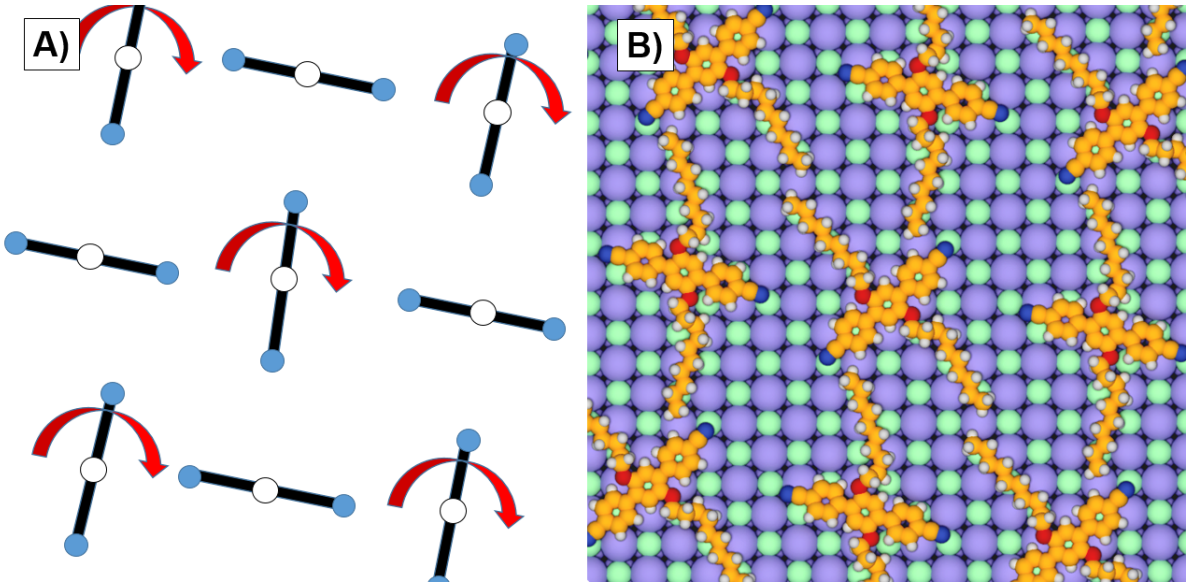

Figure 6.6: A) A schematic diagram of the lowest energy structure shown in Figure 6.5 and how it may be modified to produce the alternate structure. CN groups are shown in blue, the center of mass is indicated by a white circle, and the rotation of every second molecule is illustrated by a red arrow. The hydrocarbon arms are not shown in this diagram. B) An alternate monolayer structure composed of CDB molecules on KCl(001) as calculated by DFT. Surface K ions are shown in green and Cl anions are shown in purple. The C atoms are shown in yellow, H in white, O in red, and N in blue. The CN groups of the molecule are still able to interact with surface cations, resulting in an adsorption energy of 3.3 eV per molecule.

ones in the system.

These results highlight the importance of molecule-surface interactions within my system and provided several reasonable atomistic structures that were thermodynamically stable when compared to CDB monomers on KCl(100). However, it was not possible to directly compare these atomistic models to NCAFM data without accounting for the AFM tip and imaging mechanisms involved.

6.4.4 Comparing with Experiment: VAFM

In order to bridge the gap between experimental images such as the one shown in Figure 6.2 and atomistic models I used the VAFM [184]. In Chapters 4 and 5, I have shown that at large tip-sample separations, images taken over bulk insulating surfaces using a metallic (or metal coated) tip can be simulated using the point dipole model. In this study, the

tips employed are likely terminated by inert silanol groups [217] with dipole moments on the order of 1.5 D [237]. At the AFM tip apex, it is reasonable to expect a larger dipole moment which can be approximated using the previously presented point dipole model.

One of the degenerate stable atomistic structures of the CDB monolayer on KCl(001) is shown in Figure 6.7A. I calculated the theoretical image corresponding to this structure using the VAFM, as shown in Figure 6.7B. The tip used in this simulation incorporated a positively oriented point dipole of 10 Debye and generic macroscopic tip parameters as discussed in the methods section. The simulation was performed at a tip-sample separation of 0.8 nm. Bright lines in the VAFM image were observed above areas corresponding to the main bodies of the CDB molecules and the CN functional groups. The hydrocarbon chains were not visible in these images due to weak electrostatic interactions with the tip dipole. This theoretical image can be directly compared to an experimental image of a CDB monolayer on KCl(001), as shown in Figure 6.7.

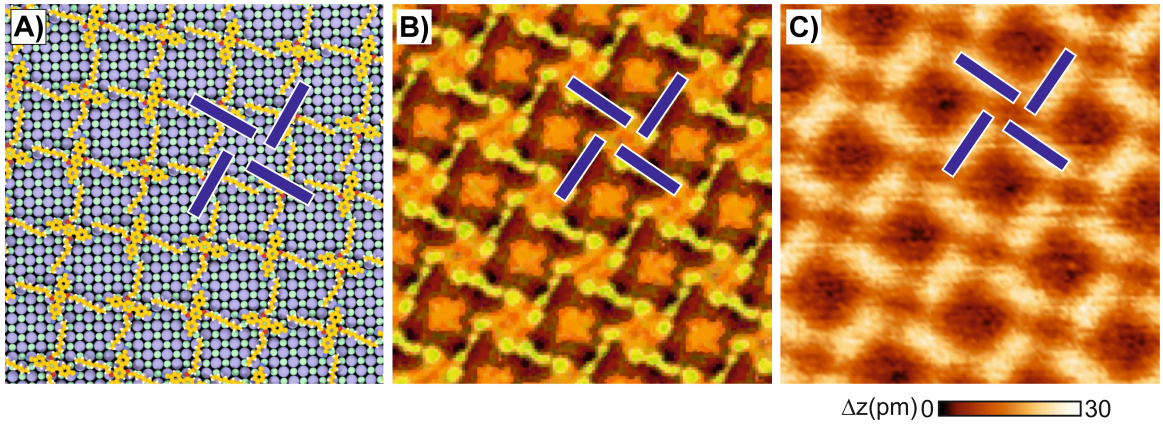

Figure 6.7: A) An atomistic representation of a monolayer of CDB molecules on KCl(001). Surface K ions are shown in green and Cl anions are shown in purple. The C atoms are shown in yellow, H in white, O in red, and N in blue. B) A VAFM image of the monolayer imaged using a 10 Debye point dipole for the tip and a tip-sample separation of 0.8 nm. C) An NCAFM topography image of CDB molecules on KCl(001) taken at room temperature (frame edge=12 nm).

It is important to realize that the experimental image shown in Figure 6.7C and the ones presented previously in Figure 6.2 were not obtained using the same mechanisms. The image in Figure 6.2 was taken at much smaller tip-sample separations, where the point dipole approximation is no longer valid. However, since I did not have any data

on the Si tip used in these experiments, it was not possible to perform traditional VAFM simulations. In order to provide a desired link between theory and experiment, I compared my VAFM image produced using the point dipole model to an experimental image taken at a large tip-sample separation. While occasionally images with measurable contrast were obtained experimentally (such as the one shown in 6.7C), this data cannot be routinely collected due to a lack of signal.

Furthermore, since the macroscopic tip parameters and dipole moment used in these simulations were not extrapolated from experimental data as before, the VAFM image presented can only be qualitatively compared with experiment. However, this qualitative agreement between theory and experiment suggests that the atomistic representation proposed is realistic and supports the suggestion that these networks are not close-packed and do indeed contain porous features.

6.4.5 Experimental Modification of the Molecule

The main objective in this chapter was to study the competing interactions within this system and use the knowledge gained to explain the differences in morphology attributed to several modifications of the molecule. In order to accomplish this, I considered how the film would change in several ways depending on how the molecule was modified. The molecule was then modified experimentally, deposited onto KCl(001), and imaged using NCAFM by C. Loppacher *et al.*

First I considered the effect of weakening the most dominant interaction present in the system. For the CDB molecule, the anchoring CN group was responsible for the square porous structure present on KCl(001). If the site specific CN to cation interaction was weakened, the layer structure is expected to be more close-packed. Furthermore, if the molecule-surface interaction was weakened sufficiently in relation to the molecule-molecule interaction, nanostructures or molecular crystals similar to the ones observed for Co-Salen molecules on NaCl should be observed [3]. Finally, without the repulsive interaction between CN groups, the benzene rings that make up the body of the molecule

would be able to interact with each other more readily.

To demonstrate this, the polar cyano groups were experimentally replaced with less polar vinyl groups and nonpolar methyl groups. When the CN group was replaced using a vinyl-terminated aromatic core, an ordered layer structure was still observed on the KCl substrate, as shown in Figure 6.8. These ordered structures appeared unstable at the island borders, as shown in Figure 6.8A. Although the molecule was only slightly modified, the experimentally observed network formed was no longer a porous square mesh, but a 2D-line structure, as shown in Figure 6.8B. In this image, the observed lattice parameters were found to be a_{1m}=(2.5±0.3) nm, a_{2m}=(1.0±0.1) nm and β=90°, where a_{2m} is the distance between neighbouring molecular centers within each line of molecules.

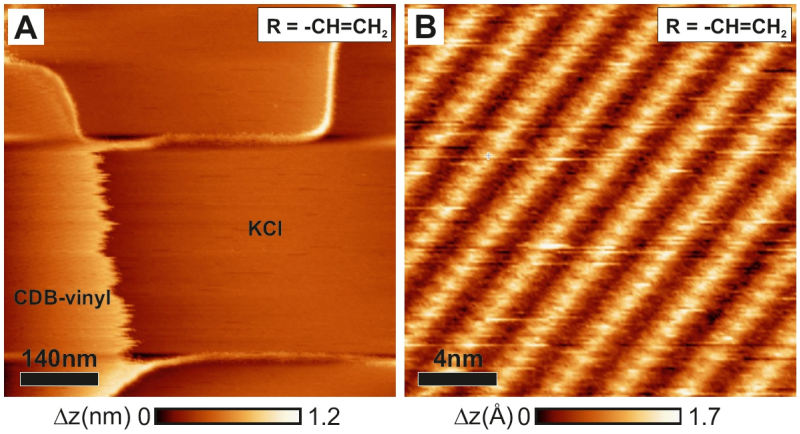

Figure 6.8: A) An experimental NCAFM topography image of vinyl-terminated CDB molecules on KCl(001). The step edges are decorated while island borders appear unstable due to molecular diffusion on the surface. B) An experimental NCAFM topography image of the 2D line structures formed by vinyl-terminated CDB molecules on KCl(001).

The CN functional groups were then replaced using nonpolar methyl groups to further weaken the molecule-surface interactions. The experimental NCAFM images of these molecules can be seen in Figure 6.9A. In these images, monolayer structures are no longer observed. Instead, dewetting occurs and large crystallites are formed on the surface. These structures were confirmed to be molecular crystal rather than a large bundle of KCl step edges by examining the dissipation signal shown in Figure 6.9B. The height of these molecular crystals were estimated using the surface level as a reference, as shown in Figure 6.9C.

Another type of modification applied to the CDB molecule was simply enlarging the

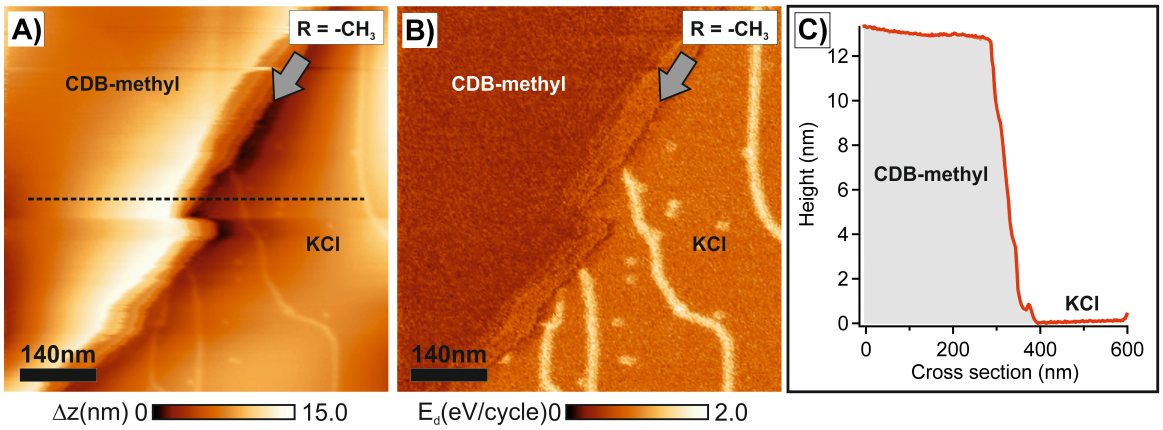

Figure 6.9: A) An experimental NCAFM topography image of methyl-terminated CDB molecules on KCl(001). On the left side, there is an approximately 12 nm-high molecular crystallite. B) A plot of the dissipation signal over methyl-terminated CDB molecules on KCl(001). A clear contrast between the KCl surface and the molecular crystal can be observed. The dissipation signal is larger on the KCl step edges decorated by molecules. C) A height profile illustrating the difference in height between the crystallite and the clean KCl(001) surface.

central aromatic body of the molecule. The molecule was synthesized so that the central body contained a total of 5 rings instead of the original 3 and once again deposited onto KCl(001). The layer structures formed using this molecule were once again observed to be square porous networks, as shown in Figure 6.10

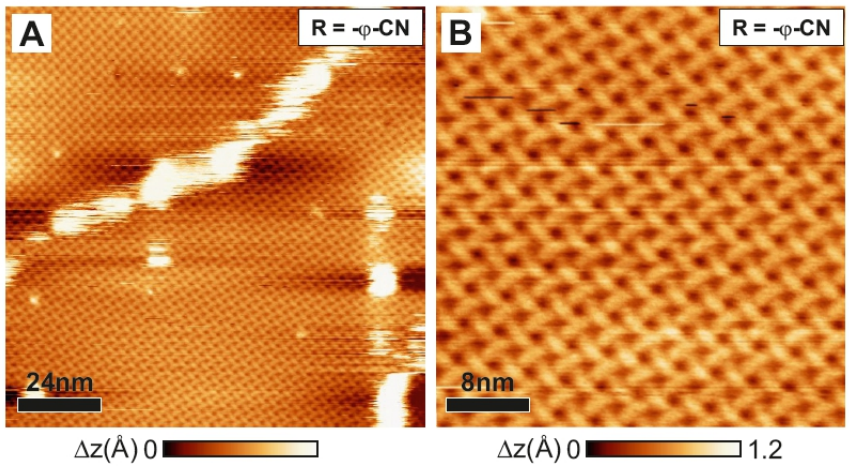

Figure 6.10: A) An experimental NCAFM topography image of CDB molecules with enlarged central aromatic bodies on KCl(001). B) A closer view of the mesh structure formed by the enlarged molecules.

For this molecule, the molecule-surface interactions were left unchanged. The only difference between it and the original CDB molecule was an increased vdW interaction

that did not depend on the adsorption site. It is not surprising then, that the morphology of the film was largely unchanged. The only observable differences were in the increased size of the pores and the orientation of the film with respect to the surface. The first difference can simply be attributed to the elongation of the molecular body, while the second results from a change in the CN to CN group distance. This distance determines the orientation of the single molecule on the surface, since both CN groups prefer to interact with cations. When the central body of the CDB molecule was elongated, the minimum energy configuration no longer corresponded to the <110> orientation.

6.5 Discussion and Conclusions

In this chapter I studied the fine balance between molecule-molecule and molecule-surface interactions within the CDB on KCl(001) system using DFT. I calculated all the possible molecule-molecule and molecule-surface interactions within the system and compared their relative strengths in order to identify the dominant interactions that influence the morphology of the film. My results allowed me to successfully propose monolayer structures and generate VAFM images that could be directly compared to experiment in order to interpret NCAFM images. This allowed me to identify the atomistic model that gave the best agreement with experimental data.

However, many of the monolayer structures that I generated were within 0.1-0.2 eV per CDB molecule of the lowest energy configuration. At room temperature, it is unclear whether the true structure should be represented as an average of several configurations, or a single defect-free network. Furthermore, I predicted that the racemic and enantiopure structures shown in Figure 6.5 are degenerate, making it even more difficult to deduce the exact atomic structure of the film.

Since the experimental data presented depicts regular defect free networks, it is reasonable to infer that room temperature NCAFM provides information on the average position rather than the instantaneous position of atoms on the surface. For example, the hydro-

carbon chains of the molecule were predicted to be stabilized by interactions with the CN groups of neighboring molecules. However, at room temperature, these relatively weak molecule-molecule interactions can easily be overcome.

Using the knowledge gained from my studies of competing interactions within the system, I then proposed several experimental modifications to the CDB molecule. My calculations predicted that the strongest site specific interaction (the CN to surface cation interaction) played a large role in determining the structure of this network. This prediction was verified by experimentally altering the strength of this interaction by replacing the CN functional group. When the interaction was weakened using a vinyl group, the molecule-molecule interactions within the system became more dominant, resulting in the formation of a more close-packed 2D line structure. When this interaction was further weakened by replacing the CN group with a methyl termination, the relative strength of molecule-molecule interactions within the surface resulted in the dewetting of the molecular monolayer. These modified molecules were still able to adsorb to KCl(001) terraces and decorate step edges initially, however, since the molecule-molecule interaction became stronger than the molecule-surface interaction, the formation of large molecular crystals became favoured over the previously observed monolayers. Finally, it was shown that elongating the central body of the CDB molecule effectively enlarged the size of the experimentally observed pores.

While these results validated many of my theoretical predictions, they also indicated that true control over the morphology of the networks formed had not yet been achieved. Since the growth mode or self-assembly mechanism may influence the morphology of the final network, I was not able to predict the structures that would be formed as a result of my suggested modifications. In order to address these issues, simply understanding the relative strengths of the competing interactions within the system was not enough; a full understanding of the growth process and the dynamic behavior of the network structure is still needed.

In summary, I have studied the competing molecule-molecule and molecule-surface in-

teractions within the CDB on KCl(001) system that influence film structure. These results were used to propose atomistic models and generate VAFM images that could be directly compared to experimental images. The CDB molecule was then modified experimentally in order to adjust the competing interactions within the system and qualitative change the morphology of the structures formed. These differences in morphology were explained using theoretical estimates of the relative strength and dominance of various interactions.

Chapter 7

Dynamic Properties on the Surface: CDB on KCl(001)

Aims: This chapter presents the results of studying the dynamic properties of CDB molecules on the KCl(001) surface. In Chapter 6, I proposed atomistic models for the experimentally observed networks of CDB on KCl(001). It was apparent, however, that the ground state model of the system is only approximate as it does not consider any dynamic effects. I had to extend the size and time scales of my simulations in order to study the dynamics of molecules within the layer and to advance my knowledge of the film growth process.

Methods: I combined the efficient QM/MM scheme with genetic algorithm (GA) methods in order to parametrize a classical force field for CDB molecules on KCl(001). Molecular dynamics and energy/force calculations were performed using the QM/MM scheme to generate a large data set that was used as a fitting library. I then developed a GA code in collaboration with Filippo Federici Canova that used this data to simultaneously optimize all the necessary parameters to produce complex molecule-surface force fields using a variety of functional forms. These force fields were then screened using properties such as adsorption energy and force matching. This force field was then used to perform large scale molecular dynamics simulations to study the dynamic properties of the system.

Results: A reasonable force field for CDB on KCl(001) was produced and used to study diffusion, rotation, adhesion to step edges, and structure stability on the surface. The molecule was predicted to be mobile enough on the clean KCl surface that NCAFM experiments should not be able to image it. At step edges, however, a calculated increase in adsorption energy suggests that CDB molecules can spend enough time at step edges to be observed by NCAFM experiments. Finally, the previously proposed monolayer structure was shown to be stable at room temperature and eventually dewet into large CDB droplets at higher temperatures.

7.1 Introduction and Prior Work

So far, I have been able to combine my theoretical studies with NCAFM experiments in order to accurately interpret experimental data, characterize interactions, and verify my methods using experimental observables. My studies have progressed from studying single atoms and molecules up to monolayer structures of large organic molecules on insulating surfaces. However, the mechanisms behind film formation and other dynamic effects that occur at room temperature have not yet been addressed. These processes must be explored theoretically due to the relatively long time scale of NCAFM experiments.

Further insight into these growth processes can be achieved through large scale molecular dynamics (MD) simulations. However, the computational cost of performing such MD simulations using *ab initio* methods is prohibitively large. These studies must be performed using classical force fields instead. However, a major challenge that must first be overcome is the lack of complete classical interaction models for my system. While many of the components of these interactions are readily available, the molecule-surface interaction in particular is system dependent and must be parametrized for each system of interest. Recently, Wright *et al.* parametrized molecule-surface force fields for small proteins on Au(111) and Au(100) using *ab initio* data [244, 245] by incorporating existing protein force fields and generic Au-Au parameters.

Since organic molecules can be modeled as combinations of elementary building blocks, several transferable force fields are available (CHARMM [246, 247, 248], AMBER [249], UFF [250], etc.), to describe their intramolecular, bonded interactions. Non-bonded interactions can be represented using Lennard-Jones (LJ) or Morse potentials which are obtained by mixing atomic parameters in a simple fashion. Typically only minor adjustments are necessary to reproduce experimentally observable properties (such as crystal structure, density, and viscosity). Classical models are also readily available for a wide range of solid surfaces. These force fields are usually optimized to reproduce empirical data, such as lattice structure, compressibility, and vibrational spectra. In many cases LJ potentials are not able to reproduce the strong short-range interactions found in solids and

more flexible functional forms are used. Unfortunately, these potentials cannot simply be mixed with LJ models for organics to obtain molecule-surface interactions and must be parametrized seperately.

Creating molecule-surface forcefields is a complicated task for several reasons. First of all, unlike pure fluid or solid systems where experimentally measured macroscopic properties can be used as fitting criteria, nanoscale measurements of large molecules adsorbed on surfaces are not readily available or easily interpreted. The interpretation of such experimental data often relies on *ab initio* calculations, which could be used to produce fitting criteria. These techniques, however, cannot easily treat large organic molecules on surfaces as many such systems exceed the capabilities of present computers.

In some cases, the molecule can be separated into smaller fragments to reduce computational cost. A force field representing each fragment is then separately parametrized using *ab initio* data and the results are combined to create a force field for the full molecule. However, this procedure is highly dependent on the molecule and cannot be automated. It is both time consuming to formulate and to implement, requiring a significant amount of chemical intuition. Despite the fact that the fragmentation approach has been shown to produce reasonable force fields, inaccuracies often appear in the the properties of larger molecules represented by combining the force fields of individual fragments [251, 252, 253]. Studying large molecules on surfaces further increases the complexity of the system and as a result increases the error that may arise from an incomplete description of the full molecule. On the other hand, due to the modular nature of organic molecules, it is often unrealistic to re-parametrize the force field for every small variation of a molecule. This combination of challenges indicates the need for an efficient systematic procedure for parametrizing transferable molecule-surface interactions in complex systems, which is currently lacking.

A more desirable approach would be to let the computer optimize a classical model, based on a set of *ab initio* data for the full system. Unfortunately, methods that are guaranteed to find the best solution, such as least squares fitting, scale exponentially with

the number of interdependent parameters to fit and are not practical for such complex systems. In order to meet this challenge, I employed GA methods [254] which have been popularized in the context of structure prediction in the past [255]. Indeed, it is shown to produce reasonably good solutions [256, 257, 258, 259, 260] for many small systems. In particular, it has been successfully used to parametrize a variety of complex reactive force fields for small molecules [261].

In this chapter I first introduce a method for efficiently fitting classical force fields to represent the molecule-surface interactions between a large organic molecule (CDB) and the surface (KCl), by using *ab initio* data as a fitting criteria. This genetic algorithm (GA) based method is applicable to any system and can be generalized to any force field model. The force field produced by this method is then used to simulate the dynamic properties of CDB molecules on the KCl(001) surface.

7.2 Theoretical Methods

7.2.1 Producing Data for Parametrization

One of the biggest challenges is ensuring that the force field is able to properly describe the full molecule-surface interaction. In order to avoid the need for fragmentation, I employed the hybrid QM/MM method that was described in Chapter 2 and used in Chapter 6. In this work, I represented the KCl(001) surface using one layer of quantum atoms and three layers of classical atoms. The QM region was treated in the same way as the DFT calculations described in the previous chapter. The MM region was represented using a set of classical parameters by Catlow et al. [33] and the charges were smeared using Gaussian functions according to ionic radii as before. Using this treatment, the KCl(001) surface was calculated to have a band gap of 4.4 eV and produced surface rumpling and lattice constants in good agreement with experiment, as shown in Chapter 2. It is important to note that electronic interactions between the molecule and the surface was well preserved in the QM/MM method, as shown in Figure 6.4. This is critically important in validating

the use of QM/MM methods with this system.

Before optimizing any parameters, I first needed to collect enough *ab initio* data from QM/MM calculations to fully represent the molecule-surface interaction. This was done by compiling a training set for the CDB molecule on KCl(001) which contained information on the forces acting on each atom in the system over a series of 210 atomic configurations or frames. The first 80 of these frames were obtained directly from QM/MM MD calculations performed using the ground state as the initial configuration. These calculations were performed using a 1 fs timestep while keeping the number of atoms, volume, and energy of the system constant (NVE). The atoms in the system were then assigned randomized velocities to produce a temperature of 500 K before letting the system evolve over time. Finally, a snapshot was collected and added to the database every 10,000 timesteps. The starting position of the molecule was then rotated by 15°, 30°, and 45° to generate 3 additional starting configurations and 30 additional frames were collected from each of these simulations for a total of 90 additional frames. It is important to note that the system was not equilibrated at the beginning of these MD simulations. This is because these calculations were simply meant to probe as many configurations as possible rather than model the system at equilibrium. The final 40 frames were created by manually positioning the molecule at extreme (both near and far) distances with respect to the surface. These frames represented situations which would not normally be probed *via* MD and provide information about the system when CDB is farther or closer to the surface plane than normal.

7.2.2 Classical Representations

While complete force fields representing CDB molecules on KCl(100) are not readily available, many of the individual components have been previously derived. Since high quality force fields are available for some of the interactions in the system, it makes sense to use them when possible. The interactions within the system can be partitioned into several categories, as shown in Figure 7.1.

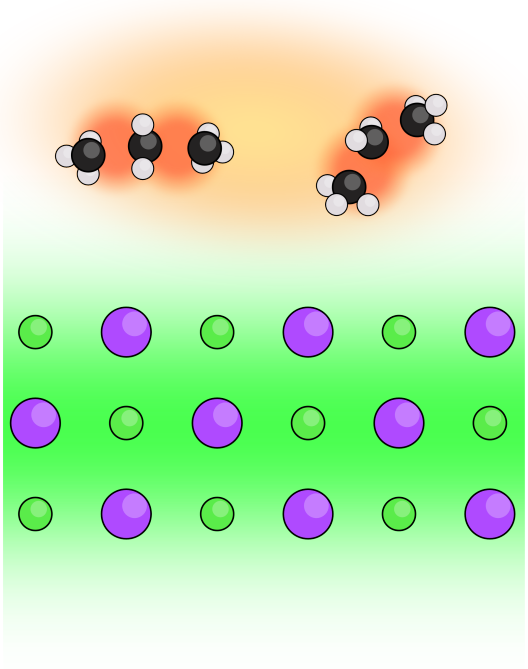

Figure 7.1: A schematic illustration of the known interactions in the system. Red regions represent intramolecular interactions while orange regions represent the molecule-molecule interactions obtained from CHARMM. The green region corresponds to interactions within the KCl surface. The molecule-surface interactions between the CDB molecule and the KCl(001) surface were not available in literature.

Organic molecules are well studied and a number of popular force fields are available. For this study, I selected the CHARMM force field [262] to describe the intramolecular interactions within CDB molecules. These regions are shown in red in Figure 7.1. The CHARMM force field also includes molecule-molecule interactions which are shown in orange in Figure 7.1. This accounts for all of the bonded interactions within CDB, and provides a set of Lennard-Jones atomic parameters to use for non-bonded short-range interactions. Since the CHARMM force-field does not provide partial charges, I obtained them by performing Mulliken population analysis on my DFT calculations of an isolated CDB molecule.

The KCl(001) surface has also been studied extensively in the past. For the sake of continuity I used the same classical potentials [33] as in the previously described QM/MM scheme to describe interactions between surface atoms. Since the shell model was not implemented in the QM/MM scheme within CP2K, I have fixed the positions of the shells

to the positions of the cores in my force field as well.

This accounted for all of the interactions within the system, other than molecule-surface interactions which were not available in the literature. These interactions were parametrized directly using *ab initio* data. I tested several different potential forms for the short-range interactions between CDB and KCl models.

The first two fitting models were of the Lennard-Jones form as shown:

$$\begin{aligned} V_{ij}(r;\mathbf{p}) &= 4\epsilon_{ij}\left[\left(\frac{\sigma_{ij}}{r}\right)^{12} - \left(\frac{\sigma_{ij}}{r}\right)^{6}\right] \\ \mathbf{p} &= \{\epsilon_{ij}, \sigma_{ij}\}, \end{aligned}$$

where $\mathbf{p}$ is the parameter vector, i is an atomic type within the CDB molecule, and j is an atomic type within the KCl surface. In the first model, only the atomic parameters ϵ and σ for K and Cl were optimized. All of the mixed interactions (between KCl and the CDB molecule) were then obtained by mixing these parameters with the LJ parameters from CHARMM using Lorenz-Berthelot rules [263]. This model, Lennard-Jones Mixed (**LJM**), has a total of four fitting parameters. In the second model, all of the pairwise interactions were parametrized independently. This model is labelled Lennard-Jones All (**LJA**). Since this representation used 13 different atomic types to represent the CDB molecule and 2 atomic types for the surface, a total of 52 fitting parameters were needed to account for the molecule-surface interactions.

I then considered the Morse potential form [264]:

$$\begin{aligned} V_{ij}(r;\mathbf{p}) &= D_{ij}\left[e^{-2\alpha_{ij}(r-\rho_{ij})} - 2e^{-\alpha_{ij}(r-\rho_{ij})}\right] \\ \mathbf{p} &= \{D_{ij}, \alpha_{ij}, \rho_{ij}\}, \end{aligned}$$

In this representation each pairwise interaction was independently optimized, resulting in a total of 78 parameters. This model was labelled **MRS**. I also considered the Fumi-Tosi

potential [265]:

$$\begin{aligned} V_{ij}(r;\mathbf{p}) &= A_{ij}\exp\left(\frac{\sigma_{ij}-r}{\rho_{ij}}\right)-\frac{C_{ij}}{r^6}+\frac{D_{ij}}{r^8} \\ \mathbf{p} &= \{A_{ij},\sigma_{ij},\rho_{ij},C_{ij},D_{ij}\}, \end{aligned}$$

which resulted in a total of 130 parameters and was labelled **FT**.

Each of these potential forms was evaluated to find a best fit for representing CDB molecules on the KCl(001) surface. Since they were originally designed for a variety of systems, it is important to ensure that the best one is chosen when parametrizing a new force field.

7.2.3 Genetic Algorithm (GA)

Due to the large number of interdependent force field parameters that must be optimized in each of the described models, I could not use simple systematic optimization algorithms. In order to overcome this challenge, I worked with Filippo Federici Canova and wrote a home-built GA code using the algorithm shown in Figure 7.2A. This implementation of the algorithm creates a population of N elements $e_0, e_1, ..., e_{N-1}$ composed of randomized genomes. These genes represent the force field parameters and can be evaluated and intermixed to produce an offspring population. Elements that are assigned higher fitness values are more likely to be chosen for reproduction, passing their characteristics onward to the next generation. After many generations, the population adapts to produce an increasingly accurate force field. The GA code can be found on the supplementary disk attached to this thesis.

In our implementation, the genome e_k is the parameter vector $\mathbf{p}$ within one of the previously described potential forms. Each parameter p is constrained within an interval of $[p_{min}, p_{max}]$. This prevents the GA from finding unphysical, yet numerically superior solutions, such as negative length scales. Furthermore, in this scheme the parameters were rounded to the second decimal place, so that identical elements could be easily identified.

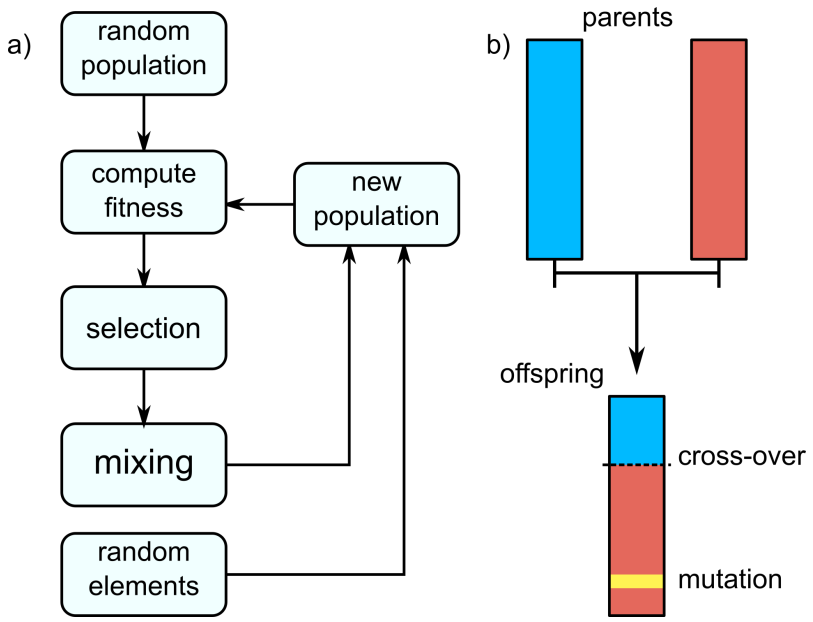

Figure 7.2: A) Schematic description of the standard GA. B) The mixing procedure with cross-over and mutation operations.

When these duplicate elements appear within the same population, one of them is retained while the remaining clones are randomized. This way I could reduce the rate at which the entire population would converge to one solution. Since GA methods are not subject to the variational principle and are not guaranteed to find the optimal solution, this apparent convergence should be avoided when possible. Finally, an additional 5% of the population is randomized every generation, introducing fresh genes into the population to further reduce artificial convergence.

In order to select the best members of the population, I then had to define a fitness criteria. In this study the fitness of a particular element $f\left(\mathbf{p}_{ij}\right)$ was defined as the difference between molecular forces calculated using the previously described QM/MM methods and those obtained using classical methods as shown:

$$f\left(\mathbf{p}_{ij}\right) = -\frac{1}{N_{\mathrm{CDB}}}\left\langle \left|\vec{F}^{\mathrm{MD}} - \vec{F}^{\mathrm{DFT}}\right|^2 \right\rangle_{\mathrm{frames}}, \tag{7.1}$$

where N_{CDB} represents the number of atoms in the CDB molecule, and $\vec{F}^{\mathrm{MD/DFT}}$ represent the total force on CDB obtained from the classical model and QM/MM, respectively. This discrepancy is then averaged over all atomic configurations in the training set of data.

As the classical approximation is optimized to reproduce *ab initio* data, $f(\mathbf{p}_{ij}) \leq 0$ should approach zero. It is important to note that the total molecular force was used in this implementation to cancel out any interfering intramolecular contributions. In this way, the inherent mismatch between CHARMM and DFT interactions are not allowed to influence my molecule-surface parameters.

After the fitness of each element was evaluated, they were ranked in order of descending fitness, and N pairs were chosen at random for mixing. The probability of choosing any particular element e_k was set to $e^{(-k/\lambda)}$ where:

$$\lambda = \frac{\log(N)}{N-1}. \tag{7.2}$$

In this scheme the probability $P(e_{N-1})$ of selecting the worst element is $P(e_0)/N$. This is somewhat of an arbitrary choice, however, it ensured that elements with low fitness were still occasionally selected, enhancing diversity within the population.

Finally, the mixing of elements e_i and e_j was performed using a standard cross-over operation where a random portion of an element genome $\mathbf{p}^i$ is taken from the genome of element e_i and complemented by a complementary partial genome $\mathbf{p}^j$ taken from element e_j, as shown in Fig. 7.2B. The genome of the offspring element produced in this way can be written as:

$$\mathbf{p}^{\text{new}} = \left\{\mathbf{p}_0^i, ..., \mathbf{p}_m^i, \mathbf{p}_{m+1}^j, ..., \mathbf{p}_n^j\right\}, \tag{7.3}$$

where m represents a randomly chosen index. Furthermore, we assigned a 0.2% chance to randomly mutate each value for $\mathbf{p}_k^{\text{new}}$ during the mixing operation. After many generations of elements, the fitness of the population was seen to improve greatly. In summary, within each generation 5% of the population was randomized, duplicate members were randomized, and each element had a 0.2% chance of mutation in order to reduce artificial convergence. Elitism was not used in this study, but is available in the provided code. However, since these methods are not guaranteed to converge to the best solution, I had

to define an acceptance criteria that could be applied to select a usable set of force field parameters.

7.2.4 Acceptance Criteria

When using GA optimization algorithms, it is important to remember that any perceived convergence can be misleading. The technique has not been mathematically proven to eventually find the best solution to the problem, and indeed it is possible that a sudden random mutation can greatly improve the fitness of an element within the population. This results in great difficulties when determining how many generations are needed before an acceptable set of results has been produced.

In the context of the methods discussed here, however, I was able to define an acceptance criteria as a replacement for the more commonly used convergence criteria. Since the model uses the CHARMM force field to represent interactions within the CDB molecules, the system already contains the difference between the DFT and CHARMM representations of the molecule. For the isolated CDB molecule in the minimized lowest energy configuration, I calculated the difference in forces produced by DFT and CHARMM, to be on the order of 5%. Since this comparison was made at the lowest energy configuration of the molecule, these forces are already close to 0.

If the average difference in force on the CDB molecule when it is adsorbed onto KCl(001) between my QM/MM simulations and the optimized force field is comparable, then it is reasonable to consider it to be fairly high quality. Since this average value includes comparisons performed at geometries other than the minimum energy configuration, it indicates whether or not the force field is able to provide a good description of the molecule-surface interactions between CDB and KCl for all geometries and positions of the molecule. For this study, I then set an acceptance criteria of 5% average error in forces when compared to QM/MM data.

7.3 Results

7.3.1 A Classical Force Field for CDB on KCl(001)

For each fitting model described in the methods section of this chapter, a population of $N = 1024$ elements was evolved over 1000 generations. Since GA relies heavily on randomness, the calculation has been repeated several times for each model. In my preliminary tests, I observed that small populations ($N = 256$ and $N = 512$) sometimes produce different results when evolved over the same number of generations. However, populations of 1024 or more elements were able to produce similar results when the calculation was repeated, due to a reduced susceptibility to artificial convergence.

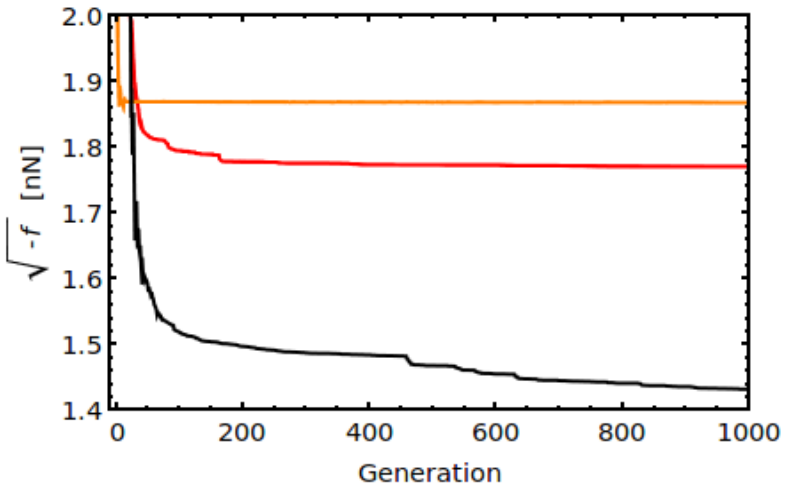

Figure 7.3: Evolution of LJA (red), LJM (orange), and Morse (black) models over 1000 GA generations.

Figure 7.3 plots the fitness of the best element in the population over 1000 generations for the LJA, LJM, and MRS models. The FT potential resulted in fitness values that were several orders of magnitude worse and was not evaluated further. Out of these three models the best fitness was achieved using the MRS model with a mean discrepancy of 1.41 nN. The LJA and LJM models produced slightly higher mean discrepancies of 1.8 nN and 1.9 nN respectively. LJM is the least flexible of these models, incorporating the fewest number of parameters and unsurprisingly results in the highest mean discrepancy. It is important to note, however, that all three of these models managed to successfully satisfy the acceptance

criteria that I defined in the previous section. This indicates that all of these models were expected to accurately reproduce *ab initio* molecule-surface interactions. Since the LJA and LJM models are technically the same functional form with varying degrees of freedom, I will only discuss the more flexible LJA model from this point onward.

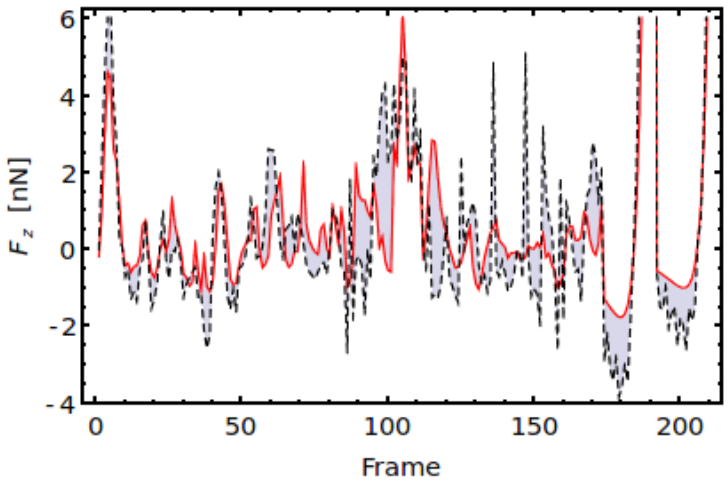

Figure 7.4: Comparison between DFT reference forces (black dashed) and ones obtained from the best fitted LJA model (solid red). Only the component normal to the surface plane is shown.

The difference between QM/MM simulations and the newly parametrized LJA force field can be illustrated by plotting forces on the CDB molecule in each frame included in the fitting database, as shown in Figure 7.4. Fairly significant differences can be observed throughout all the frames in this case, indicating that the error present within this model should be somewhat systematic. Furthermore, the increased discrepancies over the last 40 frames indicates that this error increases when the molecule-surface separation is larger or smaller than the equilibrium distance. This hints that the LJA model may inaccurately describe the overall strength of the molecule-surface interaction, which is primarily attributed to vdW effects in this system.

The MRS model showed improved fitness when compared to the LJA model, as shown in Figure 7.5. This model was able to accurately reproduce the first 80 training frames, from near-ground state QM/MM MD, as well as the final 40 frames. This indicated that the MRS model is able to more accurately represent the distance dependence of the molecule-

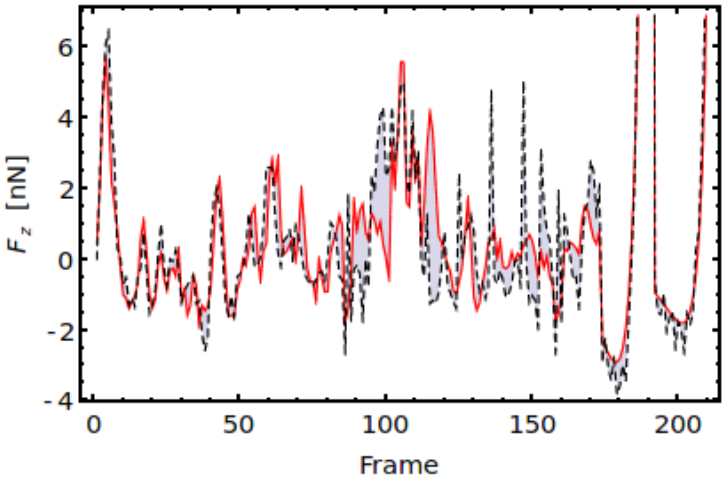

Figure 7.5: Comparison between DFT reference forces (black dashed) and ones obtained from the best fitted Morse model (solid red). Only the component normal to the surface plane is shown.

surface interactions.

As a final test, I evaluated these optimized force field models by testing how well they were able to reproduce several physical properties of the system. Since experimental measurements of CDB on KCl are not available, I used the adsorption energy and geometry of CDB molecules calculated in the previous chapter. Both the LJA and MRS models predicted the same lowest energy configuration of a single CDB molecule on KCl(001) as my previous DFT calculations. However, the adsorption energy previously estimated using DFT methods was 3.1 eV while LJA gave an adsorption energy of 2.6 eV and MRS gave an adsorption energy of 2.8 eV.

These results confirmed my previous suspicion that the MRS model more accurately reproduces the molecule-surface interaction. Since the MRS model satisfied my previously defined acceptance criteria and was the best candidate produced using these methods, I then used it to perform further simulations of the CDB molecule on KCl(001).

7.3.2 CDB Diffusion and Rotation

Using the optimized MRS force field, I was finally able to simulate some of the dynamic processes that occur when CDB molecules are deposited onto the KCl(001) surface. The

starting point that I chose for these studies was to examine the behaviour of CDB molecules on a clean KCl(001) surface. These calculations were performed by placing a CDB molecule above the KCl(001) surface with the plane of the molecule parallel to the surface and allowing the system to equilibrate for 10 ps. The simulations were performed using a 1 fs timestep and a 4 layer thick slab of KCl(001) to represent the surface. The bottom layer was fixed while the top 3 layers and all CDB atoms were allowed to relax. The behaviour of a single CDB molecule on KCl(001) was then observed for 10 ns at 300 K, 400 K, and 500 K using the NVE microcanonical ensemble. Each of these simulations was repeated a total of 10 times at each temperature.

The molecule was observed to be mobile at room temperature and could easily reorient itself with respect to the KCl(001) surface. This mobility can be characterized in two ways. The first is by considering how often the molecule may rotate. Within the scope of this evaluation, I defined rotation as a change in the angle between the line drawn through the two cations on the surface that the CN groups of the molecule were closest to and the [100] direction of the surface. Throughout these simulations, the CDB molecule was observed to undergo an average of 5 rotational motions at 300 K. At the same time, the central ring of the CDB molecule moved an average of 1 nm across the KCl(001) surface.

These results are in good agreement with experimental NCAFM images taken at room temperature where single CDB molecules cannot be resolved on clean KCl(001) terraces. The length of time needed to collect a NCAFM image is several orders of magnitude longer than that of molecular motion on the surface, making it impossible to image CDB molecules at room temperature. At 400 K, CDB molecules became predictably more mobile. Additionally, they were observed to occasionally roll or flip across the surface. Finally, at 500 K these effects were further pronounced, and in one rare instance the molecule became fully desorbed from the surface. In order to form the periodic defect-free porous networks described in Chapter 6, CDB molecules must first somehow become immobilized on the surface or form larger aggregates.

7.3.3 Adhesion to Step Edges

I then performed long time-scale simulations of many CDB molecules on the KCl(001) surface in order to gain insight into how nucleation may happen in this system. These calculations were performed using the MRS force field and a 4 layer slab representing the KCl(001) surface. The top three layers of KCl were allowed to relax along with all CDB atoms. The system was treated using the NVE microcanonical ensemble and contained a total of 49 CDB molecules on a large KCl(001) terrace which incorporated a step edge in the [100] direction. The starting point of this simulation can be seen in Figure 7.6A.

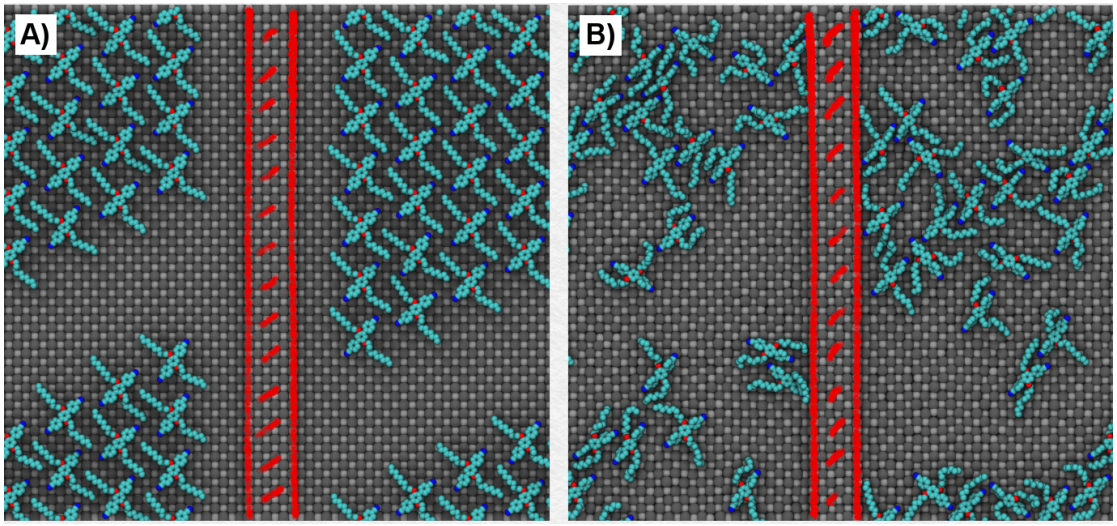

Figure 7.6: A) The starting point of a large MD simulation containing 49 CDB molecules on KCl(001). A step edge feature can be seen running down the center of the simulation cell. B) A snapshop of the MD simulation taken after 10 ns at 500 K. Some CDB molecules can be seen adhering to step edges, while others interact with each other in what resembles close-packed structures

After evolving this system for 20 ns at 500K, several CDB molecules could be observed at the step edge, as shown in Figure 7.6B. However, the other molecules exhibited very little motion during this time. Although the rate of diffusion observed for a single CDB molecule was sufficiently fast that it cannot be imaged with NCAFM, the motion of these molecules was still too slow for me to investigate growth directly using MD. Fortunately, these results still provide insight into the early stages of growth and nucleation.

Previous calculations and experimental data agree that isolated CDB molecules diffuse

rapidly across the KCl(001) surface. They must become immobilized on the surface in order to form the highly ordered films described in Chapter 6. The first possibility that I examined was the trapping of CDB molecules at step edges and kinks on the KCl(001) surface. I began by performing molecular dynamics simulations using the MRS force field of a single CDB molecule at a step edge feature on KCl(001).

Throughout 10 ps of equilibration and 20 ns of MD, the CDB molecule was observed to be stable at the step edge. Using the MD trajectory from these calculations, I then performed full DFT calculations in order to estimate the adsorption energy of a single CDB molecule at a [100] step edge on KCl(001). These DFT calculations were performed using the same methods described in Chapter 6 and represented the system as a 4 layer slab of KCl with a step edge rising one layer above the surface level. The lowest energy configuration of a CDB molecule at the step edge is shown in Figure 7.7.

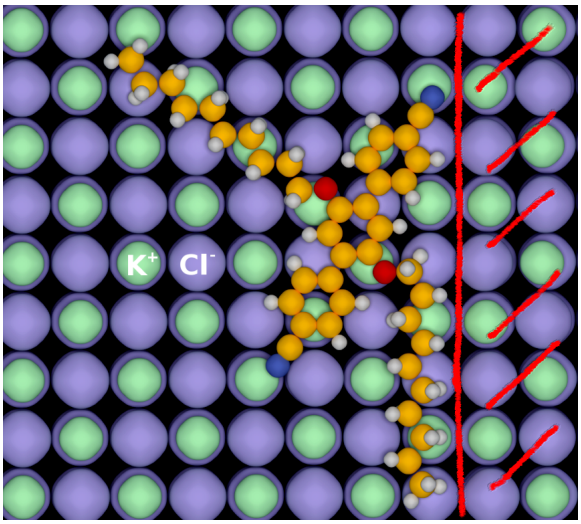

Figure 7.7: The optimized adsorption geometry for a single CDB molecule at a step edge on the KCl(001) surface. The CN anchoring group simultaneously interacts with two surface cations while the hydrocarbon chain adsorbs along the step edge itself.

When an isolated CDB molecule adsorbs at a step edge, the adsorption energy increases to 4.0 eV. This value was verified using both the QM/MM hybrid scheme and a full DFT setup. The large increase in adsorption energy in this configuration confirmed that a CDB molecule that finds a step edge on the surface at room temperature will spend a significant amount of time there before desorbing. The increased adsorption energy can

be attributed largely to two interactions. The first of these is that the CN group can simultaneously interact with two cation sites on the surface rather than just one. Secondly, the hydrocarbon chain can lie along the step edge and further increase adsorption energy *via* vdW interactions with the surface atoms. This result is consistent with experimental images that show decorated step edges when low coverages of CDB molecules are deposited at room temperature. After one CDB molecule has been stabilized at the step edge, it becomes increasingly favourable for additional molecules to adsorb there. The lowest energy configuration of a second captured molecule adsorbing adjacent to the first one along the step edge was calculated to be 4.2 eV. CDB molecules adsorbing next to the first one on the terrace, however, were predicted to have a much smaller increase in adsorption energy resulting in a final value of 3.3 eV.

When the CDB molecule adsorbs at a kink or corner the adsorption energy increases accordingly. At such sites, the CN group can interact with a total of 3 cation sites and it becomes possible for the second hydrocarbon chain to lie along a step edge as well. One such configuration is shown in Figure 7.8

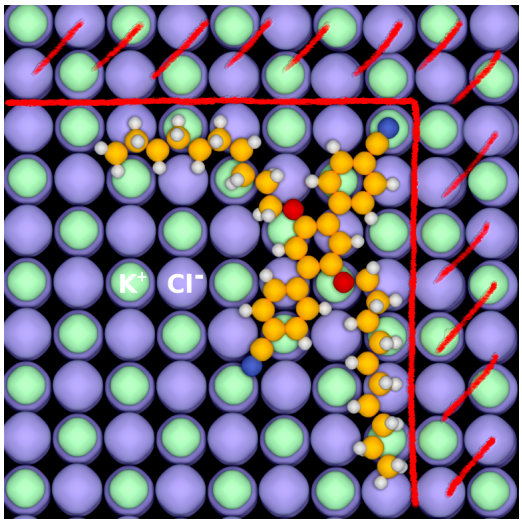

Figure 7.8: The optimized adsorption geometry for a single CDB molecule at a kink feature on the KCl(001) surface. The CN anchoring group simultaneously interacts with three surface cations while the two hydrocarbon chains lie along the step edges. These interactions contribute to greatly increase the adsorption energy of the molecule.

Full DFT calculations of a CDB molecule adsorbed to a kink feature on KCl(001)

estimate the adsorption energy to be 4.4 eV. These results show that molecules captured at kink features are even more stable than at step edges. These molecules were predicted to increase the adsorption energy of adjacent molecules along the step edge to 4.2 eV and ones on the clean terrace to 3.3 eV as well.

7.3.4 Structure Stability and Dewetting

While my MD simulations of CDB molecules on KCl(001) were not able to directly probe the growth process, they were able to provide some knowledge about the relative stability of CDB layer structures. To achieve this, I performed MD calculations using the MRS force field, a 4 layer slab representing the clean KCl(001) surface, and around 50 CDB molecules using the NVE microcanonical ensemble. The top three layers of KCl were allowed to relax along with all CDB atoms. The CDB molecules were arranged in several patterns on the surface and evolved for 10 ns at 300 K, 400 K, and 500 K. The starting velocities of these systems were chosen such that the desired temperature was produced after 10 ps of equilibration. The lowest energy monolayer structure shown in Figure 7.9A was found to be stable for the full 10 ns at 300 K, as seen in Figure 7.9B. In order to demonstrate that such stability is meaningful, it is useful to examine the behavior of a less stable film structure, such as the one shown in Figure 7.9C.

After 10 ns at 300 K, a snapshot of the close-packed system was taken, as shown in Figure 7.9D. While it is clear that the hydrocarbon arms are able to reorient themselves, the main bodies of the CDB molecules in the porous network configuration are still relatively stable within 10 ns of MD. Since the experimental images presented in Chapter 6 can only resolve the body of the molecule, as previously shown in Figure 6.7, rearrangements of the hydrocarbon chains or minor fluctuations in the film would not be noticeable. It is important to note that these simulations do not prove that the proposed structure is stable at room temperature and only highlight the relative instability of the close-packed structure shown in Figure 7.9 and the large difference in theoretical and experimental time-scales. At higher temperatures, however, both films became unstable and appeared to go

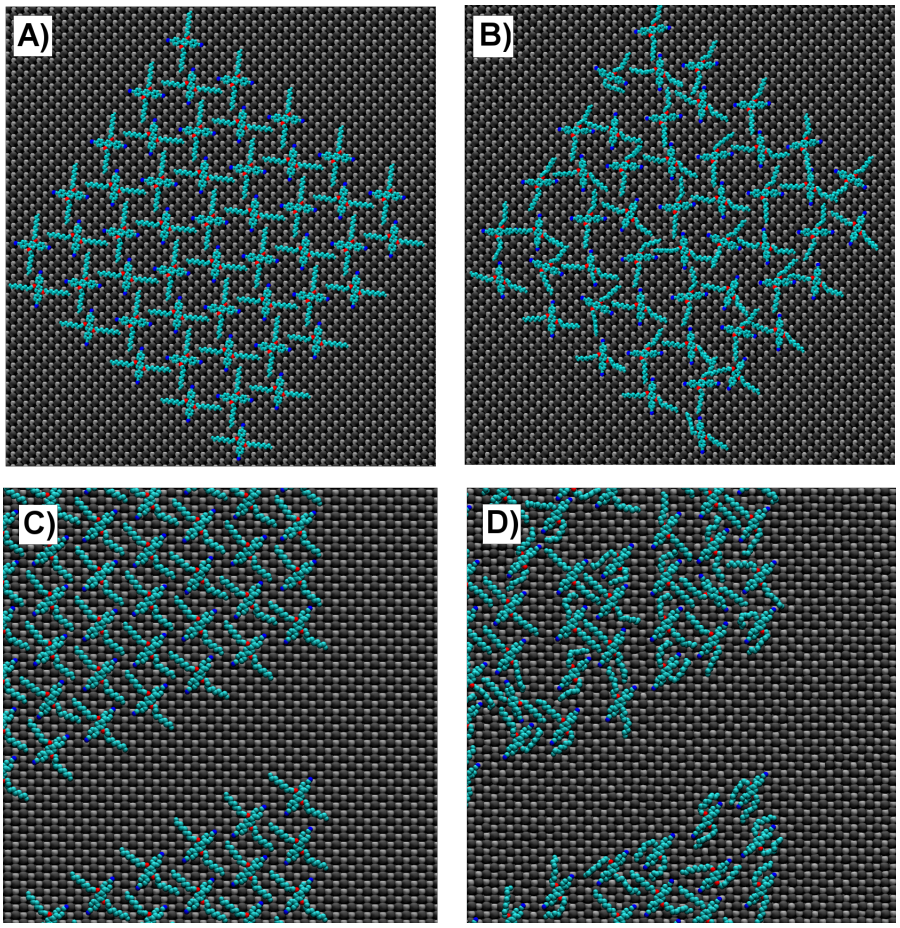

Figure 7.9: A) The starting configuration for 50 CDB molecules arranged in the previously calculated porous network. The surface is depicted in grey and black while the CDB molecules are shown in light blue with their CN groups (dark blue) and O atoms (red) highlighted. B) A snapshot of the porous network after 10 ns of MD at 300 K. The general structure has so far been preserved. C) The starting configuration for an array of 49 molecules arranged in a close-packed configuration on the KCl(001) surface. D) A snapshot of the system after 10 ns of MD at 300 K. A few of the CDB molecules have rotated on the surface.

through a dewetting process, during which large droplets composed of CDB molecules were observed, as shown in Figure 7.10.

All of the MD simulations that I performed at 500 K resulted in the dewetting of CDB molecules into large droplets within 10 ns regardless of starting configuration. At such high temperatures, there were no noticeable differences between simulations performed using various starting film geometries. These results indicate that the molecule-molecule interactions within this system are competitive with molecule-surface interactions. The previously observed film structures may actually be metastable states that arise due to

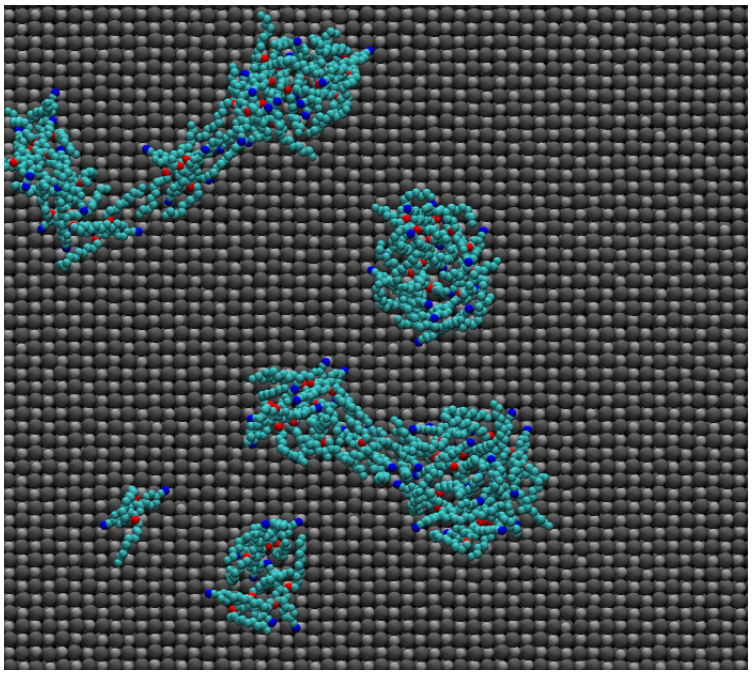

Figure 7.10: A representative snapshot of the system after 10 ns of MD at 500 K. The CDB molecules formed densely packed droplets on the surface. The surface is depicted in grey and black while the CDB molecules are shown in light blue. The CN groups are highlighted in dark blue and the O atoms are highlighted in red.

experimental deposition procedures rather than thermodynamically favored lowest energy configurations. It is important to remember, however, that the strength of the molecule-surface forces within my simulations are largely dependent on vdW interactions, which were represented using the semi-empirical DFT-D2 [176] method. Ideally, these interactions should be evaluated and verified using more accurate *ab initio* methods or experimental data. Unfortunately such data is currently unavailable for the KCl(001) surface.

7.4 Discussion and Conclusions

In this chapter, I developed a classical force field to model CDB molecules adsorbed onto the KCl(001) surface. The scheme that I used depends heavily on two critical techniques that I used to address the challenges of obtaining sufficient fitting data and optimizing a large parameter set. The QM/MM method allowed me to efficiently produce a large database of forces at various geometries using *ab initio* methods. This fitting library was

then used in conjunction with a GA based optimization scheme in order to obtain a number of molecule-surface force fields. Finally, I evaluated the obtained force fields and used the best one to study the dynamic properties of CDB molecules on KCl(001).

One of the biggest challenges when using a GA based optimization scheme is that it is not guaranteed to converge. Convergence is commonly defined by taking the RMS deviation between successive iterations. However, in the context of GA methods, this definition is conceptually lacking. The fitness of the best element within a population can remain constant for hundreds of generations before a random mutation appears and improves the population, as shown in Figure 7.3. There is no mathematical proof that the system will find a global minimum after a certain number of generations and the variational principle cannot be applied in a system where it is possible for mutations to both improve and reduce the fitness. However, despite these shortcomings, in our system it is reasonable to evaluate the average error in molecular forces, and use it to define an *acceptance* criteria instead. For the gas phase CDB molecule, CHARMM interactions (not parametrized) already give a 5% error in forces when compared to our DFT calculations. Each GA parametrized model that gives a comparable error is of acceptable quality. In the studies that I have performed, the force fields produced using GA methods were able to reach this level of accuracy within roughly 1000 generations.

Another important issue that I encountered was ensuring that the training set was complete. Simply taking a number of atomic configurations and corresponding forces from a MD trajectory was not sufficient to sample all of the possible interatomic interactions. Since the CDB molecule was almost always found in a stable equilibrium position, the initial model was *overtrained* to reproduce that one particular state. The force field was artificially driven towards unphysically strong interactions between certain atom types in order to reproduce the DFT-MD forces. However, the algorithm did not know that such strong interactions would result in instabilities when CDB atoms moved closer to the KCl(001) surface. Additional, unlikely configurations in the repulsive regime of molecule-surface interactions were included to probe these interactions and the models produced

were found to be stable over 10 ns MD simulations. The final MRS force field obtained was able to accurately reproduce DFT forces on molecular atoms and an adsorption energy of 2.8 eV in comparison to a DFT value of 3.1 eV.

These force fields were then used to simulate single CDB molecules on the clean KCl(001) terrace and study molecular diffusion and rotation. The results indicated that the molecules exhibit rapid rotational and translational motion on the surface at a rate that should make it impossible for NCAFM experiments to image them at room temperature. These fast moving molecules must be captured at surface features or form larger networks before they can be observed. Simulations containing many CDB molecules showed that nucleation may originate at step edges and kinks where an increase in adsorption energy was then confirmed using *ab initio* methods. Finally, my results showed that the previously proposed lowest energy film structure was more stable than a close-packed arrangement of molecules at 300 K and predicted the dewetting of CDB molecules at 500 K. These results are all consistent with the experimental data that indicates that depositing low concentrations of CDB molecules onto KCl(001) leads to decorated step edges and clean terraces. Unfortunately, my MD simulations were still unable to probe a sufficiently long time-scale to study the entire growth process.

In summary, in this study I have developed an efficient scheme for fitting molecule-surface force fields by combining a QM/MM embedding techniques with GA methods. This scheme avoids the need to approximate large organic molecules using a collection of smaller fragments and allowed me to optimize all the parameters within the system simultaneously. The force field produced using these methods was then used to study the mobility of single CDB molecules and propose an initial step in the growth of experimentally observed network structures.

Chapter 8

Conclusion of Thesis

I performed multi-scale studies of the properties of organic molecules and films on bulk insulating surfaces. My approach partitioned the problem into several components and incorporated them into a multi-scale model of the system. I studied molecule-surface interactions to build realistic atomistic models of the adsorbed system and combined these results with molecule-molecule interactions to predict the morphology of structures formed *via* deposition and growth. These theoretical predictions were then used in conjunction with a point dipole model and VAFM code to produce data that can be directly compared to experimental results. This allowed me to both verify my methods and propose mechanisms and explanations for experimentally observed phenomena.

I began by studying the transient mobility of deposited atoms or molecules on an insulating surface. Molecular dynamics simulations designed to mimic experimental deposition predicted that a large percentage of Pd atoms arriving on a MgO(001) surface are transiently mobile at temperatures as low as 5 K. This mobility was shown to be mainly dependent on scattering or deflection near repulsive Mg sites on the surface rather than energy gained during the adsorption process. The angle of deposition and incident energy of the Pd atom were both shown to significantly enhance transient mobility.

Next I investigated single Co-Salen molecules on the NaCl(001) and NiO(001) surfaces. Combining theoretical predictions with experimental images in this system allowed me to

determine the adsorption site of Co-Salen on NiO(001) and provide an explanation for the differences observed in comparison to a previous study of Co-Salen on NaCl(001) [3]. Slight changes in commensurability between these systems resulted in qualitative differences in film structure and growth modes on two bulk insulators with the same simple cubic crystal structure. These results emphasized the benefits of combining theoretical predictions with experimental images, however, a direct comparison between theory and experiment had not been achieved.

In order to progress towards a direct comparison between theory and experiment, I explored the NCAFM imaging mechanism and the properties of the Cr coated NCAFM tips used. DFT calculations were used to develop a model of the tip and generate tip-sample force fields which could be used in conjunction with a VAFM code. The most stable atomic configuration of the tip apex was a pyramid with a large dipole moment at the tip apex. This dipole moment was represented using a point dipole model, greatly reducing the complexity of generating VAFM force fields and interpreting experimental data. The point dipole model was then used to extrapolate the magnitude and orientation of the dipole moment at a real Cr coated NCAFM tip apex directly from experimental scan-lines. It was then tested by studying CO molecules on NiO(001) and shown to produce scan-lines that were in quantitative agreement with experimental results.

After developing my understanding of NCAFM imaging mechanisms, I focused my attention on how competing molecule-molecule and molecule-surface interactions can be used to influence the morphology of deposited films. I characterized the molecule-molecule and molecule-surface interactions present when CDB molecules were deposited onto KCl(001) in order to propose atomistic models of stable monolayer structures. These configurations were then used to generate VAFM images using the point dipole model and directly compared to experimental images. Furthermore, my results on the relative strengths of the competing interactions within the system were consistent with experimentally observed differences in the film structures of modified CDB molecules.

Finally, in order to progress beyond a static view of these systems, I parametrized a

classical force field for CDB molecules on KCl(001) to study their dynamic properties. I developed an efficient parametrization scheme that took advantage of QM/MM techniques to generate fitting data and GA methods to simultaneously optimize a large set of parameters. These classical potentials allowed me to substantially increase the size and time scales of my simulations to study the diffusion of CDB molecules. My results indicated that single molecules should move rapidly across the KCl(001) surface until they are eventually captured at a step edge or kink. The increased adsorption energy at these surface sites make them likely candidates for the initial stages of growth and nucleation. Due to the amount of time that it takes to image the surface with NCAFM, these mobile molecules are not visible until they are immobilized.

8.1 Future Developments

While the techniques and results discussed in this work will be helpful in future interpretation of experimental NCAFM data and the design of novel molecular structures on insulating surfaces, it would be useful to extend this study in several ways.

1. VdW interactions contribute substantially to the adsorption energy of many organic molecules on insulating surfaces, as predicted for Co-Salen and CDB molecules throughout this thesis. However, since these interactions are not well represented in standard DFT methods, they are often accounted for using semi-empirical corrections or vdW functionals. While experimental values and higher accuracy theoretical predictions are occasionally available, a reliable estimate of such energies on alkali halide surfaces is not currently available in the literature. Results that could validate these popular semi-empirical correction schemes on these materials would be of great value in the future.

2. Classical potentials allowed me to greatly increase the size and time scale of my simulations, however, they were still insufficient to directly model the growth process of CDB molecules on KCl(001). While methods such as Monte Carlo simulations may

be able to solve such problems in some systems, they are difficult to implement for the CDB molecule due to its many degrees of freedom. Further method development is still needed to extend simulation time-scale so that slow processes such as nucleation and growth may be addressed.

These studies provide a substantial amount of knowledge about the adsorption, diffusion, and film structure of organic molecules on insulating surfaces. In particular, they highlight the importance of considering both the kinetic and thermodynamic properties of the system and the importance of carefully balancing molecule-molecule and molecule-surface interactions. The methods developed throughout this work will help in the interpretation and analysis of future experimental measurements of molecules on insulating surfaces and the knowledge gained will be useful when tailoring the properties of functional molecular films in the future.

Appendix A

Information Supplementary to Chapter 2

Energy Level	ADMM Method	Full DFT	Difference (Ha)	Difference (eV)
LUMO 1	-0.0891609	-0.0907906	0.00163	0.0444
LUMO 2	-0.0196702	-0.0201723	0.00050	0.0136
LUMO 3	0.0016591	0.0008286	0.00083	0.0226
LUMO 4	0.0311522	0.0317138	-0.00056	-0.0152
LUMO 5	0.0544461	0.0537445	0.00070	0.0190
LUMO 6	0.0824156	0.0823380	0.00008	0.0022
LUMO 7	0.1229759	0.1227551	0.00022	0.0060
LUMO 8	0.1385413	0.1384986	0.00004	0.0011
LUMO 9	0.1768859	0.1760883	0.00080	0.0218
LUMO 10	0.1827329	0.1819730	0.00076	0.0207

Table A.1: A table containing 10 LUMO levels of the $C_4H_6NiO_4$ evaluation molecule calculated using the CP2K code. The energy values for these levels are given in Ha and results using the ADMM method and the full DFT treatment are compared. The difference between levels are on the order of 0.01-0.05 eV.

Appendix B

Information Supplementary to Chapter 3

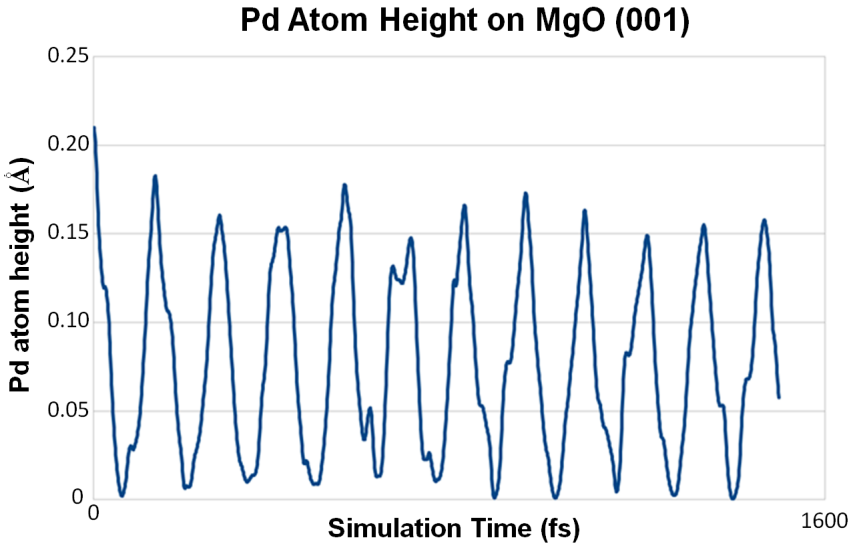

Figure B.1: The height of a Pd atom adsorbed on MgO (001) as a function of simulation time is shown. The average frequency of oscillation was calculated to be 2.2 x 10^{12} s^{-1} over 10 ns of equilibrated trajectory.

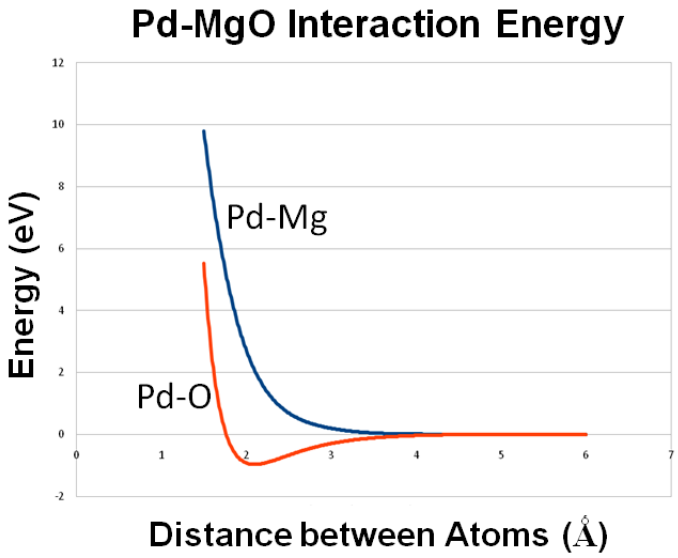

Figure B.2: The interaction energy between a Pd atom and MgO surface atoms is shown as a function of distance. Pd-O interactions are shown in red while Pd-Mg interactions are shown in blue. In both cases the interactions approach zero at distances larger than 4 Å.

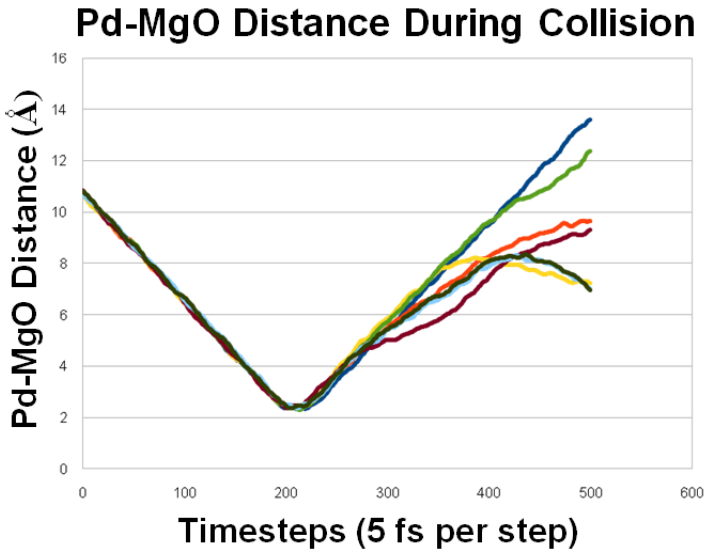

Figure B.3: The minimum distance between the Pd atom and a surface atom during the initial collision. 10 trajectories of a Pd atom colliding with the MgO (001) surface are shown. In all cases the incoming atoms were assigned 0.4 eV of incident energy and were observed to remain within the interaction regime for 100 timesteps. Incoming atoms with higher incident energy are expected to interact with the initial collision site for shorter periods of time while incoming atoms with lower incident energy are expected to interact for longer periods of time.

Appendix C

Information Supplementary to Chapter 4

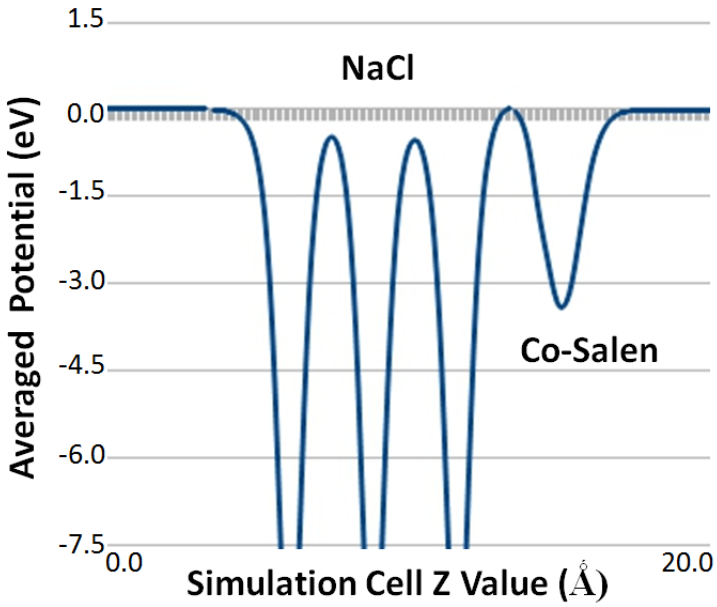

Figure C.1: The average electrostatic potential of the system in the xy plane is plotted from one side of the simulation cell to the other. The Co-Salen decorated NaCl (001) surface is represented in blue. In contrast to Co-Salen on NiO (001) (see Figure 4.8), there is no change in the vacuum level on either side of the cell.

Appendix D

Information Supplementary to Chapter 5

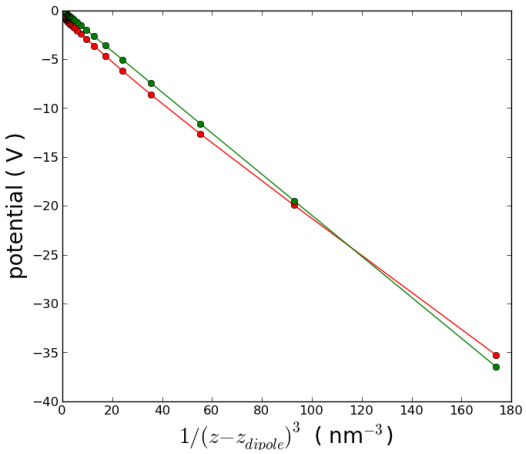

Figure D.1: A plot of the electrostatic potential with respect to distance away from the nano-tip apex. A 5 D point dipole positioned at the atomic coordinates of the apex atom is unable to reproduce the local electrostatic potential obtained from DFT calculations.

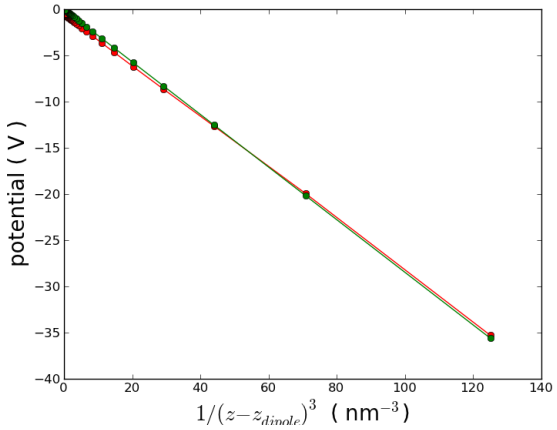

Figure D.2: A plot of the electrostatic potential with respect to distance away from the nano-tip apex. Even a 9.5 D point dipole can produce the local electrostatic potential obtained from DFT calculations if it can be positioned anywhere within the nano-tip. However, such a nano-tip is too large and incompatible with the rest of the model.

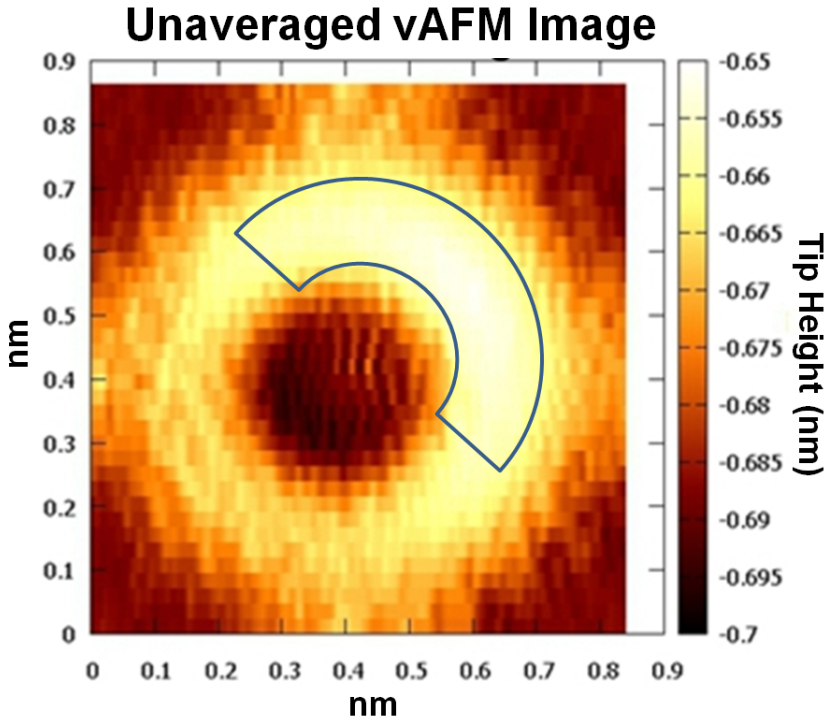

Figure D.3: A vAFM image of CO on NiO (001) generated using a single unaveraged geometry. The tilted geometry of the CO molecule results in the bright edge outlined in blue. This image was produced using the experimental parameters of f_0 = 190.444039 kHz, c = 151±21 N/m, A_0 = 1.0±0.1 nm, Q = 175903, Δf = -48 Hz. The theoretical long-range forces were fit to experimental data and the tip was represented as a 7 D point dipole 0.6 nm below the macro-tip.

Appendix E

List of Example Files on Disk

- **Chapter 2: Theoretical Methods**
  - Auxiliary Basis Set Parametrization Example Files
  - QM/MM CP2K Example Files
- **Chapter 3: Transient Mobility**
  - Pd on MgO GULP Example Files
  - Pd on MgO SciFi Example Files
- **Chapter 4: Adsorption and Mobility of Single Molecules**
  - Co-Salen on NaCl CP2K Example Files
  - Co-Salen on NiO CP2K Example Files
  - Dipole Moment Analysis Script
- **Chapter 5: Atomic Force Microscopy with Metallic Tips**
  - CO on NiO CP2K Example Files
  - Cr Asperity CP2K Example Files
  - Dipole Moment Analysis Script

  - VAFM Force Field Maker Python Script
  - Hamaker Constant Estimator
  - VAFM Code
  - VAFM Example Files

- **Chapter 6: Competing Interactions on the Surface**
  - CDB on KCl CP2K Example Files

- **Chapter 7: Dynamic Effects on the Surface**
  - CDB on KCl Molecular Dynamnics LAMMPS Example Files
  - Genetic Algorithm Code

Bibliography

[1] G. Bhalla, M. H. Tsang, D. Gao, Q. Chen, W. Ruhe, and N. Ushioda. *SAE International*, 5:496–503, 2012.

[2] A. M. Barnes, K. D. Bartle, and V. R. A. Thibon. *Tribol. Int.*, 34:389–395, 2001.

[3] K. Lämmle, T. Trevethan, A. Schwarz, M. Watkins, A. Shluger, and R. Wiesendanger. *Nano Lett.*, 10:2965–2971, 2010.

[4] A. Leach. *Molecular Modelling: Principles and Applications*. Prentice Hall, New Jersey, USA, 2001.

[5] J. P. Perdew, K. Burke, and M. Ernzerhof. *Phys. Rev. Lett.*, 77:3865–3868, 1996.

[6] M. Ernzerhof and J. P. Purdew. *J. Chem. Phys.*, 109:3313–3320, 1998.

[7] A. D. Becke. *J. Chem. Phys.*, 98:5648–5652, 1993.

[8] P. J. Stephens, F. J. Devlin, C. F. Chabalowsky, and M. J. Frisch. *J. Phys. Chem.*, 98:11623–11627, 1994.

[9] T. Laino, F. Mohamed, A. Laio, and M. Parrinello. *J. Chem. Theory Comput.*, 1:1176–1184, 2005.

[10] T. Laino, F. Mohamed, A. Laio, and M. Parrinello. *J. Chem. Theory Comput.*, 2:2178–2189, 2006.

[11] M.C. Payne, M.P. Teter, D.C. Allen, T.A. Arias, and J.D. Joannopoulos. *Rev. Mod. Phys.*, 64:1045, 1992.

[12] G. Henkelman and H. Jonsson. *J. Chem. Phys.*, 111:7010, 1999.

[13] G. Lippert, J. Hutter, and M. Parrinello. *M. Mol. Phys.*, 92:477–487, 1997.

[14] T. H. Dunning. *J. Chem. Phys.*, 90:1007, 1989.

[15] H. B. Jansen and P. Ros. *Chem. Phys. Lett.*, 3:140, 1969.

[16] B. Liu and A. D. McLean. *J. Chem. Phys.*, 59:4557, 1973.

[17] M. Guidon, J. Hutter, and J. VandeVondele. *J. Chem. Theory Comput.*, 6:2348–2364, 2010.

[18] S. Goedecker, M. Teter, and J. Hutter. *Phys. Rev. B*, 54:1703, 1996.

[19] J. VandeVondele and J. Hutter. *J. Chem. Phys.*, 127:114105–1–9, 2007.

[20] S. Grimme. *J. Comput. Chem*, 27:1787–1799, 2006.

[21] A. Warshel and M. Levitt. *J. Mol. Biol.*, 103:227–249, 1976.

[22] U.C. Singh and P.A. Kollman. *J. Comput. Chem.*, 7:718–730, 1986.

[23] M.J. Field, P.A. Bash, and M. Karplus. *J. Comput. Chem.*, 11:700–733, 1990.

[24] F. Maseras and K. Morokuma. *J. Comput. Chem.*, 16:1170–1179, 1995.

[25] A. Crespo, D.A. Sherlis, M.A. Marti, P. Ordejon, A.E. Roitberg, and D.A. Estrin. *J. Phys. Chem. B*, 107:13728–13736, 2003.

[26] M.A. Thompson. *J. Phys. Chem.*, 99:4794–4804, 1995.

[27] D.A. Yarne, M. E. Tuckerman, and G. J. Martyna. *J. Chem. Phys.*, 115:3531–3539, 2001.

[28] A. Laio, J. VandeVondele, and U. Rothlisberger. *J. Chem. Phys.*, 116:9641–6947, 2002.

[29] K. Nam, J. Gao, and D.M. York. *J. Chem. Th. Comput.*, 103:3462–3471, 1999.

[30] M. Sushko, UI.A. Abarenkov P. Sushko, and A.L Shluger. *J. Comput. Chem.*, 31:2955–2966, 2010.

[31] D. Das, P.L. Eurenius, E.M. Billings, P. Sherwood, C.D. Chatfield, M. Hodoscek, and B.R. Brooks. *J. Chem. Phys.*, 117:10534–10547, 2002.

[32] P. Amara and M.J. Field. *Theor. Chem. Acc.*, 109:43–52, 2003.

[33] C. R. A. Catlow, K. M. Diller, and M.J. Norgett. *J. Phys. C: Solid State Phys.*, 10:1395–1412, 1977.

[34] C.S. Praveen, A. Kokalj, and M. Valant. *Comp. Mater. Sci.*, 50:2628–2635, 2011.

[35] D. M. Roessler and W. C. Walker. *Phys. Rev.*, 166:599, 1968.

[36] J. Vogt and H. Weiss. *Surf. Sci.*, 491:155–168, 2001.

[37] D. Berger, A.J. Logsdail, H. Oberhofer, M.R. Farrow, C.R.A. Catlow, P. Sherwood, A.A. Sokol, V. Blum, and K. Reuter. *J. Chem. Phys.*, 141:024105, 2014.

[38] B.J. Alder and T.E. Wainwright. *J. Chem. Phys.*, 31:459, 1959.

[39] A. Rahman. *Phys. Rev.*, 136:A405–A411, 1964.

[40] M.A. Gonzalez. *Collection SFN*, 12:169–200, 2011.

[41] J.I. Choe and B. Kim. *Bull. Korean Chem. Soc.*, 4:419–424, 2000.

[42] N. Galamba and C.A. Nieto de Castro. *J. Chem. Phys.*, 120:8676–8681, 2004.

[43] L. Verlet. *Phys. Rev.*, 159:98–103, 1967.

[44] P.H. Hunenberger. *Adv. Polymer. Sci.*, 173:105–149, 2005.

[45] D. J. Auerbach. *Science*, 294:2488–2489, 2001.

[46] J. A. Venables. *Introduction to Surface and Thin Film Processes*. Cambridge University, Cambridge, England, 2000.

[47] I. Yamada, H Inokawa, and T. J. Takagi. *J. Appl. Phys.*, 56:2746, 1985.

[48] S. Rousset, S. Chiang, D. E. Fowler, and D. D. Chambliss. *Phys. Rev. Lett.*, 69:3200, 1992.

[49] S. Rousset, S. Chiang, D. E. Fowler, and D. D. Chambliss. *Surf. Sci.*, 287/288:941, 1993.

[50] C. R. Henry. *Surf. Sci. Rep.*, 31:231, 1998.

[51] H. Graoui, S. Giorgia, and C. R. Henry. *Surf. Sci.*, 417:350, 1998.

[52] H. Graoui, S. Giorgio, and C. R. Henry. *Phil. Mag.*, 81:1649, 2001.

[53] C. R. Henry, C. Chapon, C. Duriez, and S. Giorgio. *Surf. Sci.*, 253:177–189, 1991.

[54] C. Goyhenex, M. Meunier, and C. R. Henry. *Surf. Sci.*, 350:103–112, 1996.

[55] C. Duriez, C. Chapon, C. R. Henry, and J. M. Rickard. *Surf. Sci.*, 230:123–136, 1990.

[56] G. Haas, A. Menck, H. Brune, J. V. Barth, J. A. Venables, and K. Kern. *Phys. Rev. B*, 61:11105–11108, 2000.

[57] L. Xu, G. Henkelman, C. T. Campbell, and H. Jonsson. *Phys. Rev. Lett.*, 95:146103, 2005.

[58] L. Xu, G. Henkelman, C. T. Campbell, and H. Jonsson. *Surf. Sci.*, 600:1351, 2006.

[59] G. Bacaro, A. Fortunelli, F. Nita, and R. Ferrando. *Phys. Rev. Lett.*, 95:246103, 2005.

[60] I. V. Yudanovv, S. Vent, K. Neyman, G. Pacchioni, and N. Rosch. *Chem, Phys. Lett.*, 275:245, 1997.

[61] W. Vervisch, C. Mottet, and J. Goniakowski. *Phys. Rev. B*, 65:245411, 2002.

[62] W. Vervisch, C. Mottet, and J. Goniakowski. *Eur. Phys. J. D*, 24:311, 2003.

[63] Y. Long and N. X. Chen. *Physica B*, 403:4006–4011, 2008.

[64] K. McKenna, T. Trevethan, and A. Shluger. *Phys. Rev. B*, 82:085271–085276, 2010.

[65] I. Ostadal, P. Kocan, J. Myslivecek, and P. Sobotik. *Czech J. Phys.*, 53:41–48, 2003.

[66] M Sterrer, T. Risse, M. Heyde, H-P. Rust, and H-J. Freund. *Phys. Rev. Lett.*, 98:206103, 2007.

[67] W. F. Egelhoff and I. Jacob. *Phys. Rev. Lett.*, 62:921, 1989.

[68] D. K. Flynn, J. W. Evans, and J. A. Thiel. *J. Vac. Sci. A*, 7:235412, 1989.

[69] E. Vasco, C. Polop, and E. Rodriguez. *Phys. Rev. B*, 67:235412, 2003.

[70] J. Myslivecek, P. Sobotik, I. Ostadal, and T. Jarolimek. *Phys. Rev. B*, 63:045403, 2001.

[71] J. W. Evans. *Vacuum*, 41:479, 1990.

[72] J. W. Evans, D. E. Sanders, P. A. Thiel, and A. E. DePristo. *Phys. Rev. B*, 41:5410, 1990.

[73] D. E. Sanders and A. E. DePristo. *Surf. Sci.*, 254:341–353, 1991.

[74] S. Clarke, M. R. Wilby, D. D. Vvedenskey, T. Kawamura, and T. Sakamoto. *Appl. Phys. Lett.*, 54:2417, 1989.

[75] B. Heinrich, J. F. Cochran, A. S. Arrott, S. T. Purcell, K. B. Urquhart, J. R. Dutcher, and W. F. Egelhoff. *Appl. Phys. A*, 49:473, 1989.

[76] S. Clarke, M. R. Wilby, D. D. Vvedenskey, and T. Kawamura. *Phys. Rev. B*, 40:1369, 1990.

[77] A. Samsavar, E. S. Hirschorn, F. M. Leibsle, and T. C. Chiang. *Phys. Rev. Lett.*, 63:2830, 1989.

[78] D. D. Chambliss and R. J. Wilson. *Vac. Sci. Technol. B*, 9:928–932, 1991.

[79] R. D. Young and D.C. Schubert. *J. Chem. Phys.*, 42:3943, 1965.

[80] G. L. Kellogg. *Phys. Rev. Lett.*, 76:98–101, 1996.

[81] P. S. Weiss and D. M. Eigler. *Phys. Rev. Lett.*, 69:2240, 1992.

[82] S. C. Wang and G. Ehrlich. *J. Chem. Phys.*, 94:4071, 1991.

[83] S. C. Wang and G. Ehrlich. *Phys. Rev. Lett.*, 71:4174–4177, 1993.

[84] M. Schneider, A. Rahman, and I. K. Schuller. *Phys. Rev. Lett.*, 55:604–606, 1985.

[85] G. DeLorenzi and G. Ehrlich. *Surf. Sci.*, 293:900–907, 1993.

[86] A. Beniya, K. Mukai, Y. Yamashita, and J. Yoshinobu. *J. Chem. Phys.*, 126:141102, 2007.

[87] J. Yoshinobu, N. Tsukahara, F. Yasui, K Mukai, and Y. Yamashita. *Phys. Rev. Lett.*, 90:248301–248304, 2003.

[88] J. V. Barth. *Surf. Sci. Rep.*, 40:75, 2000.

[89] J. V. Barth, T. Zambelli, J. Wintterlin, and G. Ertl. *Chem. Phy. Lett.*, 270:152, 1997.

[90] J. Harris and B. Kaesmo. *Surf. Sci.*, 105:L281, 1981.

[91] C. Felix, G. Vandoni, W. Harbich, J. Buttet, and R. Monot. *Phys. Rev. B*, 54:17039, 1996.

[92] Y. Yue, Y. K. Ho, and Z. Y. Pan. *Phys. Rev. B*, 57:6685, 1998.

[93] S.-G. Lee and Y.-C. Chung. *Vac. Sci. Technol.*, 26:1392, 2008.

[94] Y. Zeiri and R. R. Lucchese. *J. Chem. Phys.*, 94:4055=4061, 1991.

[95] I. L. Singer. *Vac. Sci. Technol.*, 12:2605–2616, 1994.

[96] J. Noguiera, S. A. Vazquez, O. A. Mazyar, W. L. Hase, B. G. Perkins, D. J. Nesbitt, and E. Martinez-Nunez. *J. Phys. Chem.*, 113:3850–3865, 2009.

[97] E. Pollak. *J. Phys. Chem.*, 115:7189–7198, 2001.

[98] Y. Peng, L. Liu, Z. Cao, S. Li, O. A. Mazyar, W. L. Hase, and Y. Yan. *J. Phys. Chem. C*, 112:20340 – 20346, 2008.

[99] G. Fan and J. R. Manson. *Phys. Rev. B*, 79:79, 2009.

[100] U. Tasic, B. Scott Day, T. Yan, J. R. Morris, and W. L. Hase. *J. Phys. Chem. C*, 112:476–490, 2008.

[101] T. Yan, N. Isa, K. D. Gibson, S. J. Sibender, and W. L. Hase. *J. Phys. Chem. A*, 107:10600–10607, 2003.

[102] J. W. Lu, W. A. Alexander, and J. R. Morris. *Phys. Chem. Chem. Phys.*, 12:12533–12543, 2010.

[103] J. R. Manson. *Phys. Rev. B*, 58:2253=2258, 1998.

[104] M. E. Saecker, S. T. Govoni, D. V. Kowalski, M. E. King, and G. M. Nathanson. *Science*, 252:1421–1424, 1991.

[105] J. C. Tully. *Annu. Rev. Phys. Chem.*, 51:153–178, 2000.

[106] G. Antczak and G. Ehrlich. *Surf. Sci. Rep.*, 62:39–61, 2007.

[107] B. Taylor and I. Langmuir. *Phys. Rev.*, 44:423, 1993.

[108] D. W. Bassett and P. R. Webber. *Surf. Sci.*, 70:520, 1978.

[109] G. DeLorenzi and G. Jacucci. *Surf. Sci.*, 164:526, 1985.

[110] G. L. Kellogg and P. J. Feibelman. *Phys. Rev. Lett.*, 64:3143, 1990.

[111] C. Chen and T. T. Tsong. *Phys. Rev. Lett.*, 64:3147, 1990.

[112] G. L. Kellogg. *Surf. Sci.*, 246:31, 1991.

[113] G. L. Kellogg, A. F. Wright, and M. S. Daw. *J. Vac. Sci. Technol.*, 9:1757, 1991.

[114] T. T. Tsong and C. Chen. *Nature*, 335:328, 1992.

[115] G. L. Kellogg. *Surf. Sci.*, 226:18, 1992.

[116] A. Friedl, O. Schultz, and K. Muller. *Surf. Sci.*, 226:24, 1992.

[117] T.-Y. Fu and T. T. Tsong. *Surf. Sci.*, 421:157, 1999.

[118] J. C. Tully, G. H. Gilmer, and M. Shugard. *J. Chem. Phys.*, 71:1630, 1979.

[119] G. DeLorenzi, G. Jacucci, and V. Pontikis. *Surf. Sci.*, 116:391, 1982.

[120] J. D. Gale and A. L. Rohl. *Mol. Simul.*, 29:291, 2003.

[121] L. Kantorovich, T. Trevethan, and A. Foster. Self-consistent image force interaction code, 2009.

[122] E. Kolodney, A. Amirav, R. Elber, and R. B. Gerber. *Chem. Phys. Lett.*, 113:303–306, 1985.

[123] B. G. Dick Jr. and A. W. Overhauser. *Phys. Rev.*, 112:90, 1958.

[124] O. Robach, G. Renaud, and A. Barbier. *Surf. Sci.*, 401:227–235, 1998.

[125] G. Renaud and A. Barbier. *Surf. Sci.*, 142:433–435, 142.

[126] G. Renaud, A. Barbier, and O. Robach. *Phys. Rev. B*, 60:5972, 1999.

[127] G. Henkelman and H. Jonsson. *J. Chem. Phys.*, 113:9978–9985, 2000.

[128] D. Toton, C. D. Lorenz, N. Rompotis, N. Martsinovich, and L. Kantorovich. *J. Phys. Condens. Matter*, 22:074205, 2010.

[129] T. Trevethan. *PhD. Dissertation.* PhD thesis, Kings College London, 2006.

[130] S. Andersson, L. Wilzen, M. Persson, and J. Harris. *Phys. Rev. B*, 40:8146–8148, 1989.

[131] G. Armand and J. R. Manson. *Phys. Rev. B*, 43:14371–14377, 1991.

[132] A. V. A. Kumar, H. Jobic, and S. K. Bhatia. *J. Phys. Chem. B*, 110:16666–16671, 2006.

[133] G. Fan and J. R. Manson. *Phys. Rev. Lett.*, 101:063202, 2008.

[134] R. W. Zwanzig. *J. Chem. Phys.*, 32:1173, 1960.

[135] B. MacCarroll and G. Ehrlich. *J. Chem. Phys.*, 38:523, 1963.

[136] A. Plyukhim and J. Schofield. *Phys. Rev. E*, 65:026603, 2002.

[137] F. O. Goodman. *Prog. Surf. Sci.*, 5:261, 1974.

[138] G. N. Vayssilov. *Adv. Colloid Interface Sci.*, 57:123–159, 1995.

[139] A. L. Shluger, R. T. Williams, and A. L. Rohl. *Surf. Sci.*, 343:273–287, 1995.

[140] S. Kawai, T. Glatzel, S. Koch, A. Baratoff, and E. Meyer. *Phys. Rev. B*, 83:035421, 2011.

[141] G. Bertotti. *Hysteresis in magnetism: For physicists, material scientists, and engineers.* Gulf Professional Publishing, 1998.

[142] G. Antxzak and G. Ehrlich. *J. Colloid Interface Sci.*, 276:1–5, 2004.

[143] D. C. Senft and G. Ehrlich. *Phys. Rev. Lett.*, 74:294, 1995.

[144] R. Ferrando and A. Fortunelli. *J. Phys. Condens. Matter*, 21:264001, 2009.

[145] T. Ala-Nissila, R. Ferrando, and S. C. Ying. *Adv. Phys.*, 51:3:949–1078, 2002.

[146] R. Ferrando, R. Spadacini, and G. E. Tommei. *Phys. Rev. E*, 51:126, 1995.

[147] O. M. Braun and R. Ferrando. *Phys. Rev. E*, 65:061107, 2002.

[148] J. Ferron. *Phys. Rev. B*, 79:245407, 2009.

[149] D. C. Senft. *Appl. Surf. Sci.*, 94-95:231, 1996.

[150] L. Prandtl. *J. App. Math. Mech.*, 8:85–106, 1928.

[151] L. Jansen, H. Holscher, H. Fuchs, and A. Schirmeisen. *Phys. Rev. Lett.*, 104:256101, 2010.

[152] L. Venkatamaraman, J.E. Klare, I.W. Tam, C. Nuckolls, M.S. Hybertsen, and M.L. Steigerwald. *Nano Lett.*, 6:458–462, 2006.

[153] J. R. Heath. *Rev. Matter Res.*, 39:30, 2009.

[154] J. S. Miller and A. J. Epstein. *MRS Bull.*, 25:21, 2000.

[155] U. Malaske, C. Tegenkamp, M. Henzler, and H. Pfnuru. *Surf. Sci.*, 408:237, 1998.

[156] H. Pfnur, C. Tegenkamp, V. Maslyuk, and T. Bredow. *Surf. Sci.*, 600:1664, 2006.

[157] W. Chen, C. Tegenkamp, and H. Pfnur. *Phys. Rev. B*, 79:235419, 2009.

[158] W. Chen, C. Tegenkamp, H. Pfnur, and T. Bredow. *J. Phys. Chem. C*, 114:460–467, 2010.

[159] R. Borsali and R. Pecora. *Soft-Matter Characterization.* Springer, New York City, USA, 2008.

[160] G. Binnig, H. Rohrer, Ch. Gerber, and E. Werbel. *Phys. Rev. Lett.*, 49:2488–2489, 1982.

[161] H. Onishi, A. Sasahara, H. Uetsuka, and T. Ishibashi. *Appl. Surf. Sci.*, 188:265–271, 2002.

[162] Y. Namai, K. Fukui, and Y. Iwasawa. *Nanotechnology*, 15:S49–S54, 2004.

[163] L. Nony, R. Bennewitz, O. Pfeiffer, E. Gnecco, A. Baratoff, E. Meyer, T. Eguchi, A. Gourdon, and C. Joachim. *Nanotechnology*, 15:S91–S96, 2004.

[164] S. A. Burke, J. M. Mativetsky, R. Hoffmann, and P. Grutter. *Phys. Rev. Lett.*, 94:096102–1–4, 2005.

[165] T. Kunstmann, A. Schlarb, M. Fendrich, T. Wagner, and R. Moller. *Phys. Rev. B*, 71:121403–1–4, 2005.

[166] T. Dienel, C. Loppacher, S. C. B. Mannfeld, R. Forker, and T. Fritz. *Adv. Mater.*, 20:959–963, 2008.

[167] S. A. Burke, W. Ji, J. M. Mativetsky, J. Topple, S. Fostner, H. J. Gao, H. Guo, and P. Grutter. *Phys. Rev. Lett.*, 100:7–10, 2008.

[168] J. Schutte, R. Bechstein, P. Rahe, A. Kuhnle, and H. Langhals. *Phys. Rev. B*, 79:045428–1–8, 2009.

[169] F. Loske, R. Bechstein, J. Schutte, F. Ostendorf, M. Reichling, and A. Kuhnle. *Nanotechnology*, 20:065606–1–5, 2009.

[170] M. Kittelmann, P. Rahe, and A. Kuhnle. *J. Phys. Condens. Matter*, 24:354007–1–5, 2012.

[171] A. Hinaut, A. Pujol, F. Chaumeton, D. Martrou, A. Gourdon, and S. Gauthier. *Beilstein J. Nanotechnol.*, 3:221–229, 2012.

[172] T. R. Albrecht, P. Grütter, D. Horne, and D. Rugar. *J. Appl. Phys.*, 69:668–673, 1991.

[173] The supersharp Si cantilevers (about 2 nm nominal tip radius) were purchased from Nanosensors (www.nanosensors.com).

[174] G. Teobaldi, K. Lämmle, T. Trevethan, M. Watkins, A. Schwarz, R. Wiesendanger, and A. L. Shluger. *Phys. Rev. Lett.*, 106:216102–1–4, 2011.

[175] A. Schwarz, D. Z. Gao, K. Lämmle, J. Grenz, M. Watkins, A. Shluger, and R. Wiesendanger. *J. Phys. Chem. C*, 117:1105–1112, 2013.

[176] S. Grimme. *J. Comput. Chem.*, 27:1787–1799, 2006.

[177] G. A. Sawatzky and J. W. Allen. *Phys. Rev. Lett.*, 53:2339–2342, 1984.

[178] M. R. Castell, S. L. Dudarev, C. Muggelberg, A. P. Sutton, G. A. D. Briggs, and D. T. Goddard. *J. Vac. Sci. Technol.*, 16:1055–1058, 1998.

[179] J.D. Jackson. *Classical Electrodynamics*. Wiley, New York, NY, 1998.

[180] R. S. Mulliken. *J. Chem. Phys.*, 23:1833–1840, 1955.

[181] W. Tang, E. Sanville, and H. Henkelmann. *J. Phys.: Compute Mater.*, 21:084204–1–7, 2009.

[182] T. Sonnleitner, I. Swart, N. Pavlicek, A. Pollmann, and J. Repp. *Phys. Rev. Lett.*, 107:186103–1–4, 2011.

[183] S. Fremy, A. Schwarz, K. Lämmle, M. Prosenc, and R. Wiesendanger. *Nanotechnology*, 20:405608–1–9, 2009.

[184] F. Federici Canova, A. S. Foster, M. K. Rasmussen, K. Meinander, F. Besenbacher, and J. V. Lauristen. *Nanotechnology*, 23:1–13, 2012.

[185] W. A. Hofer, A. S. Foster, and A. L. Shluger. *Rev. Mod. Phys.*, 75:1287–1331, 2003.

[186] P. Pou, S. A. Ghasemi, P. Jelinek, T. Lenosky, S. Goedecker, and R. Perez. *Nanotechnology*, 20:264015–1–10, 2009.

[187] W. Paul, Y. Miyahara, and P. Grütter. *Nanotechnology*, 23:335702–1–7, 2012.

[188] L. Gross. *Nature Chem.*, 3:273–278, 2011.

[189] B. Schuler, W. Liu, A. Tkatchenko, N. Moll, G. Meyer, A. Mistry, D. Fox, and L. Gross. *Phys. Rev. Lett.*, 111:106103–1–5, 2013.

[190] L. Gross, F. Mohn, N. Moll, B. Schuler, A. Criado, E. Guitian, D. Pena, A. Gourdon, and G. Meyer. *Science*, 337:1326–1329, 2012.

[191] M. Ondracek, P. Pou, V. Rozsival, C. Gonzalez, P. Jelinek, and R. Perez. *Phys. Rev. Lett.*, 106:176101–1–4, 2011.

[192] C. Lazo, V. Caciuc, H. Holscher, and S. Heinze. *Phys. Rev. B*, 78:214416–1–13, 2008.

[193] A. Schwarz, U. Kaiser, and R. Wiesendanger. *Nanotechnology*, 20:264017–1–5, 2009.

[194] R. Smoluchowski. *Phys. Rev.*, 60:661–674, 1941.

[195] J. F. Jia, K. Inoue, Y. Hasegawa, W. S. Yang, and T. Sakurai. *Phys. Rev. B*, 58:1193–1196, 1998.

[196] K. Besocke, B. Kral-Urban, and H. Wagner. *Surf. Sci.*, 68:39–46, 1977.

[197] H. Ishida and A. Liebsch. *Phys. Rev. B*, 46:7153–7156, 1992.

[198] D.Z. Gao, J. Grenz, M. Watkins, F. Federici Canova, A. Schwarz, R. Wiesendanger, and A.L. Shluger. *ACS Nano*, 8:5339–5351, 2014.

[199] M. Liebmann, A. Schwarz, S. M. Langkat, and R. Wiesendanger. *Rev. Sci. Instrum.*, 73:3508–3514, 2002.

[200] J. VandeVondele, M. Krack, F. Mohamed, M. Parrinello, T. Chassaing, and J. Hutter. *Comput. Phys. Commun.*, 167:103–128, 2005.

[201] W. Wang, J. Li, and Y. Zhang. *Appl. Surf. Sci.*, 252:2673–2683, 2006.

[202] A. Rohrbach, J. Hafner, and G. Kreese. *Phys. Rev. B*, 70:125426–1–13, 2004.

[203] J. Kim, S.W. Seo, J.W. Park, J.W. Lee, Y.H. Lee, and B.K. Ju. *J. Korean Phys. Soc.*, 39:S101–S107, 2001.

[204] C. Liu, J. Erdmann, and A. Macrander. *Thin Solid Films*, 355-356:41–48, 1999.

[205] M. Hu, S. Noda, T. Okubo, and Komoyama H. *Appl. Phys. A*, 79:625–628, 2004.

[206] T. Ossowski and A. Kiejna. *Surf. Sci.*, 602:517–524, 2008.

[207] G. Wulff. *Zeitschr. Krystallogr. Mineral.*, 34:449–530, 1901.

[208] C. Argento and R. H. French. *J. Appl. Phys.*, 80:6081–6090, 1996.

[209] L. Bergstrom. *Adv. Colloid Interface Sci.*, 70:125–169, 1997.

[210] L. Kantorovich, A. I. Livshits, and M. Stoneham. *J. Phys. Condens. Matter*, 12:795–814, 2000.

[211] J. Polesel-Maris and S. Gauthier. *J. Appl. Phys.*, 97:044902, 2005.

[212] M. Kittel, J. T. Hoeft, S. Bao, M. Polcik, R. L. Toomes, J-H. Kang, D. P. Woodruff, M. Pascal, and C. L. A. Lamont. *Surf. Sci.*, 499:1–14, 2002.

[213] T.-L. Chan, C. Z. Wang, K. M. Ho, and James R. Chelikowsky. *Phys. Rev. Lett.*, 102:176101–1–4, 2009.

[214] P. Pou, S. A. Ghasemi, P. Jelinek, T. Lenosky, S. Goedecker, and R. Perez. *Nanotechnology*, 20:264015–1–10, 2009.

[215] F. Mohn, L. Gross, N. Moll, and G. Meyer. *Nature Nanotech.*, 7:227–231, 2012.

[216] P. Liljeroth, J. Repp, and G. Meyer. *Science*, 317:1203–1206, 2007.

[217] H. Jennet, H. Bubert, and E. Grallath. *Fres. Z. Anal. Chem.*, 333:502–506, 1989.

[218] T. Yokoyama, S. Yokoyama, T. Kamikado, Y. Okuno, and S. Mashiko. *Nature*, 413:619–621, 2001.

[219] M. de Wild, S. Berner, H. Suzuki, H. Yanagi, D. Schlettwein, S. Ivan, A. Baratoff, H.-J. Guntherodt, and T.A. Jung. *Chem. Phys. Chem.*, 3:825–885, 2002.

[220] C. Bobisch, Th. Wagner, A. Bannani, and R. Möller. *J. Chem. Phys.*, 119:9804–9809, 2003.

[221] M. Abel, S. Clair, O. Ourdjini, M. Mossoyan, and L. Port. *J. Am. Chem. Soc.*, 133:1203–1205, 2011.

[222] O. Ourdjini, R. Pawlak, M. Abel, S. Clair, L. Chen, N. Bergeon, M. Sassi, and V. Oison. *Phys. Rev. B*, 84:125421–1–9, 2011.

[223] B. Baris, J. Jeannoutot, V. Luzet, F. Palmino, A. Rochefort, and F. Cherioux. *ACS Nano*, 6:6905–6911, 2012.

[224] S.A. Burke, J.M. Topple, and P. Grütter. *J. Phys. Condens. Matter*, 21:423101–1–16, 2009.

[225] L. Nony, E. Gnecco, A. Baratoff, A. Alkauskas, R. Bennewitz, O. Pfeiffer, S. Maier, A. Wetzel, E. Meyer, and Ch. Gerber. *Nano Letters*, 11:2185–2189, 2004.

[226] P. Rahe, M. Kittelmann, J.L. Neff, M. Nimmrich, M. Reichling, P. Maass, and A. Kühnle. *Adv. Mater.*, 25:3948–3956, 2013.

[227] U. Zerweck, C. Loppacher, and L.M. Eng. *Nanotechnology*, 17:S107–S111, 2006.

[228] S. Maier, L.-A. Fendt, L. Zimmerli, T. Glatzel, O. Pfeiffer, F. Diederich, and E. Meyer. *Small*, 4:1115–1118, 2008.

[229] R. Pawlak, L. Nony, F. Bocquet, V. Oison, M. Sassi, J.-M. Debierre, C. Loppacher, and L. Porte. *J. Phys. Chem. C*, 114:9290–9295, 2010.

[230] B. Such, T. Trevethan, T. Glatzel, S. Kawai, L. Zimmerli, E. Meyer, A.L. Shluger, C.H.M. Amjis, P. de Mendoza, and A.M. Echavarren. *ACS Nano*, 114:9290–9295, 2010.

[231] A. Hinaut, K. Lekhal, G. Aivazian, S. Bataille, A. Gourdon, D. Martrou, and S. Gauthier. *J. Phys. Chem. C*, 115:13338–13342, 2011.

[232] A. Hinaut, A. Pujol, F. Chaumeton, D. Martrou, A. Gourdon, and S. Gauthier. *Nanotechnology*, 3:221–229, 2012.

[233] A. Amrous, F. Bocquet, L. Nony, F. Para, C. Loppacher, S. Lamare, F. Palmino, F. Cherioux, D.Z. Gao, F. Federici Canova, M. B. Watkins, and A.L. Shluger. *Adv. Mater. Interfaces*, Accepted:TBD, 2014.

[234] J.A.A.W. Elemens, S. Lei, and S. de Feyter. *Angew. Chem., Int. Ed.*, 48:7298–7333, 2009.

[235] Y. Makoudi, M. Beyer, J. Jeannoutot, F. Palmino, F. Picaud, and F. Cherioux. *Chem. Commun.*, 50:5714–5716, 2014.

[236] Y. Makoudi, F. Palmino, M. Arab, E. Duverger, and F. Cherioux. *J. Am. Chem. Soc.*, 130:6670–6671, 2008.

[237] M.C. McCarthy, F. Tamassia, D.E. Woon, and P. Thaddeus. *J. Chem. Phys.*, 129:184301–1–6, 2008.

[238] W. Liu, J. Carrasco, B. Santra, A. Michaelides, M. Scheffler, and A. Tkatchenko. *Phys. Rev. B*, 86:245405–1–6, 2012.

[239] F.W. de Wette, W. Kress, and U. Schröder. *Phys. Rev. B*, 32:4143–4157, 1985.

[240] M. O. Sinnokrot, E. F. Valeev, and E. F. Sherrill. *J. Am. Chem. Soc.*, 124:10887–10893, 2002.

[241] J. M. Sanders. *J. Phys. Chem.*, 114:9205–9211, 2010.

[242] S. E. Wheeler. *Acc. Chem. Res.*, 46:1029–1038, 2013.

[243] C.R. Martinez and B.L. Iverson. *Chem. Sci.*, 3:2192–2201, 2012.

[244] L.B. Wright, M. Rodger, S. Corni, and T.R. Walsh. *J. Chem. Theory Comput.*, 9:1616–1630, 2013.

[245] L.B. Wright, M. Rodger, T.R. Walsh, and S. Corni. *J. Phys. Chem. C*, 117:24292–24306, 2013.

[246] B. R. Brooks, C. L. Brooks, III, A. D. Mackerell, Jr., L. Nilsson, R. J. Petrella, B. Roux, Y. Won, G. Archontis, C. Bartels, S. Boresch, A. Caflisch, L. Caves, Q. Cui, A. R. Dinner, M. Feig, S. Fischer, J. Gao, M. Hodoscek, W. Im, K. Kuczera, T. Lazaridis, J. Ma, V. Ovchinnikov, E. Paci, R. W. Pastor, C. B. Post, J. Z. Pu, M. Schaefer, B. Tidor, R. M. Venable, H. L. Woodcock, X. Wu, W. Yang, D. M. York, and M. Karplus. *J. Comput. Chem.*, 30(10, Sp. Iss. SI):1545–1614, 2009.

[247] B.R. Brooks, R.E. Bruccoleri, D.J. Olafson, D.J. States, S. Swaminathan, and M. Karplus. *J. Comput. Chem.*, 4:187–217, 1983.

[248] A.D. MacKerel Jr., C.L. Brooks III, L. Nilsson, B. Roux, Y. Won, and M. Karplus. *CHARMM: The Energy Function and Its Parameterization with an Overview of the Program*, volume 1 of *The Encyclopedia of Computational Chemistry*, pages 271–277. John Wiley & Sons: Chichester, 1998.

[249] W.D. Cornell, P. Cieplak, C.I. Bayly, I.R. Gould, K.M. Jr Merz, D.M. Ferguson, D.C. Spellmeyer, T. Fox, J.W. Caldwell, and P.A. Kollman. *J. Comput. Chem.*, 24:1999–2012, 2003.

[250] A.K. Rappe amd C.J. Casewit, K.S. Colwell, W.A. Goddard III, and W.M. Skiff. *J. Am. Chem. Soc.*, 114:10024–10035, 1992.

[251] F. Sato, S. Hojo, and H. Sun. *J. Phys. Chem. A*, 107(2):248–257, 2003.

[252] Nadeem A. Vellore, Jeremy A. Yancey, Galen Collier, Robert A. Latour, and Steven J. Stuart. *Langmuir*, 26(10):7396–7404, 2010.

[253] Robert B. Best, Xiao Zhu, Jihyun Shim, Pedro E. M. Lopes, Jeetain Mittal, Michael Feig, and Alexander D. MacKerell. *J. Chem. Theory Comput.*, 8(9):3257–3273, 2012.

[254] M. Mitchell. *An Introduction to Genetic Algorithms*. MIT Press, Cambridge, MA, 1998.

[255] S.M. Woodley and R. Catlow. *Nature Mater.*, 7:937–946, 2008.

[256] J. Hunger, S. Beyreuther, G. Huttner, K. Allinger, U. Radelof, and L. Zsolnai. *Eur. J. Inorg. Chem.*, 1:693–702, 1998.

[257] J. Hunger and G. Huttner. *J. Comput. Chem.*, 20:455–471, 1999.

[258] J. Wang and P. A. Kollman. *J. Comput. Chem.*, 22:1219–1228, 2001.

[259] T. Strassner, M. Busold, and W. A. Herrmann. *J. Comput. Chem.*, 23:282–290, 2002.

[260] H. R. Larsson, A. C. T. van Duin, and B. Hartke. *J. Comput. Chem.*, 34:2178–2189, 2013.

[261] A. Jaramillo-Botero, S. Naserifar, and W.A. Goddard III. *J. Chem. Theory Comput.*, 10:1426–1439, 2014.

[262] Jr. A.D. MacKerell, D. Bashford, M. Bellott, Jr. R.L. Dunbrack, J.D. Evanseck, M.J. Field, S. Fischer, J. Gao, H. Guo, S. Ha, D. Joseph-McCarthy, L. Kuchnir, K. Kuczera, F.T.K. Lau, C. Mattos, S. Michnick, T. Ngo, J.C. Smith, R. Stote, J. Straub, M. Watanabe, J. Wiorkiewicz-Kuczera, D. Yin, and M. Karplus. *J. Phys. Chem. B*, 102(18):3586–3616, 1998.

[263] M.P. Allen and D.J. Tildesley. *Computer Simulation of Liquids*. Oxford University Press, Oxford, UK, 1987.

[264] Philip M. Morse. *Phys. Rev.*, 34:57–64, Jul 1929.

[265] F. G. Fumi and M. P. Tosi. *J. Phys. Chem. Solids*, 25:31, 1964.